Stochastic Oscillations in Living Cells

Exemplified by Ca^{2+} and p53

D I S S E R T A T I O N

zur Erlangung des akademischen Grades

d o c t o r r e r u m n a t u r a l i u m
(Dr. rer. nat.)
im Fach Biophysik

eingereicht an der
Lebenswissenschaftlichen Fakultät
Humboldt-Universität zu Berlin

von
Dipl. Physiker Gregor Mönke

Präsident der Humboldt-Universität zu Berlin:
Prof. Dr. Jan-Hendrik Olbertz

Dekan der Lebenswissenschaftlichen Fakultät:
Prof. Dr. Richard Lucius

Gutachter:
1. Prof. Hanspeter Herzel
2. Dr. Alexander Löwer
3. Dr. Martin Falcke

eingereicht am: 18. Dezember 2014
Tag der mündlichen Prüfung: 7. Mai 2015

Abstract

Recent developments in cell biology, especially single cell experiments, allow for a very detailed view on intracellular processes. It has become evident, that there are many complex dynamics present, which can not be described by standard steady state or regular oscillatory regimes. In this work two signaling pathways, involving the tumor suppressor p53 and the second messenger Ca^{2+} , are discussed and modelled in this context.

The tumor suppressor p53 shows a pulsatile response in single cells after induction of DNA double strand breaks (DSBs). Except for very high amounts of damage, these pulses appear at irregular times. To quantify these irregularities, the inter pulse interval (IPI) distributions are extracted from the data with the help of a wavelet based feature detection. A comparison to synthetic noisy limit cycle oscillator dynamics indicate the presence of non-oscillatory regimes in the data. The concept of excitable systems is employed as a convenient way to model such observed dynamics. An application to biomolecular reaction networks shows the need for a positive feedback within the p53 regulatory network. Exploiting the reported ultrasensitive dynamics of the upstream damage sensor kinases, leads to a simplified excitable kinase-phosphatase model. Coupling that to the canonical negative feedback p53 regulatory loop, is the core idea behind the construction of the excitable p53 model. A detailed bifurcation analysis of the full model establishes a robust excitable regime, which can be switched to oscillatory dynamics via a strong DNA damage signal. This elegantly reproduces the experimentally observed *digital response* after damage. To further assess the observed cell-to-cell variability, single cell damage foci trajectories are analysed. A Markovian process describing the DSB dynamics is constructed and a strategy to extract its parameters from the data is devised. Driving the p53 model with that stochastic process yields pulsatile dynamics which reflect different experimental scenarios. Finally, the modeling results lead to a reanalysis of published data, supporting the anticipated structure of the regulatory p53 network.

Intracellular Ca^{2+} concentration spikes arise from a hierarchic cascade of stochastic events. In this thesis, the emphasis first lies on the mathematical theory behind the established stochastic Ca^{2+} models. An analytical solution strategy, employing a semi-Markovian description and involving Laplace transformations, is devised and successfully applied to a specific Ca^{2+} model. The new gained insights are then used, to construct a new generic Ca^{2+} model, which elegantly captures many known features of Ca^{2+} signaling. In particular the experimentally observed relations between the average and the standard deviation of the inter spike intervals (ISIs) can be explained in a concise way. Additionally, an exact and fast algorithm to simulate semi-Markovian processes is developed. Finally, the theoretical considerations allow to calculate the stimulus encoding relation, which governs the adaption of the Ca^{2+} signals to varying extracellular stimuli. This is predicted to be a fold change response and new experimental results obtained by collaborators display a strong support of this idea.

Zusammenfassung

Neueste Entwicklungen der Zellbiologie, insbesondere Einzelzell basierte Experimente, erlauben einen sehr genauen Blick auf intrazelluläre Prozesse. Es hat sich gezeigt, dass es sehr vielfältige und komplexe Dynamiken gibt, welche nicht durch stationäre Zustände oder regelmäßige Oszillationen modelliert werden können. In dieser Arbeit werden zwei intrazelluläre Signalwege, betreffend den Tumorsuppressor p53 und das Signalmolekül Ca^{2+} , in dieser Hinsicht diskutiert und modelliert.

Einzelzellmessungen des Tumorsuppressors p53 zeigen pulsatile Antworten nach Zufügung von DNA Doppelstrangbrüchen (DSBs). Außer für sehr hohe Schadensdosen, ist das zeitliche auftreten dieser Pulse unregelmäßig. Mithilfe eines Wavelet basierten Pulsdetektors werden die einzelzell Trajektorien untersucht und die inter-Puls Intervall (IPI) Verteilungen extrahiert. Diese weisen auf nicht-oszillatorische Regime in den Daten hin, quantitativ überprüft durch den Vergleich mit künstlich erzeugten verrauschten Oszillationen. Die Theorie der anregbaren Systeme angewendet auf regulatorische Netzwerke ermöglicht dieses komplexe Verhalten mathematisch zu beschreiben. Die Theorie erfordert zwingend einen starken positiven feedback im modellierten p53 Netzwerk. Das beobachtete ultra-sensitive Verhalten der Schadens-Sensor Kinasen, deutet auf einen solchen positiven feedback hin. Die Kopplung dieser Kinase Dynamik mit dem kanonischen p53 negativen feedback loop, ergibt ein anregbares p53 Modell. Detaillierte Bifurkationsanalysen zeigen ein robustes anregbares Regime, welches durch ein starkes Schadenssignal auch in Oszillationen überführt werden kann. Dies zusammen reproduziert auf natürliche Weise die experimentell beobachtete *digitale Antwort* nach Schaden. Desweiteren werden einzelzell Schadensdynamiken analysiert. Diese zeigen eine große Variabilität zwischen den Zellen, was zu einer markovschen Beschreibung der DSB Dynamik führt. Sowohl die Reparatur- als auch die spontane Bruchrate können aus den Daten geschätzt werden. Treibt man das p53 Modell mit diesem stochastischen Prozess, kann sowohl das oszillatorische Verhalten nach hohem Schaden, als auch das unregelmäßige pulsatile Verhalten ohne äußere Stimulation reproduziert werden. Schließlich führen diese Überlegungen zu einer Reanalyse bereits publizierter Daten, welche die gemachten Annahmen über das regulatorische p53 Netzwerk unterstützen.

Intrazelluläre Ca^{2+} Spikes entstehen durch eine hierarchische Kaskade stochastischer prozesse. In dieser Arbeit wird zuerst die hinter etablierten stochastischen Ca^{2+} Modellen liegende mathematische Theorie vertieft. Die Anwendung einer semi-markovschen Beschreibung führt zu praktischen analytischen Lösungen mit Hilfe von Laplace Transformationen. Eine hierbei entdeckte Zeitskalenseparation ermöglicht ein neues allgemeines Ca^{2+} -Modell. Dieses erklärt auf äußerst prägnante Weise viele wesentliche experimentelle Ergebnisse, insbesondere die Momentenbeziehungen der inter-Spike Intervall Verteilungen. Numerische Analysen bestätigen die Validität dieses neuen Modells. Schließlich erlaubt die hier vorgestellte Theorie Berechnungen der Stimulus-Enkodierung, also die Adaption des Ca^{2+} Signals auf veränderliche extrazelluläre Stimuli. Die Vorhersage einer *fold change* Enkodierung kann durch Experimente, durchgeführt von Kollaborationspartnern, gestützt werden.

Dann lächelt der bescheidene Gelehrte und sagt zu den Staunenden: "Was habe ich denn erschaffen? Nichts. Der Mensch erfindet keine Kraft, er lenkt sie nur, und die Wissenschaft besteht darin, die Natur nachzuahmen."

Honoré de Balzac

Contents

1. An excitable p53 model **1**

1.1. Introduction to p53 and the DNA damage response system . . . 1
1.1.1. The guardian of the genome . . . 1
1.1.2. DNA double strand breaks . . . 2
1.1.3. Established p53 dynamics . . . 2
1.2. Experimental findings not covered by oscillatory dynamics . . . 4
1.2.1. Introducing IPI distributions . . . 5
1.2.2. p53 data analysis . . . 7
1.3. Modeling theory . . . 12
1.3.1. Preface - dynamical systems theory and biochemical reaction networks . . . 12
1.3.2. Negative feedback oscillators . . . 14
1.3.3. Introduction to excitability - case study FitzHugh Nagumo 18
1.4. The ATM-Wip1 switch building block . . . 25
1.4.1. ATM as Signalling Switch . . . 25
1.4.2. Incorporating the Phosphatase Wip1 . . . 27
1.5. Including the core negative feedback loop - the full p53 model . . 30
1.5.1. The effectual modeled p53 network for the DSB response 30
1.5.2. Bifurcation analysis and deterministic dynamics . . . 33
1.6. Driving the p53 model with a stochastic DSB process . . . 39
1.6.1. Constructing a stochastic process for the DSB dynamics . 39
1.6.2. Stochastic forcing of the excitable p53 model . . . 46
1.7. Reanalysis of inhibitor experiments . . . 50
1.8. Discussing the p53 modeling approach . . . 54

2. Hierarchic stochastic modelling of intracellular Ca^{2+} **59**

2.1. Introduction to intracellular Ca^{2+} signaling . . . 59
2.2. An analytical approach to hierarchic stochastic modelling . . . 61
2.2.1. What is HSM ? . . . 61
2.2.2. Semi-Markov processes . . . 63
2.2.3. Non-Markovian master equations and first passage times . 64
2.2.4. A simple semi-Markovian system . . . 65
2.2.5. Explicit solutions for the tetrahedron Ca^{2+} model . . . 69
2.3. Exploiting time scale separation - The generic Ca^{2+} model . . . 74
2.3.1. Model Construction . . . 75
2.3.2. Results of the generic model . . . 77
2.3.3. Error analysis . . . 79
2.4. Numerical Analysis of the HSM Ca^{2+} model . . . 81
2.4.1. The DSSA algorithm . . . 81

2.4.2. An exact semi-Markovian simulation algorithm 83
2.5. Encoding Stimulus intensities in random spike trains 86
2.5.1. Theoretical predictions 86
2.5.2. Experiments supporting the fold change encoding hypothesis 89
2.6. Discussion of the stochastic Ca^{2+} modeling 93

3. Concluding remarks **97**

A. Appendix p53 **99**
A.1. Peak detection with wavelets 99
A.2. Table of Parameters for the p53 model 105
A.3. Sensitivity of pulse shapes and the excitation threshold on parameter variations 107
A.4. Codimension-2 bifurcation diagrams 112
A.5. Period of oscillations in the p53 model 113

B. Appendix Ca^{2+} **115**
B.1. Laplace transformations of Ψ_o and Ψ_c 115

C. List of abbreviations **119**

Acknowledgments **131**

1. An excitable p53 model

1.1. Introduction to p53 and the DNA damage response system

The mammalian p53 gene belongs, with tens of thousands of publications, to the best studied genes in molecular biology. It is inactivated in about half of the human cancers and consequently was the first tumor suppressor to be identified [3]. This insight put p53 right in the center of molecular cancer research, and triggered *an avalanche of research* until today [108]. Although, there have been numerous modeling approaches in the past, the focus on the irregular pulsatile dynamics found for the basal p53 dynamics shed new light on the underlying design principles of the regulatory network for p53. The findings to be developed in the following were greatly supported by the group of Alexander Loewer at the MDC Berlin. All experimental raw data used here was either directly measured by the group, or originates from publications developed at the group of Galit Lahav at the Harvard Medical School with a major contribution from Alexander Loewer.

1.1.1. The guardian of the genome

As a central hub in different stress response signalling networks, p53 can be activated by various upstream kinases which often serve as stress sensors. It gets activated e.g. by oncogene induced $p14^{arf}$, in response to single strand DNA breaks and double strand DNA breaks (DSBs). The latter is mediated by the ataxia telangiectasia mutated (ATM) kinase, which serves as a damage sensor. Upon activation p53 acts as a transcription factor for numerous target genes which in effect regulate different cellular stress responses like DNA repair, cell-cycle-arrest or apoptosis [80, 108]. The versatility of the downstream output of p53 activation stems from its many post translational modification sites. These include, besides phosphorylation, acetylation, sumolation, glycolysation and ubiquitination on various residues [55]. In summary, the tumor suppressing function of p53 is achieved by preventing the proliferation of cells with corrupted genomic integrity. It was therefore called *the guardian of the genome* [28, 58].

A key feature of the p53 regulatory system is that p53 transcriptionally activates its own suppressor Mdm2 (mouse double minute protein 2) [45, 77]. Mdm2 is an E3-ligase which binds to p53 and polyubiquitinates it. This effectively flags p53 for the proteolytic pathway and therefore induces its degradation [19]. In unstressed conditions this negative feedback loop keeps p53 at low levels as needed for cell homeostasis. Remarkably the entire regulation of p53 takes place on a post translational level, as the level of p53 transcripts remains constant over time, particularly also after stimulation [52].

1.1.2. DNA double strand breaks

DNA double strand breaks are a particularly dangerous form of DNA damage and are a prevalent cause of p53 signaling. If not repaired genomic rearrangements including translocations, deletions and fusion may follow. These kinds of genomic aberrations are often found in cancerous cells [53]. DSBs occur naturally inside cells, most prominent causes are radical metabolic by-products, cosmic radiation and errors during DNA replication. To induce DSBs experimentally living cells are either irradiated with γ-irradiation or the radiomimetic drug neocarzinostatin (NCS) is used. After damage induction, very complex processes involving damage sensing, repair mechanisms and signalling to downstream pathways including p53 take place. The protein complexes which develop around a damage locus is called a foci. Some of these processes important for p53 dynamics will be discussed in detail later in this work in section 1.4.1.

To track foci formation and their subsequent disappearance indicating repair in living cells, a protein called 53BP1 was labeled with the red fluorescent protein mCherry [63]. 53BP1 is an important mediator of the damage response which localizes early at the damage loci [109]. By using time-lapse microscopy, foci trajectories can be recorded which serve as a proxy for the number of DSBs inside a cell. Foci dynamics for cells stimulated by NCS and γ-irradiation with different dosing are shown in figure 1.2. The repair dynamics generally follow an exponential decay, although at least two different molecular mechanisms contribute to the repair process [63]. Highlighted by the quantiles, the variability of the amount of initial damage a single cell receives in a fixed dose experiment is quite high. This contributes to the variability in p53 dynamics to be discussed later.

1.1.3. Established p53 dynamics

The first experimental study which attempted to reveal the p53 dynamics after DSB induction, in contrast to only steady state transitions observed before, was conducted almost 15 years ago [5]. By harvesting cells every hour after stimulation and probing for P53 and Mdm2 in a Western Blot analysis they found damped oscillatory behavior of both proteins. Interestingly these authors were also motivated from the theoretical side and proposed an ODE model capturing the observed dynamics which was solely based on the properties of the P53-Mdm2 negative feedback loop. A detailed discussion of oscillations in system with only negative feedbacks follows in section 1.3.2.

Since the onset of single cell analysis, the dynamical behavior of cells can be studied in much more detail. The first reporter system for both P53 and Mdm2 was established around 10 years ago [57]. Lahav and her co-workers stably transfected MCF7 cells with the fusion proteins P53-CFP and Mdm2-YFP. They showed that both fusion constructs were functional and were expressed and therefore regulated like their endogenous counterparts. In summary they were able to reliably track the P53 and Mdm2 protein dynamics on a single cell level using time lapse fluorescence microscopy. The main results were as follows: Mean pulse height and duration are independent of the damage

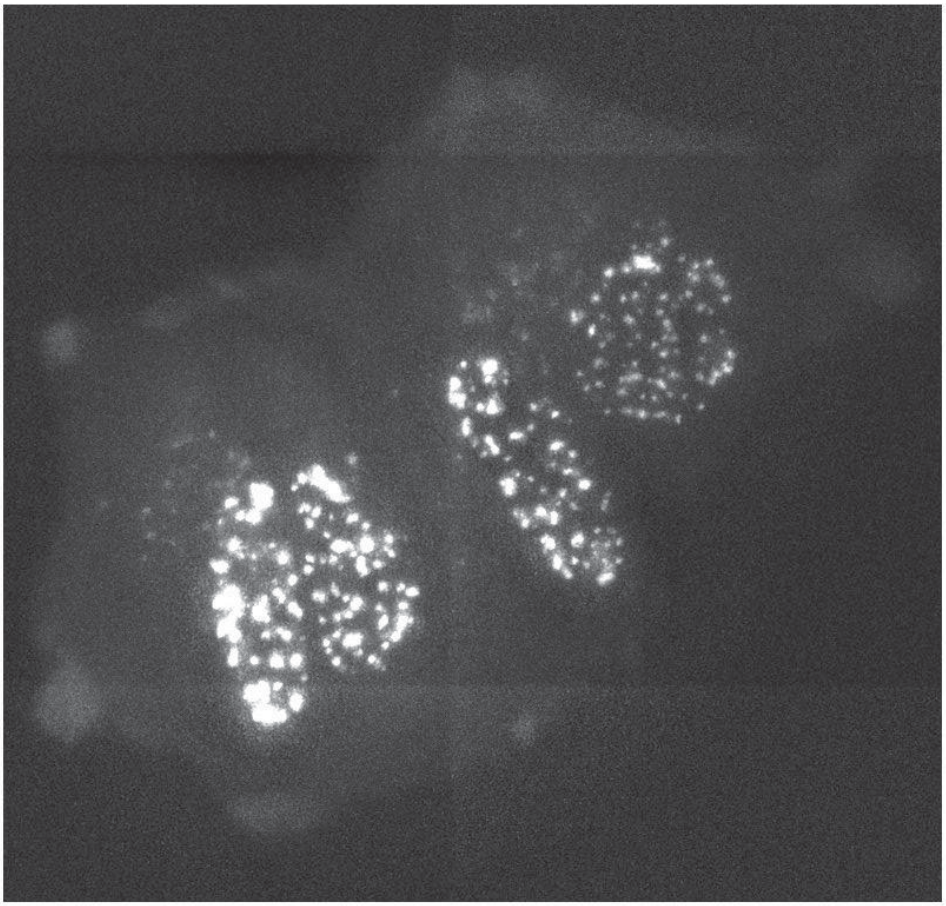

Figure 1.1.: A fluorescence image of mCherry labeled 53BP1 localized in foci inside the nuclei of four MCF7 cells. DSBs were induced by treating the cells with 50ng of the radiomimetic drug NCS.

dose and cells respond with a variable discrete number of such pulses. This number is dependent on the damage dose, and the authors concluded that the stimulus response is encoded in a digital fashion. Two representative single cell trajectories after strong stimulation are shown in figure 1.3. Different timing and especially different numbers of pulses in individual cells lead to damped oscillations on the population level, as to be seen in a the Wester blot analysis. Subsequently this damped oscillatory behavior as described in the last paragraph ([5]) could be recovered by averaging over the single cell trajectories. This striking study clearly showed, that single cell analysis can reveal qualitatively different cellular behavior compared to what can be learned from population data. In a subsequent study it was shown, that MCF7 cells can oscillate for up to three days on a single cell level after DNA damage

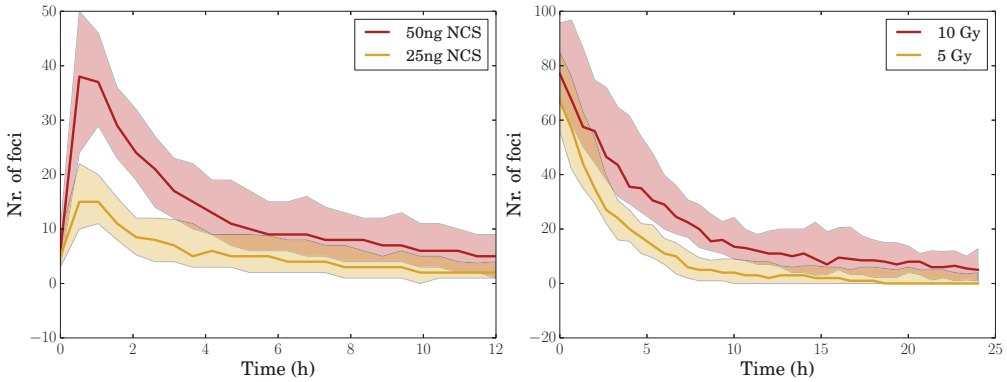

(a) Stimulation by NCS, 179 (25ng NCS) and 220 (50ng NCS) cells respectively

(b) Stimulation by γ-irradiation, 63 (10 gray) and 54 (5 gray) cells respectively

Figure 1.2.: Foci dynamics after damage induction. Median number of foci and quantiles in shaded area are shown over time. Raw data obtained from the Loewer lab.

[34]. However, the authors also pointed out, that a significant fraction of the cells showed dynamics unresembling sustained oscillations. Most notably with higher initial damage dose these irregular trajectories become less abundant. A quantitative analysis on the irregularity of p53 trajectories measured in weakly or non-stimulated MCF7 cells is presented in the next section 1.2.2.

1.2. Experimental findings not covered by oscillatory dynamics

The main focus of many works dedicated to study p53 dynamics lays on the systems response to a high damage induction. Therefore, also many theoretical studies concentrate on modeling this high damage scenario. As the main experimental results indicate constant amplitude and constant pulse duration, the p53 dynamics after strong stimulation are characterized as sustained oscillations. From the dynamical system theory side, this behavior qualifies to be modeled by limit cycle oscillators. And indeed most if not all theoretical studies construct an ODE model which exhibits a limit cycle regime [6, 15, 34, 35, 65].

In this section experimental results are presented, which are not readily captured by limit cycle models. Most of the analyzed raw data originates from experiments done by Alexander Loewer [62] in the group of Galit Lahav. At first, the inter-pulse-interval (IPI) distribution will be introduced, as means to reliably detect p53 dynamics deviating from sustained oscillations. Additionally a generic limit cycle model with additive noise is used to generate synthetic data to illustrate the IPI distribution characteristics expected for a sustained oscillator.

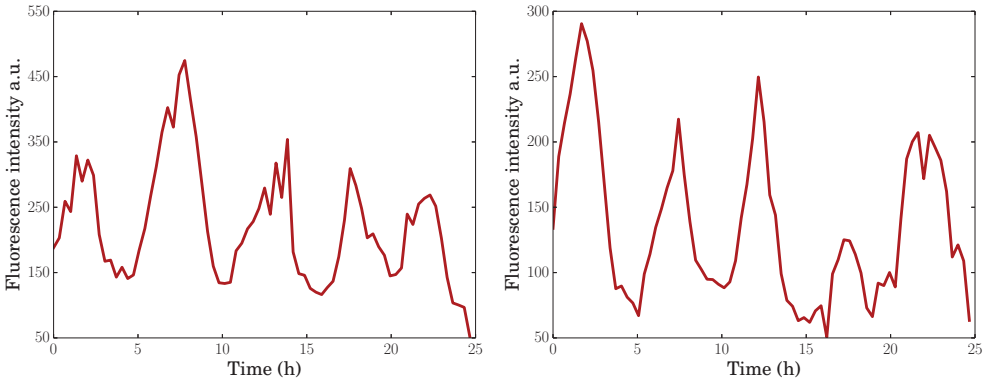

Figure 1.3.: Two representative MCF7 single cell p53 trajectories after strong stimulation with 400ng NCS. The oscillatory dynamics are clearly visible. Raw data obtained from the Loewer lab.

1.2.1. Introducing IPI distributions

From a signaling theory viewpoint, the classification of trajectories as showing oscillations involves standard methods like spectral analysis. However, in the real world of fluorescence single cell p53 data the trajectories are rather short, showing typically less than ten pulses. In combination with inevitable measurement noise, see e.g. figure 1.3, spectral methods are of limited applicability. Nevertheless, a quantitative measure of oscillatory behavior is needed. The distribution of the combined IPIs for all cells yields such a measure. To extract the IPIs from the data, a reliable peak detection algorithm was devised and implemented using wavelet analysis. Details about it can be found in the Appendix A.1.

The interpretation of the IPI distribution is straightforward. For a perfect oscillator the IPIs are delta distributed $\delta(t - T_{osc})$, with T_{osc} being the period of the oscillator. By adding a moderate amount of noise to the oscillator resembling the variability found in the p53 data, the IPIs are narrowly distributed around T_{osc}. To generate synthetic data to illustrate these properties a generic limit cycle oscillator (LCO) [111] given by the following equations:

$$\begin{aligned} \frac{dr}{dt} &= -\lambda(r - A) + \xi_r \\ \frac{d\phi}{dt} &= \frac{2\pi}{T_{osc}} + \xi_\phi, \end{aligned} \tag{1.1}$$

is used. Here A is the amplitude and λ is the relaxation rate. The two noise terms ξ_r and ξ_ϕ have Gaussian white noise properties, namely $\langle \xi_i(t+\tau), \xi_i(t) \rangle = 2D_i\delta(\tau)$, with i being either the radial variable r or the angular variable ϕ. The constants D_r and D_ϕ give the noise intensities for radial and angular perturbations respectively. This stochastic ODE is numerically solved using the standard Euler-Maruyama method. The generated trajectories are then analyzed by the wavelet based peak detection algorithm, and the IPIs are extracted.

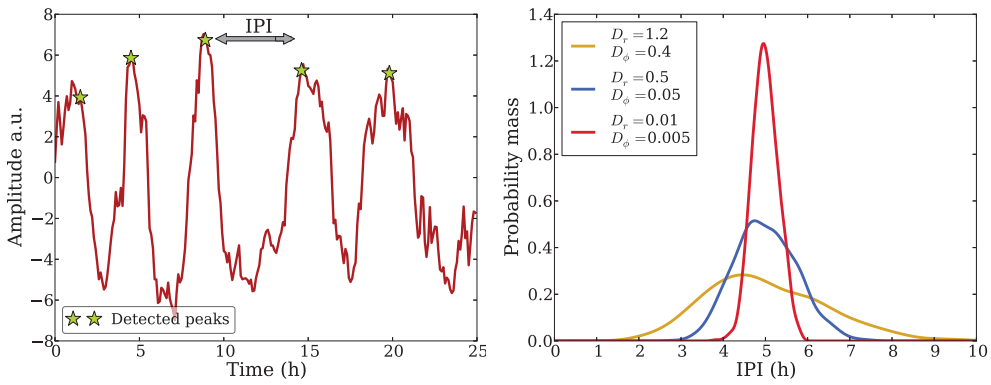

(a) Section of a representative noisy LCO trajectory, parameters are $A = 10$, $T_{osc} = 5$, $\lambda = 0.2$, $D_r = 1.2$ and $D_\phi = 0.4$.

(b) IPI distributions for the noisy LCO for different noise intensities as indicated in the legend.

Figure 1.4.: Dynamics and IPI distributions of the noisy generic LCO introduced in the main text.

In figure 1.4 a representative simulated trajectory of this noisy generic LCO is shown. The corresponding IPI distribution, calculated from a much longer simulation run is shown next to it, together with results for different noise intensities. As one might intuitively expect, the IPI distributions get broader with higher noise intensities. Notably the IPI distributions symmetrically center around the LCO period T_{osc}, which is also clearly visible in the box plot representation shown in figure 1.5.

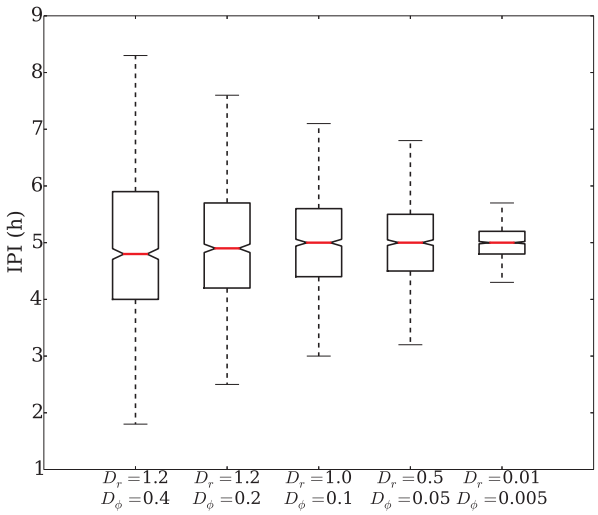

Figure 1.5.: Box plots of the IPI distributions for the noisy LCO. The distributions are symmetrically centered around $T_{osc} = 5$ and their inter quartile range decreases with decreasing noise intensity.

It will become clear in the next section, that it is foremost the uniform pulse shape combined with the aberrant IPI distribution which indicates a non LCO behavior of the p53 dynamics for no or weak stimulation.

1.2.2. p53 data analysis

The raw data reanalyzed here was already published some years ago [7]. Damaging the MCF7 cells is done by adding various concentrations of NCS prior to fluorescence microscopy analysis. The cells are then imaged every 20 minutes which yields time series of p53 fluorescence intensity. Details of the experimental conditions are shown in table 1.1. The established results obtained in the published works about pulse widths and amplitudes will be re-examined, and the IPI distributions are evaluated. All analysis is done with the wavelet based peak detection method as described in the appendix A.1.

Table 1.1.: Overview of the analyzed p53 data set. The total measurement time is 48 hours and the sampling rate is 20 minutes.

condition	**number of cells**
Control	92
25ng NCS	109
50ng NCS	108
100ng NCS	101
200ng NCS	88
400ng NCS	94

To get a first general overview about how a cell population responds to various stimulus strengths, pulse counting statistics are shown in figure 1.6. The general pulsing activity of cells rises with stronger stimulation, which is evident because higher stimulation induces on average more DSBs and therefore longer repair times. That in term causes p53 activating damage signals to trigger more pulses.

It is, however, noteworthy that there is also a basal p53 dynamic. Even in the control condition there is on average one pulse every twelve hours. One cause of that basal activity are DSBs inflicted during normal cell growth [62], other damage sources are spontaneous transient DSBs caused for example by radical metabolites. These erratic DSB occurrences will play an important role later on in this work when a stochastic process describing the DSB dynamics will be developed. Furthermore, the cell-to-cell variability in the number of pulses shown in figure 1.7 is very large for cells in identical conditions. This can be at least partly explained by the fact that even for a fixed damage dose there is always a distribution of actually inflicted DSBs as depicted by the quantiles in figure 1.2 in the preceding section.

Pulse counting alone can not reveal sufficient information about the p53 dynamics over time. To further characterize the observed pulsatile dynamics, the IPI distributions are extracted from the data. The IPIs are naturally dependent on the pulse widths, defined here as time between the start of the rise and the end of the descent of a pulse as depicted in figure 1.8.

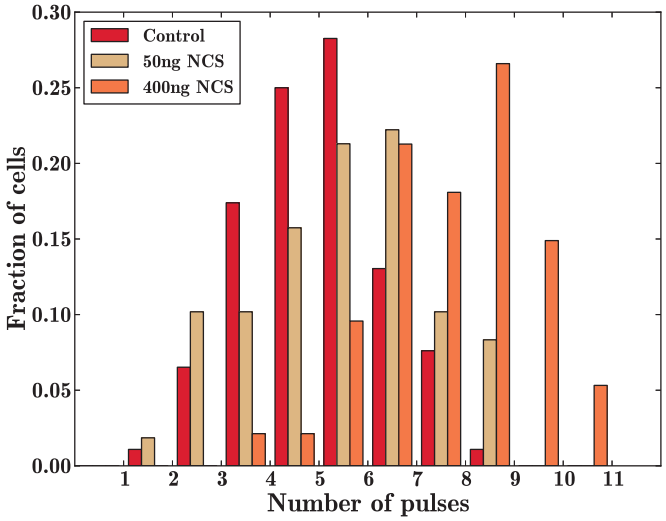

Figure 1.6.: Pulse number histograms for three selected experimental conditions. The shift of the mean of the distributions towards higher values for stronger stimulation is clearly visible, but there is also basal activity as shown by the control data set. Notably, the variability in pulse numbers for one condition is quite large.

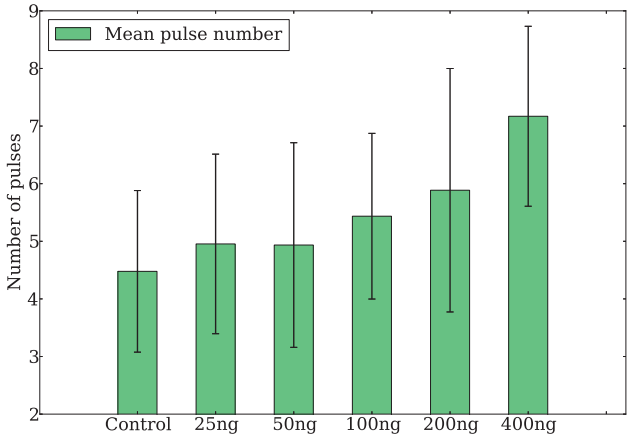

Figure 1.7.: Mean and standard deviation of pulse numbers for every condition. The cell-to-cell variability of the number of pulses is captured by the standard deviation.

The minimum IPI can thus only be as small as the smallest pulse width. For time series data where the typical IPI is much larger then the average pulse width, this effect is negligible. However, p53 trajectories show very broad and often consecutive pulses with an average width of about five hours. Hence, to adequately compare IPI distributions of different experimental conditions, the

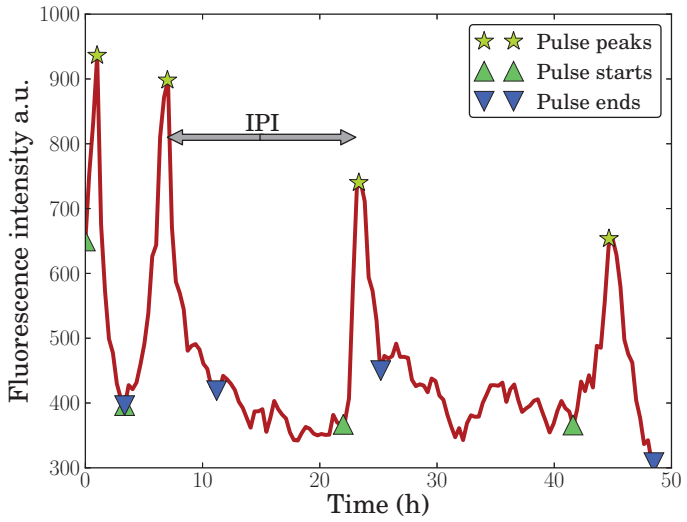

Figure 1.8.: P53 trajectory with detected pulse starts, ends and peaks. The novel detection method is described in the appendix A.1. One IPI of the three IPIs present in this trajectory is exemplified. The cell was stimulated with 25ng of NCS.

pulse width distribution was also analyzed and is shown in figure 1.10.

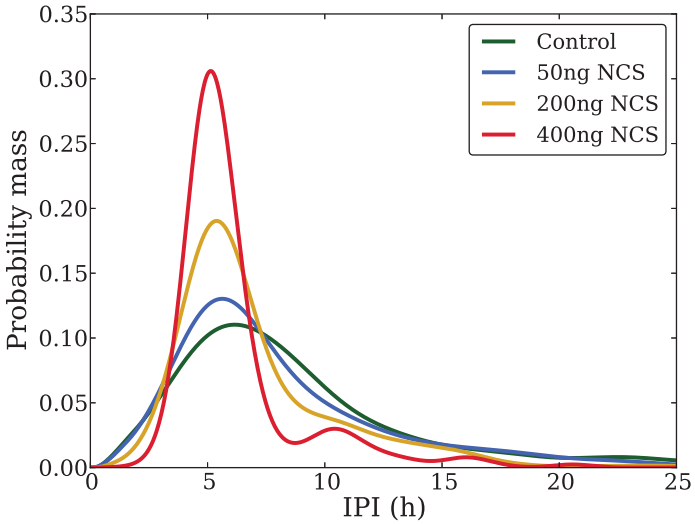

Figure 1.9.: IPI distributions for selected experimental conditions. The distributions get broader and skewed towards longer IPIs with decreasing stimulation. This clear variation in the IPI distributions can not be explained by the small differences in pulse widths in between the different conditions as shown in figure 1.10.

The main result from the IPI analysis is, that the weaker the stimulation, the

more skewed is the IPI distribution towards longer IPIs. In addition, the pulse widths are nearly the same for all conditions, with a difference in the median between unstimulated and stimulated cells of one sample point or 20 minutes. This means, that the pulse appearance over time can be highly irregular and deviates significantly from a behavior expected from a sustained oscillator for the weak or non stimulated cells. On the contrary, the pulse shape characterized by widths and amplitude is a robust property of the pulsatile p53 dynamics, results of their analysis are shown in figure 1.10.

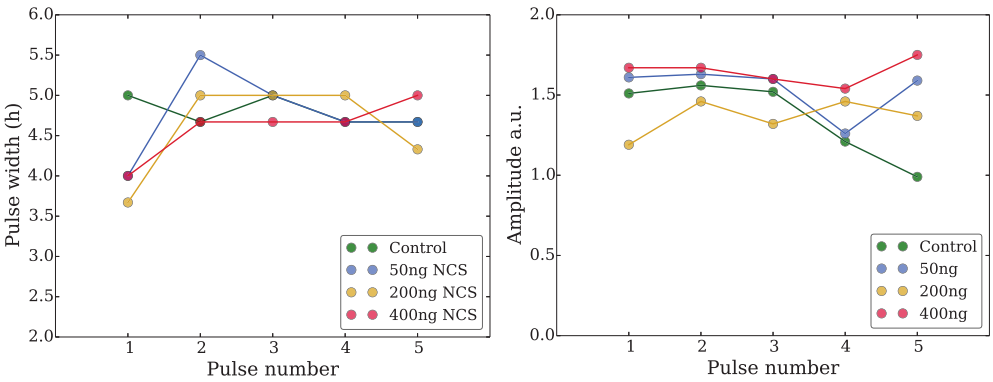

(a) Median of the pulse widths for selected stimulation strengths. The median pulse width is 5.0 hours for the control data set, and 4.67 hours for the other conditions shown in the plot.

(b) Median amplitudes for selected stimulation strengths. There is no significant variation in amplitudes in between the different conditions.

Figure 1.10.: Analysis of pulse shapes characterized by width and amplitude. The pulse shape is essentially the same for all conditions and is therefore a robust property of the p53 dynamics.

To further illustrate the dependence of the regularity of the dynamics on the stimulation strength, box plots of the IPI distribution for all conditions are shown in figure 1.11. The IPI distribution for the cells with the strongest stimulation fairly matches the one found for the noisy limit cycle oscillator presented in figure 1.4. Consequently, oscillatory dynamics are certainly a possible dynamical regime of the p53 dynamics, but are not sufficient to explain the dynamics of the weak or non stimulated cells.

The next question one may ask is about how stationary the observed dynamics are. Meant by that is, if a certain pulsatile regime stays the same for the whole observation time, or if the characteristics of the pulsing changes over time. Again, the IPI distribution can serve as a measure to address this question. This time, only the first IPI right after stimulation and the last IPI recorded are analyzed. If the pulsatile dynamics are stationary, the same IPI distributions are to be expected. However, as shown in figure 1.12, for the weak to medium stimulated cells these distributions shift to larger medians and inter quartile ranges comparable to the control conditions. It follows that the pulsing activity

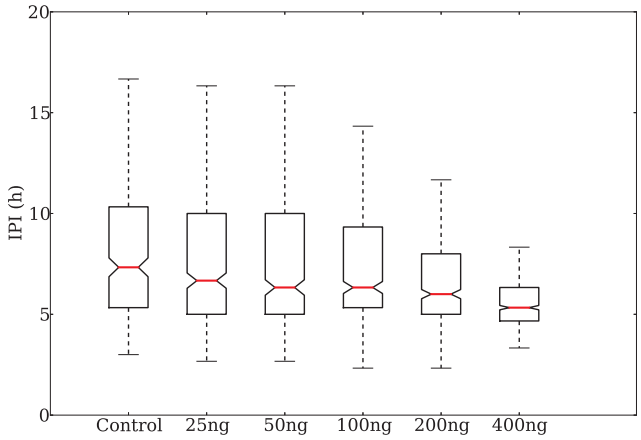

Figure 1.11.: Box plots of the IPI distributions for all experimental conditions. The median and the inter quartile range of the IPIs increase with decreasing stimulation. This indicates for non oscillatory behavior for the weak or non stimulated cells.

of the cells is time dependent, and is more regular right after stimulation. Taking into account that the induced DSBs get repaired over time, a *reset* of the p53 dynamics to basal dynamics is biologically evident. It is noteworthy that the cells stimulated with 400ng of NCS do not return to basal like dynamics even after 48 hours and that the unstimulated cells show a stationary behavior.

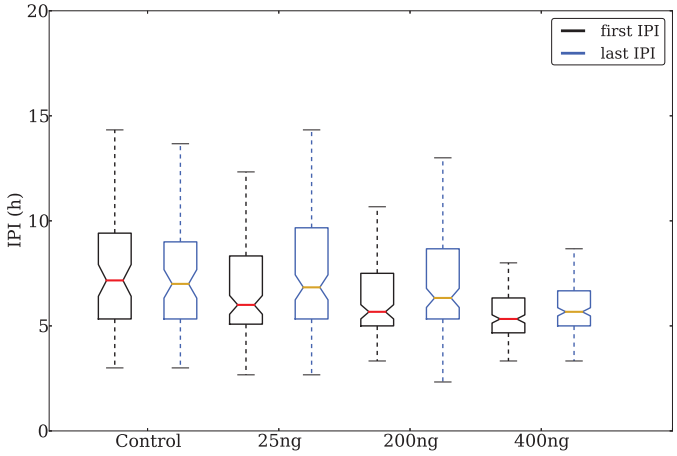

Figure 1.12.: Box plots of the IPI distributions of the first and last IPI observed for selected conditions to test for stationarity. The weak and medium stimulated cells show control-like IPI distributions at the end of the observation period, indicating a return to unstimulated behavior.

1.3. Modeling theory

In this chapter some fundamental theoretic concepts used for the construction of the p53 model shall be introduced. At first some general remarks about modeling cellular processes with ordinary differential equations (ODEs) are given. It follows a brief discussion of negative feedback oscillators, and their general properties. These get illustrated by modeling the core negative feedback motif of the p53 system, as often found in the literature [34, 65]. Finally the dynamical concept of excitability is thoroughly introduced exemplified by the classical FitzHugh-Nagumo model.

1.3.1. Preface - dynamical systems theory and biochemical reaction networks

The general definition of an autonomous dynamical system comprised of N state variables $x_1, ..., x_N$ is as follows

$$\frac{d}{dt}x_i = F_i(x_1, ..., x_N), \tag{1.2}$$

that defines a system of N coupled ODEs. The time evolution of one variable x_i can generally depend on the state of all other variables including x_i itself and is given by the potentially nonlinear vector-function F_i. In the framework of biochemical reaction networks, these variables represent concentrations of chemical species, e.g. metabolites, enzymes or transcription factors.

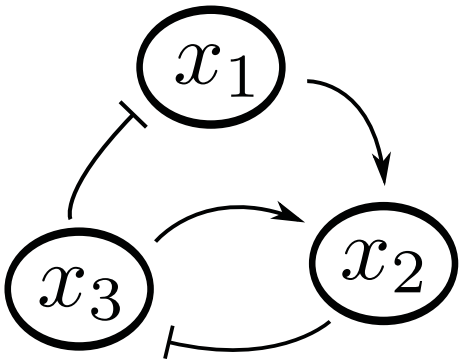

Figure 1.13.: An example of a reaction network with three state variables. x_1 is an activator of x_2, which is an inhibitor of x_3. The species x_3 in term is an inhibitor of x_1 closing the positive feedback loop. It is also an activator of x_2, therefore also establishing a negative feedback.

Often a reaction network is presented as a directed graph, as in figure 1.13. Every direct link, $x_j \to x_i$ or $x_j \dashv x_i$, between two species implicates a molecular interaction and therefore x_j actually appears inside F_i. The notion of directed links only makes sense, if the interactions between different state variables are

monotone. That means that either

$$\frac{\partial}{\partial x_j} F_i(x_1, ..., x_N) > 0 \text{ for all } x_j > 0, \tag{1.3}$$

in that case x_j is an *activator* of x_i, or

$$\frac{\partial}{\partial x_j} F_i(x_1, ..., x_N) < 0 \text{ for all } x_j > 0. \tag{1.4}$$

The last statement determines x_j to be an *repressor* of x_i.

Monotonicity secures that the effect of some species x_i on another species x_j always has the same direction. This property is unusual when studying general dynamical systems theory, but quite evident when applying this theory to biochemical reaction networks. This just means that a molecule either promotes or inhibits the production of some other molecule, it can never do both. This is an inherent characteristic of e.g. enzymes or transcription factors. A kinase always promotes the formation of its phosphorylated substrate, a transcription factor switches a gene either on or off and so on.

Another constraint when using dynamical systems theory to describe biochemical dynamics is that all state variables have to remain positive, as there are no negative molecule numbers. This confines the state space to the positive orthant given by $O_1 = \{x_i \geq 0, \text{ for all } i\}$. That further implies that the flow at the orthant boundaries is transverse, i.e. $F_i(x_1, ..., x_n) > 0$ for all $x_{j \neq i} > 0$. This condition assures that a trajectory started inside O_1 will remain in it for all times.

A last constraint refers to the finiteness of the amount of molecules present inside a cell. In mathematical terms this translates to the condition, that there is an arbitrary large but finite region $A \subset O_1$ for which $\lim_{t \to \infty} x(t) \in A$ holds. That means that all possible solutions $x(t)$ are bounded. In practice this is often assured by linear degradation terms or conservation rules.

An important concept borrowed from control theory involves the notion of feedbacks [94]. A feedback implies a closed loop in a reaction network, that means there is some path connecting a species with itself, i.e. $x_i \to x_j \dashv ... \to x_i$. If the number of repressing interactions along this path is odd, one refers to a *negative feedback*, elsewise it establishes a *positive feedback*. Feedback mechanisms are one general concept to explain how cells can reach homeostasis even under a constantly changing environment. Remarkably, even though biomolecular networks can be of arbitrary complexity, a small set of feedback motifs seems to be sufficient to explain their structure [1, 71].

All direct interactions to be modeled between molecular species x_i and x_j are specified in the functions F_i and are only constricted by the monotonicity, positivity and boundedness constraints given above. However, in practice one often finds ODE systems solely comprised of functions like the ones given in table 1.2. The development of rate equations for chemical reactions started with simple anorganic reactions were first and second order kinetics were sufficient to describe the observed concentration dynamics. Later in biochemistry when enzymatic reactions became important, saturated kinetics as for the popular

Michaelis-Menten kinetic were developed. Including cooperativity as important for e.g. ligand binding led to the highly nonlinear Hill equations. For the development of all these mathematical formulations, the underlying molecular interactions were precisely known. This is not generally true when dealing with cellular processes like transcription [11, 92] or protein degradation [12]. However, it turned out that these now phenomenological equations can still to some extend capture the dynamics that are observed inside living cells. Saturated kinetics are a natural choice if there is some rate limiting step. This is for example the case for transcriptional activation of a gene by a transcription factor. As there is a finite amount of TF binding sites, the rate by which a gene is transcribed should become independent from the TF concentration once all binding sites are occupied. The question about how applicable a specific model is and how well it is suited to deliver quantitative results can only be answered case-by-case by concomitant experiments.

Table 1.2.: Overview of prominent functions used to describe biomolecular process. These terms and combinations thereof can occur as the r.h.s. of a biochemical rate equation for x. The parameter a describes a basal rate, k is the Michaelis constant and n is the Hill coefficient.

term	**name**	**modeling objective examples**
C	zero-order kinetic	constant mRNA transcription
$a\ y$	first order kinetic	protein maturation from mRNA y
$a\ x\ y$	mass-action kinetic	degradation by y
$a\frac{y}{y+k}$	Michaelis-Menten kinetic	transcriptional activation by y
$a\frac{y^n}{y^n+k^n}$	Hill kinetic	cooperative transcriptional activation by y
$a\frac{1}{1+(y/k)^n}$	Hill repressor	cooperative repression by y

1.3.2. Negative feedback oscillators

A negative feedback oscillator is a dynamical system comprised solely of negative feedbacks which exhibits a limit cycle regime. Such systems are deployed for a wide range of biological phenomena, including circadian rhythms, cell division, gene regulation and glycolysis [38]. Models of such biochemical oscillators, e.g. the Goodwin oscillator [40], always include at least one sufficiently nonlinear

negative feedback motif. Such motifs are frequent in molecular biology, as means for autoregulation and homeostasis. A typical example is a gene activating its own repressor, a scheme to be found for about 40% of all transcription factors in E. coli [8].

An important subclass of such negative feedback systems are cyclic systems. These are build from pure loop structures, for which equation 1.2 simplifies to

$$\frac{d}{dt}x_i = F_i(x_i, x_{i-1}). \tag{1.5}$$

The condition $\prod_{i=1}^{N} \mathrm{sgn}(\frac{\partial F_i}{\partial x_{i-1}}) = -1$ assures that there is an odd number of repressing interactions which establishes the negative feedback loop. The function denoted by $\mathrm{sgn}(x)$ is the sign function, which gives -1 for $x < 0$ and $+1$ for $x > 0$. The route to oscillations for such monotone cyclic systems has been theoretically investigated by many authors [44, 66, 78, 106], and the main results are the following:

1. There is only one stable fixed point x^*
2. Destabilization of x^* can occur only via a Hopf bifurcation

The proofs heavily rely on the monotonicity constraint and the cyclic structure defined in equations 1.3,1.4 and 1.5. A not overly mathematical rigorous version of the proof can be found in the appendix of ref. [78]. The actual functional forms of the molecular interactions formulated in the F_i's are not important for these results. In addition, Hopfs theorem implies the existence of a periodic orbit. The stability of that periodic orbit spawned at the bifurcation point is assured by the boundedness of the system, stipulated in the previous section 1.3.1. This very specific route to oscillations via a supercritical Hopf bifurcation involves distinct qualitative features of the dynamics, to be discussed and exemplified in the following paragraphs.

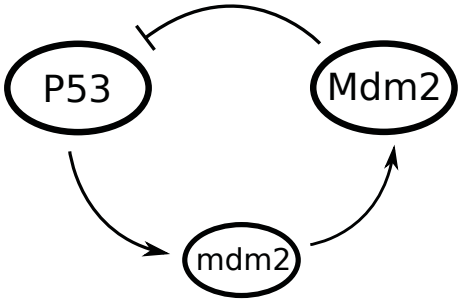

Figure 1.14.: The canonical p53 autoregulatory loop. The protein P53 acts as transcription factor for the mdm2 mRNA, whereas the matured Mdm2 protein tags P53 for degradation . This constitutes a monotone cyclic negative feedback loop system.

The basic regulatory scheme of p53 introduced in section 1.1.1 fulfills exactly the properties of a monotone cyclic negative feedback system, shown in figure 1.14. The three species involved are the p53 protein $P53$ which induces transcription

of the Mdm2 precursor mRNA $mdm2$ and its matured protein $Mdmd2$. This E3-ligase tags p53 for degradation via the proteolytic pathway and closes the negative feedback loop. Many p53 models obeying this structure have been devised [34], here the following formulation was chosen:

$$\begin{aligned} \frac{d}{dt}P53 &= C - \ g\ Mdm2\ \frac{P53}{k_{mp}+P53} - d_P\ P53 \\ \frac{d}{dt}mdm2 &= T_m\frac{P53}{k_{pm}+P53} - d_m\ mdm2 \\ \frac{d}{dt}Mdm2 &= T_M\ mdm2 - d_M\ Mdm2. \end{aligned} \tag{1.6}$$

The parameter C describes the constant inflow of p53 proteins given the unregulated and constant transcription and translation of that gene. Degradation of the three species is given by the rates d_P,d_m and d_M respectively. This model incorporates two saturating terms. The maximal degradation rate of $P53$ mediated by $Mdm2$ is given by the parameter g, and the maximal rate by which $P53$ can promote $mdm2$ transcription is limited by T_m. The Michaelis constants k_{mp} and k_{pm} determine the half maximum concentrations. The underlying assumptions for using Michaelis-Menten kinetics were already discussed for the case of transcription in the preceding section 1.3.1. The arguments mainly repeat in the case of the proteolytic degradation of p53. Rate limiting steps here include e.g. the finite amount of accessible proteasomes for ubiquitinated p53. The maturation of the Mdm2 protein is described by first order kinetics with the translation rate T_M.

In accordance to the mathematical results about stability for negative feedback loops stated above, a bifurcation analysis of this p53 system reveals a limit cycle regime bordered by two supercritical Hopf bifurcations. The bifurcation parameter, as depicted in figure 1.15, is the degradation rate d_M of the Mdm2 protein species. Inside the "Hopf bubble" the system undergoes sustained oscillations, with an amplitude strongly dependent on the parameter value of d_M. The choice of this parameter is particularly reasonable given the biological evidence, that the main DSB sensor protein ATM directly phosphorylates Mdm2 and thereby induces its autoubiquitination and degradation[70, 96].

To illustrate how such oscillators perform when changing the dynamical regime, a time dependence of the parameter d_M is introduced according to figure 1.16. A fast exponential rise of the degradation rate is followed by a constant rate and eventually a slow decay. This mimics the dynamical DSB response in a simplified way comparable to ref. [65], although no real physiological relevance is actually desired here. When moving inside the limit cycle regime negative damped dynamics are observable. These occur in the beginning mainly because of transient dynamics. The strong dependence of the amplitude on the numerical value of d_M implies damped oscillations when moving inside the "Hopf bubble". During the transition back to the steady state regime damped oscillatory dynamics are additionally observable after passing the Hopf bifurcation point.

This damped regime is understandable by recalling, that a Hopf bifurcation is

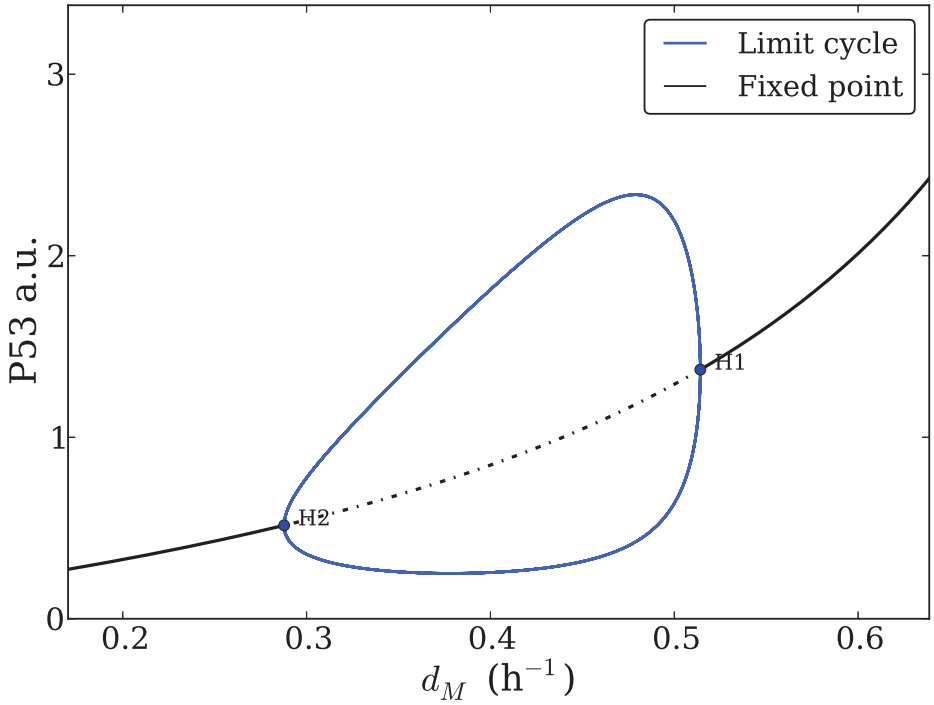

Figure 1.15.: Bifurcation diagram of the p53 negative feedback loop model. The bifurcation parameter d_M is the degradation rate of the Mdm2 protein, as defined in equation 1.6. Oscillations occur inside the *Hopf bubble* bordered by the two Hopf bifurcations denoted by H1 and H2. The amplitudes of the limit cycles are given by the lower and upper bounds in blue and vary greatly.

defined by the crossing of the imaginary axis by a pair of conjugate eigenvalues $\lambda_{1,2} = \alpha \pm i\beta$. This means, that close to the bifurcation point complex eigenvalues with arbitrary small negative real part exist. They give rise to oscillatory components of the trajectory when perturbed from the steady state with a period $T \approx \frac{2\pi}{\beta}$. Hence, damped oscillatory regimes exist in the vicinity of a Hopf bifurcation and can not be avoided even by very fast transitions. Such an instant transition into the "Hopf bubble" may also give rise to an overshoot, as can be seen in figure 1.17. For the bifurcation parameter $d_M > 0.81$ the conjugation expires, the imaginary parts become zero and the real part branches into two distinct values. Only here the system settles down to the fixed point without damped oscillations.

In summary the distinct qualitative features of the dynamics of negative feedback oscillators are the following:

1. The amplitude of the limit cycle is strongly dependent on the bifurcation parameter

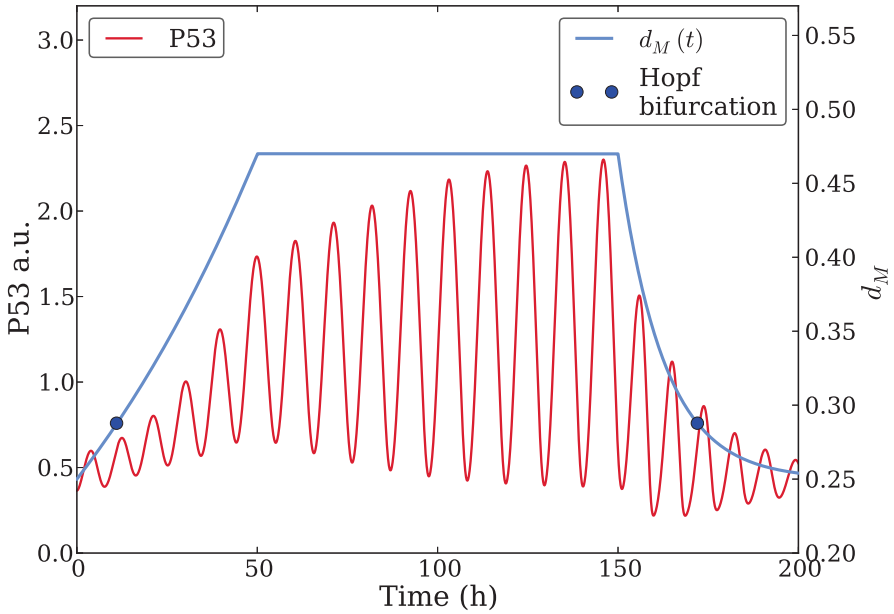

Figure 1.16.: Switching a negative feedback oscillator *on* and *off*. The bifurcation parameter d_M is made explicitly time dependent and follows the dynamics shown in blue here. This moves the system in and out of the limit cycle regime, given between the marked Hopf bifurcation points. A (negative) damping is observable at both sides of the transition.

2. Switching the oscillator on or off implies observable damped oscillations

3. As a corollary no isolated pulses can be generated

By recalling some features of the observed pulsatile p53 dynamics studied in section 1.2, i.e. the presence of isolated pulses as in figure 1.8 for the weak stimulated cells, negative feedback oscillators are very limited in accurately describing the full dynamical range of the p53 system.

1.3.3. Introduction to excitability - case study FitzHugh Nagumo

The classical prototype of an excitable system is the FitzHugh-Nagumo (FN) model [33]. It was suggested in as early as 1961 as a 2-dimensional simplification of the original 4-dimensional Hodgkin-Huxley model [47], which describes in detail the voltage and current dynamics of a spiking neuron. To introduce the concept of excitability, the dynamics and bifurcations of the FN model shall be discussed in the following.

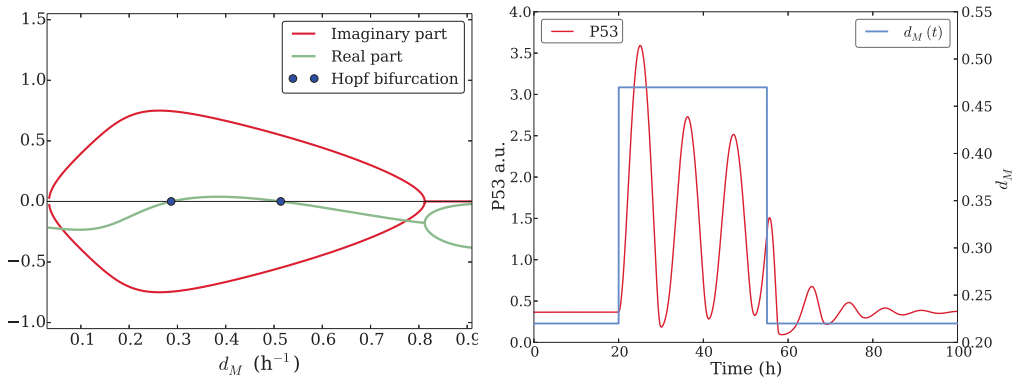

(a) Numerical values for the conjugate eigenvalue pair constituting the Hopf bifurcations. The real part determines the stability of the fixed point, whereas the imaginary parts cause the oscillatory components of the trajectory.

(b) An instant transition into the limit cycle regime may trigger an overshoot which eventually relaxes on the limit cycle. An instant exit not too far from the Hopf bifurcation generally implicates damped oscillatory dynamics.

Figure 1.17.: (a) Eigenvalues of the fixed point for an extended range of the bifurcation parameter d_M. (b) Trajectory of the system for instant transitions in and out of the limit cycle regime.

The system is given by the equations

$$\begin{aligned} \epsilon \frac{dx_1}{dt} &= x_1 - x_1^3 - x_2 + I \\ \frac{dx_2}{dt} &= \gamma x_1 - \beta x_2 + b. \end{aligned} \tag{1.7}$$

Here the parameter $\epsilon \ll 1$ introduces a time-scale separation, making x_1 the fast and x_2 the slow variable. The parameters γ,β and b are dimensionless variables and the parameter I plays the role of an external stimulus. Because the system is only 2-dimensional, phaseplane analysis is applicable and is sketched in figure 1.18.

The cubic nullcline for the x_1 variable and the linear nullcline for the x_2 variable intersect at the fixed point, which is stable for the excitable regime. Small perturbations from that fixed point can lead to huge excursions through the phasespace, as exemplified by two trajectories in figure 1.18. This behavior stems from the strong timescale separation, here an $\epsilon = 0.05$ was chosen, and can be understood geometrically. After the perturbation the system quickly moves horizontal till it reaches the x_1 nullcline. Now the slow dynamics in x_2 direction are dominant until the maximum of the x_1 nullcline is reached, and the system quickly moves back to the left branch of the cubic nullcline. From there it slowly settles back to steady state. The specific orbit and therefore the amplitude of such an excitation loop is dependent on the initial conditions. Such

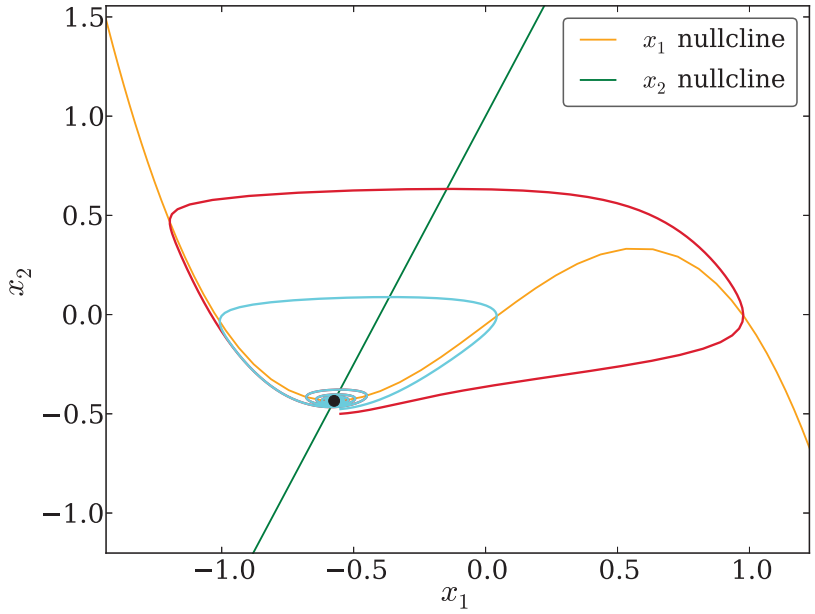

Figure 1.18.: Phaseplane for the FN model in the excitability class II regime. The nullclines intersect at one point giving the stable fixed point. A small perturbation from that fixed point leads to a wide excursion in phasespace. Different perturbations lead to different orbits, as shown with the red and the cyan trajectory.

systems with a strong time-scale separation are also called relaxation oscillators [73]. The oscillating regime is in the FN model reached via a supercritical Hopf bifurcation, as depicted in figure 1.19. The amplitudes of the limit cycles grow very fast with the bifurcation parameter I, and the oscillatory pulses for the fast variable x_1 are very spiky. These are both consequences of the strong time-scale separation. It is worth mentioning, that relaxation oscillators do not belong to the class of negative feedback oscillators.

Excitable regimes are generally close to bifurcations which result in oscillatory behavior. The authors of ref. [49] identified two types of excitability, given by the type of the bifurcations nearby. They are named class I and class II excitability. Relaxation oscillators generally belong to class II systems, characterized by arbitrary small amplitudes of the excitation loops and nonzero frequency at the onset of the oscillations. Interestingly, the FN model also has an excitability class I regime, for which the nullclines intersect at three points as shown in figure 1.22. For that regime, no strong time-scale separation is needed, and the corresponding parameter is relaxed to $\epsilon = 0.5$.

The bifurcation scheme is a bit more complicated here, as sketched in figure 1.20. An analysis for codimension one bifurcations reveals two saddle-node and two Hopf bifurcations. The middle fixed point is always a saddle, whereas the two outer fixed points are foci, which loose stability via the subcritical Hopf

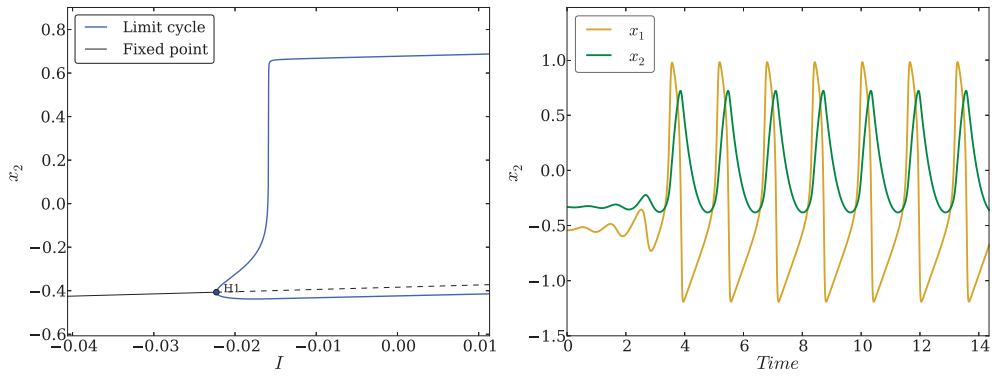

(a) Supercritical Hopf bifurcation for the bifurcation parameter I. The amplitudes of the limit cycle grow very quickly.

(b) The oscillatory pulses of the fast variable are very spiky which is typical for relaxation oscillators.

Figure 1.19.: (a) Hopf bifurcation of the FN model in the excitability class II regime. (b) Trajectories of the system in the limit cycle regime.

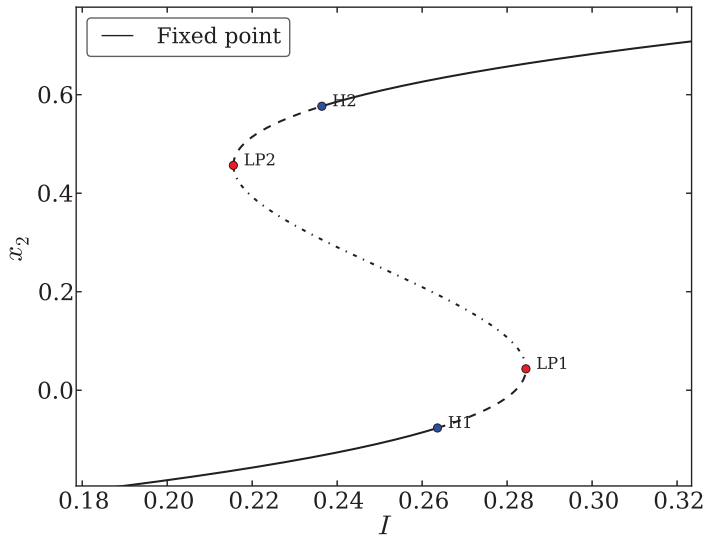

Figure 1.20.: Bifurcation analysis of the FN model for the parameter I with $\gamma = 0.8$. The system has three fixed points in the interval $I \in [0, 214.., 0.283..]$, this allwos for an excitability class I regime. A saddle and the unstable focus are born via the two saddle-node bifurcation points *LP1* and *LP2*. The two outer equilibria become stable via the two subcritical Hopf bifurcations *HP1* and *HP2*.

bifurcations indicated by *H1* and *H2* in the bifurcation diagram.

To extend the characterization of the system, a codimension two bifurcation analysis with the parameters I and γ was performed. The latter parameter

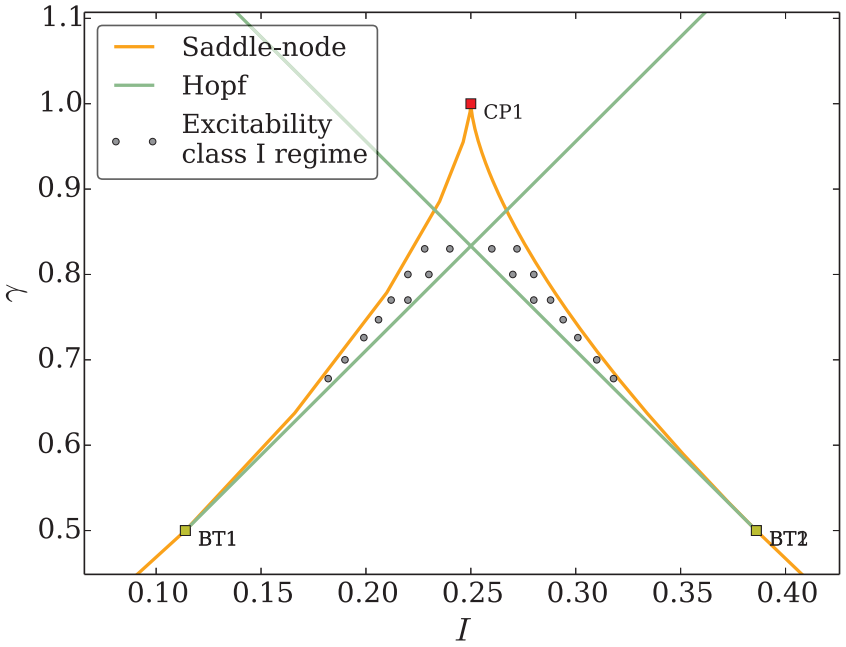

Figure 1.21.: Bifurcation set for the two parameters I and γ. Two codimension 2 bifurcations take place. The two saddle-node points collide and disappear via the Cusp bifurcation *CP1*. Additionally the two Hopf bifurcations collide with the saddle-node points at the Bogdanov-Takens bifurcations *BT1* and *BT2*. The parameter range for the excitability class I regime ends when the two Hopf curves cross at $\gamma = 5/6$.

γ determines the slope of the x_2 nullcline. As can be seen in figure 1.21 the saddle-node points *LP1* and *LP2* collide with the Hopf points at the Bogdanov-Takens points *BT1* and *BT2*. Furthermore a cusp bifurcation happens for $I = 0.25$ and $\gamma = 1$ where the two saddle-node curves collide and disappear. The three fixed points merge to one stable fixed point and the excitability class II regime lays right above this cusp bifurcation. The system is highly symmetric so there are actually two excitability class I regimes, they are characterized by the co-existence of one stable fixed point, one saddle and one unstable fixed point. The corresponding parameter range is annotated in figure 1.21.

A saddle is a hyperbolic equilibrium with at least one negative real eigenvalue. In the two dimensional case of the FN model it is exactly one. As a corollary there is a stable manifold which is also called *separatrix*. The separatrix separates the phase space into regions with different qualitative behavior. In the context of excitability it serves as a direction dependent threshold. Any trajectory started below the separatrix will do a full excitation loop around the upper right fixed point and will eventually settle down at the stable fixed point which is a focus in the FN model. Any trajectory started above the separatrix will undergo subthreshold damped oscillations. The phaseplane portrait in figure

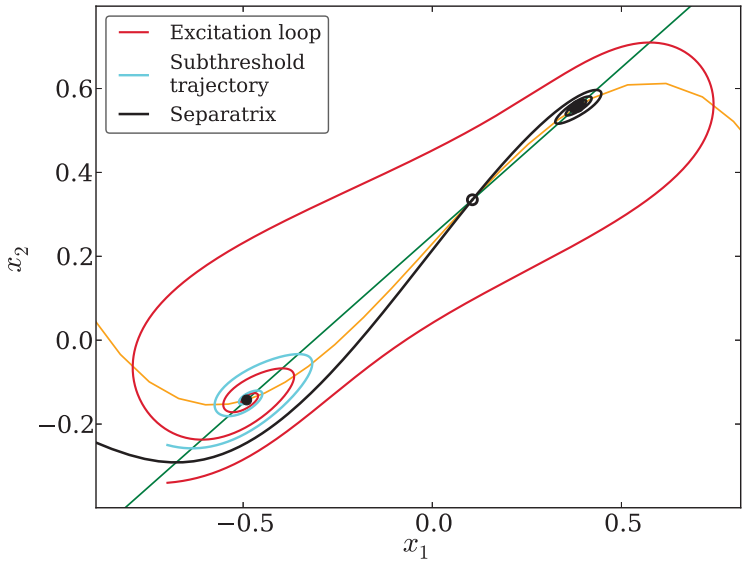

Figure 1.22.: Phaseplane for the FN model in the excitability class I regime. The nullclines intersect at three points giving one stable focus, a saddle in the middle and an unstable focus in the upper right. Perturbations which cross the separatrix lead to an excitation loop, perturbations which do not cross the separatrix lead to subthreshold dynamics. Parameters are $I = 0.23$ and $\gamma = 0.8$.

1.22 illustrates these dynamics. Perturbations leading to an excitation loop must cross the separatrix, and therefore the threshold is direction dependent. A stable manifold of the saddle merges with the unstable manifolds from the upper unstable focus, this is called a heteroclinic connection. The excitation orbits are robust with respect to the initial conditions. That means that as long as the threshold is crossed, the amplitudes of the ensuing pulses are all very similar as can be seen in figure 1.23.

As stated earlier, excitable regimes are always close to bifurcations leading to limit cycle regimes. The excitability class I regime of the FN model is close to a saddle-node on a limit cycle (LPC) bifurcation [56]. This happens when moving out of the excitable regime in positive γ direction, so right above the crossing of the Hopf curves in figure 1.21. The unstable limit cycles originating at the Hopf points collide with a stable limit cycle at the LPC points, as depicted in the bifurcation diagram in figure 1.24a.

In summary excitability class I systems exhibit excitation loops which show very similar orbits, as long as the direction dependent threshold, the separatrix, is crossed. This carries on to the onset of oscillations, which are born with large amplitudes and show only little dependence on the bifurcation parameter. No time separation is needed, as the excitability stems from the specific phasespace structure. That is the co-existence of a saddle as organizing center, one stable and one unstable fixed point. Excitability class I regimes can typically be found

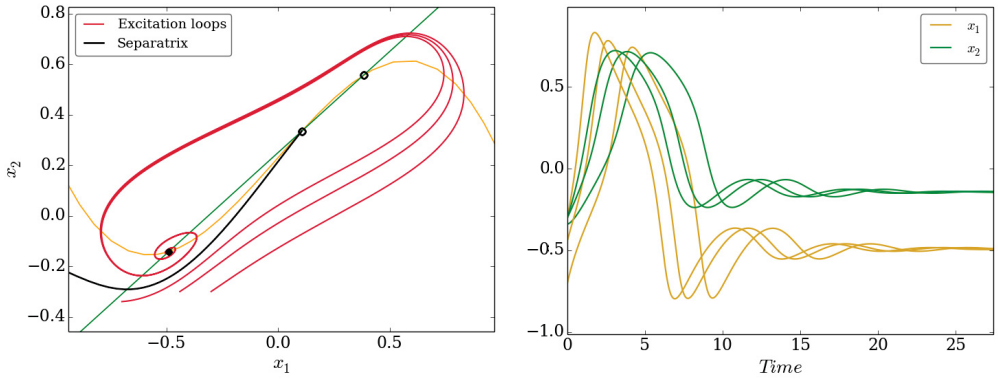

(a) Three different excitation loops, started with different distances from the separatrix.

(b) Corresponding time series for the three excitation loops shown in panel (a). The pulse shapes and amplitudes are very similar.

Figure 1.23.: As long as the threshold is crossed, different initial conditions lead to very similar orbits in excitability class I systems.

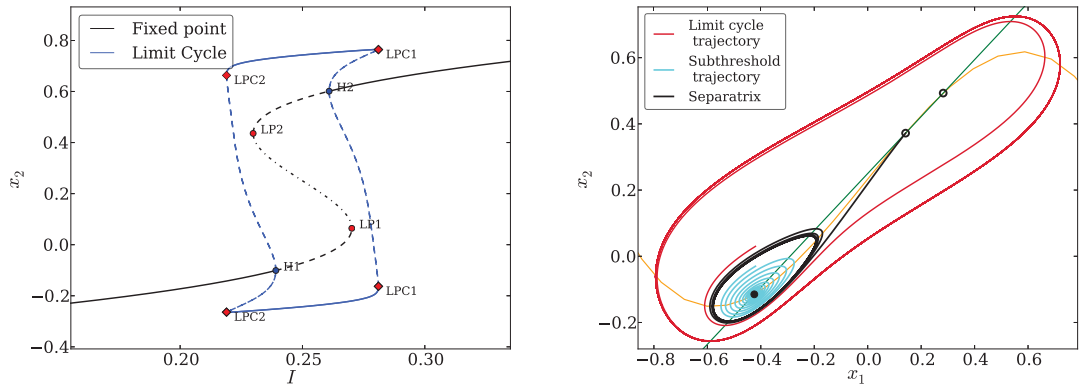

(a) Saddle-node on a limit cycle (LPC) bifurcations mark the onset of large amplitude oscillations. The excitable regime has disappeared. This bifurcation diagram corresponds to the horizontal line at $\gamma = 0.85$ in figure 1.21, right above the crossing of the Hopf curves.

(b) Phaseplane of the FN model for parameters $I = 0.23$ and $\gamma = 0.85$. The separatrix now separates limit cycle trajectories from trajectories approaching the stable focus. The separatrix itself converges to a limit set, corresponding to an unstable limit cycle, which separates the stable limit cycle and co-existing stable focus.

Figure 1.24.: Oscillating regime of the FN model right after the excitability class I regime has disappeared via LPC bifurcations.

in the vicinity of Cusp bifurcations, because they mark the appearance of three

fixed points via pairwise saddle-node bifurcations. A bifurcation nearby leading to oscillations is the LPC bifurcation, the emerging stable limit cycles have an arbitrary small frequency. However, in practice the period often follows a relationship like $T_{osc}(\alpha) \sim T_{osc} + \frac{1}{\alpha_c - \alpha}$, with α_c being the critical point of the LPC bifurcation.

1.4. The ATM-Wip1 switch building block

As outlined in the introductory section 1.1 the protein kinase ATM is the major signalling molecule of the cellular response to DSB, after activation it phosphorylates numerous downstream effectors such as P53 directly. Phosphorylation itself is an ubiquitous post-translational modification of proteins. It can rapidly alter the stability and the functional state of substrates. Moreover it occurs often in cascades along a signalling pathway. A prominent example is the MAP kinase pathway, where a signal coming from a receptor on the cell membrane is transmitted via a kinase cascade into the nucleus to eventually alter the transcriptional program of the cell [21].

If kinase activity and therefore phosphorylation is a general mechanism to activate a signalling pathway, it is evident that de-phosphorylation carried out by phosphatases is the antagonist in such a framework. For the DDR to DSBs the phosphatase Wip1 was identified to fulfil that role [87]. Remarkably the name Wip1 stands for "Wild-type p53-induced phosphatase 1", as it was first characterized as inducted after IR in a P53 dependent manner [32]. Because P53 itself gets stabilized by ATM, and Wip1 dephosphorylates and therefore deactivates ATM directly [87] a simplified feedback loop maybe written as $ATM \rightarrow P53 \rightarrow Wip1 \dashv ATM$. Therefore the kinase positively regulates its own phosphatase and this negative feedback closes one phosphorylation-dephosphorylation cycle. This scheme is also found for other kinases, for example ERK from the MAP kinase pathway directly activates its own phosphatase DUSP6 [100].

In the following such a generic phosphorylation-dephosphorylation system shall be developed by the example of ATM and Wip1. The positive feedback required to describe the observed ATM dynamics turned out to be sufficient to serve as the basis of an excitable p53 model.

1.4.1. ATM as Signalling Switch

ATM is a large protein which consists of 3056 residues. It has many modification and interaction domains, and it has indeed an extensive list of targets [86]. Its functional interactions span a huge network, not only in cellular response to DSBs but also for example in chromatin organization and metabolism. In the following the focus lies solely on the DDR response, and here it is the prominent signalling molecule in response to DSBs [60, 82].

In unstressed conditions ATM is present as inactive homodimers in the cell. After induction of DSBs ATM gets rapidly phosphorylated and dissociates into monomers which is the catalytic active form. It was further shown that this phosphorylation is strongly dependent on the presence of active ATM itself,

which revealed that autophosphorylation takes place [4]. Active ATM then phosphorylates the histone variant H2AX in the vicinity of a damage loci. These regions of γH2AX quickly expand and can elongate up to a few mega basepairs. Using immunostains of γH2AX, these sites are clearly visible as foci under the microscope [31]. Subsequently the Mre11-Rad50-Nbs1 (MRN) complex gets recruited to the site, which is reported to enhance H2AX phosphorylation by ATM. The MRN complex is a mediator who recruits additional substrates to ATM and to the foci, it is also directly involved in DNA repair [27, 60]. Moreover it is itself a substrate of the ATM kinase, establishing a positive feedback $ATM \rightarrow \gamma H2AX \rightarrow MRN \rightarrow ATM$. The precise mechanisms of ATM activation are very complex and are still not entirely resolved, but it is clear that active ATM is required for foci formation which in turn enhances ATM activation [43, 59, 86]. To what extend complete ATM localization at the damage loci is important for its activation is also still debated. Nevertheless it is reported that over 50% of the cellular ATM is activated within the first 5 minutes after a low dose of irradiation [4]. So it appears that ATM activation acts like a switch which is dose independent and very fast.

Instead of trying to model all details of this intricate ATM activation process, the focus lies on capturing the switch dynamics rather phenomenologically. In terms of dynamical systems, a switch can be modeled by a bistable system. Bistability is long studied for chemical and biological systems, and one of the main theoretic results is, that positive feedbacks are necessary for multiple steady states [17, 112].

A simple model that exhibits bistability may be written as

$$\frac{d}{dt}ATM^* = A\frac{ATM^{*2}}{k_a + ATM^{*2}} - d_A ATM^*. \tag{1.8}$$

Here, the variable ATM^* denotes active monomeric ATM. The saturation of the first term represents various cellular factors limiting autophosphorylation and activation of ATM. As depicted above many different molecules actually play a role in this process, all of them may be restricting. The parameter A describes the maximal rate by which active ATM may be produced, the parameter d_A sets its lifetime.

A graphical stability analysis can be done by plotting the r.h.s. of equation 1.8. The crossings of the x-axis in figure 1.25a mark three fixed points and their local stability can be inferred from the sign of the r.h.s. in the respective vicinity. In the plot the dynamics around the fix points are symbolized by arrows. The system exhibits two stable FPs separated by an unstable FP which serves as a threshold. As shown in figure 1.25b the system settles down to the *off* state when started below the threshold and evolves to the *on* state when started above. The threshold value tunes the sensitivity of the switch, the larger it is the more robust is the off state against perturbations.

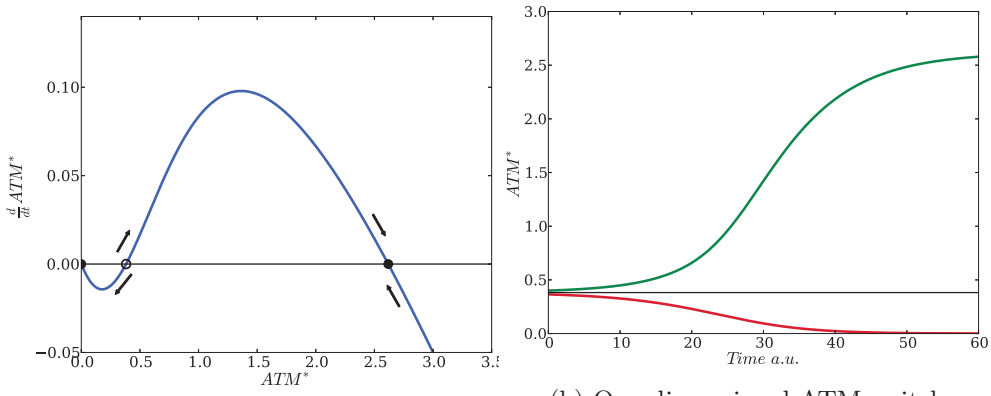

(a) Graphical stability analysis of the ATM switch. The flow is indicated by arrows. The stable off state is separated from the stable on state by an unstable node.

(b) One dimensional ATM switch dynamics. Any trajectory started below the threshold settles down to the off state. Trajectories started above the threshold will evolve to the on state.

Figure 1.25.: The one dimensional ATM switch.

This description is sufficient to model ATM activation, yet the shutdown of the damage signal once the DSBs are repaired is of equal importance. The downregulation of active ATM is done by its antagonist, the phosphatase Wip1. From the modeling perspective, its action must destabilize the on state of the ATM switch.

1.4.2. Incorporating the Phosphatase Wip1

Studies involving mouse models describe Wip1 as an oncogene, which counter acts the tumor suppressing function of P53. Moreover overexpression of Wip1 was found to be functionally equivalent to P53 inactivation and is present in some tumors, e.g. breast cancer [13]. The molecular mechanism leading to that function of Wip1 were subsequently discovered. First ATM was identified to be a substrate of Wip1 in vivo, whereas depletion of Wip1 leads to an activation of ATM [87]. Detailed biochemical studies revealed many other targets of that phosphatase, most notably for the ATM mediated DSB response are P53,Chk2, γH2AX, Rad50 and Nbs1 [114].

The dephosphorylation of γH2AX and two members of the MRN complex (Rad50 and Nbs1) directly interferes with the positive feedback $ATM^* \rightarrow \gamma H2AX \rightarrow MRN \rightarrow ATM^*$, it is therefore assumed that Wip1 inhibits ATM activation processes. Taking also the direct dephosphorylation of active ATM modeled by mass action kinetics into account, Wip1 enters the equation 1.8 as follows

$$\frac{d}{dt}ATM^* = A\frac{ATM^{*2}}{k_a + ATM^{*2}}\frac{1}{1+\frac{Wip1}{k_{wa}}} - d_A ATM^* - P\ ATM^*\ Wip1. \quad (1.9)$$

The parameter k_{wa} determines the steepness of the inhibition and the parameter

P describes the rate at which Wip1 directly dephosphorylates ATM.

To study such ATM dynamics in a simplified model, it is assumed for now that ATM directly activates Wip1. This is an oversimplification and is solely done for simplicity and reduction of dimensions at this stage of the model construction. The full model presented in later sections will include P53 as an transcription factor for Wip1.

In the following ATM dependent Wip1 production is assumed to follow a saturated kinetic with maximal rate T_w:

$$\frac{d}{dt}Wip1 = T_w \frac{ATM^*}{k_{pw} + ATM^*} - d_w Wip1. \tag{1.10}$$

This two dimensional system resembles a so-called bistable frustrated unit which was studied as a minimal model for a self activating gene with oscillatory regimes [54].

By choosing appropriate parameters, this system exhibits excitability class I dynamics. There are 3 fixed points, one stable node, a saddle and an unstable focus. An excitation loop and the separatrix including the heteroclinic connection to the unstable focus are shown in figure 1.26. The phasespace structure is qualitatively equivalent to the FN model in the excitability class I regime as studied in section 1.3.3.

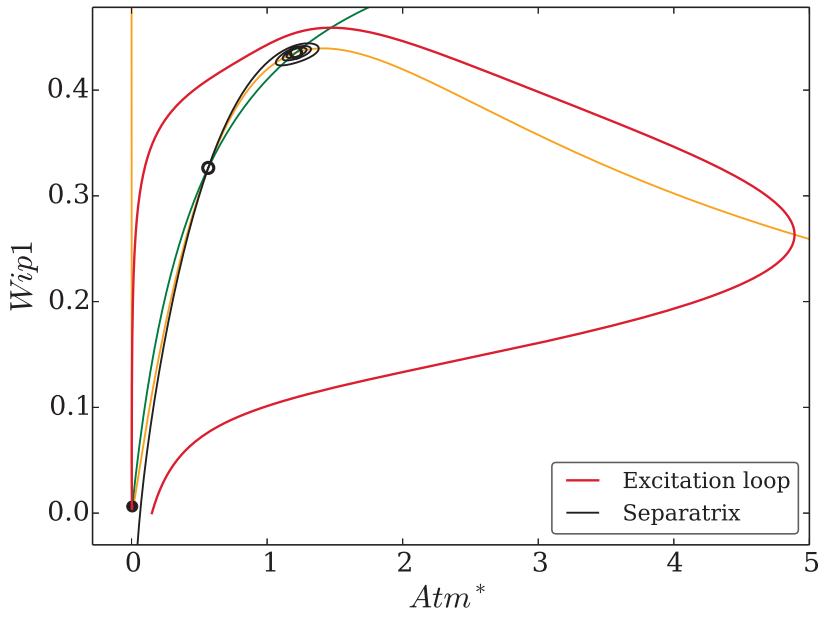

Figure 1.26.: Phaseplane for the simplified Atm-Wip1 model in the excitability class I regime. The nullclines intersect at 3 points, giving a stable node as the rest state, a saddle point with the incoming stable manifold as separatrix and an unstable focus in the upper right. When the system is initialized right the threshold a huge phasespace excursion occurs.

The specific orientation of the separatrix gives an effective threshold only with respect to ATM^*. Increased levels of $Wip1$ cause a higher threshold value in the ATM^* direction, but can not trigger an ATM kinase pulse alone. This molecule specific sensibility of the ATM-Wip1 modul is shown in figure 1.27.

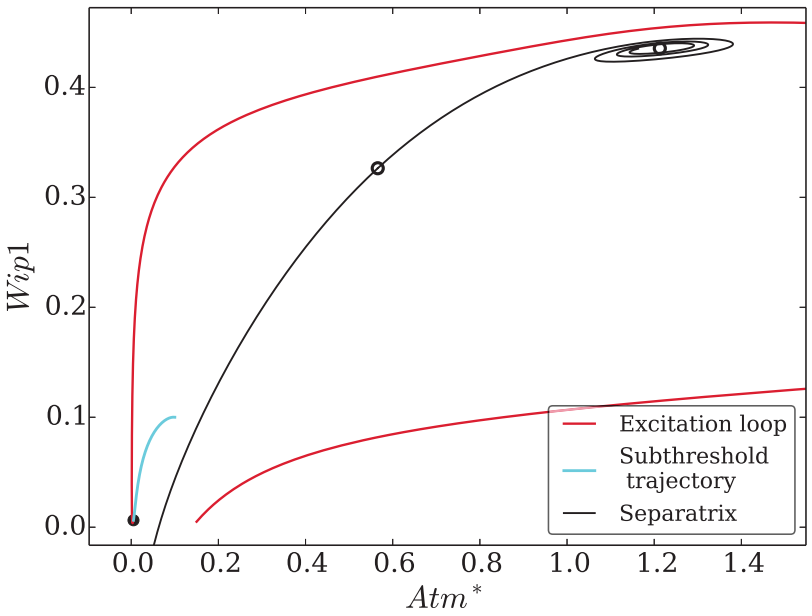

Figure 1.27.: A view in the phaseplane of the simplified ATM-Wip1 model shown in figure 1.26, The nullclines are omitted for better visibility. The orientation of the separatrix makes the system unresponsive to fluctuations in $Wip1$. Only a perturbation in ATM^* direction can trigger an excitation loop.

Direction dependent thresholds, as a typical feature of excitability class I regimes, are a natural way to reflect the robustness of a signaling network with respect to fluctuations in specific molecule species. ATM as the primary sensor molecule for DSBs has a high sensitivity towards small concentration gains caused by a few DSBs. However, fluctuations of the phosphatase Wip1 levels are not prone to trigger a deceptive ATM signal pulse.

This oversimplified model captures qualitatively the excitable activation of the ATM damage sensor and its subsequent inactivation by Wip1. Inside living cells, active ATM acts on the p53-Mdm2 regulatory loop. Only p53 stabilisation then leads to transcriptional activation of Wip1. The incorporation of these known interactions into the model and the propagation of the ATM excitability shall be elucidated in the following.

1.5. Including the core negative feedback loop - the full p53 model

1.5.1. The effectual modeled p53 network for the DSB response

The core negative feedback loop involving p53 and Mdm2 was already introduced in section 1.3.2, as was the damage sensor module involving ATM and Wip1 in the preceding section. The aim of this section is to bring these two submodels together and thereby construct the full p53 model for the response to DSBs.

The first new interaction is the phosphorylation of the Mdm2 protein by active ATM, which was already briefly introduced when studying the bifurcations of the core loop in section 1.3.2. The authors of ref. [96] showed that Mdm2 gets rapidly destabilized by DSB-dependent PI 3-kinase family members, where ATM belongs to. Phosphorylation and subsequent auto-ubiquitination followed by proteasomal degradation is the main mechanism for that. Hence, ATM^* enters the core negative feedback loop by promoting $Mdm2$ degradation. A simple mass action kinetics term was chosen to model that interaction. A second influence of ATM^* on the core loop is its reported weakening of the $Mdm2$ - $P53$ interaction. The p53 protein itself is a target of ATM^* and $Mdm2$ has a lower binding affinity to phosphorylated $P53$. As with the present data phosphorylated p53 can not be quantified, there is no additional species introduced into the model. Therefore, this mechanism is indirectly captured rather phenomenologically by inhibiting the $Mdm2$ dependent $P53$ degradation via ATM^* . The relative strength of this second ATM^* interaction is given by the parameter R in the model. The second extension so far concerns the transcriptional activation of Wip1 by p53. Transcription and subsequent translation and maturation of proteins happen typically on a time-scale of hours, as opposed to (de-)phosphorylation and ubiquitination which typically occur within minutes. By adding an explicit Wip1 mRNA species to the equations, as it was also done for Mdm2, these different time-scales get represented in the model without introducing explicit delays in the equations. Finally the initial trigger of the ATM activation are the DSBs, they enter the equation for ATM^* via the signal function $S \equiv S(DSB)$ to be specified later.

With these modifications and extensions the now complete p53 model is given by the following equations:

$$
\begin{aligned}
\frac{d}{dt}ATM^* &= A\frac{ATM^{*2}}{k_A + ATM^{*2}}\frac{1}{1 + Wip1/k_{WA}} - d_A ATM^* - P\ ATM^*\ Wip1 + S(DSB) \\
\frac{d}{dt}P53 &= C - d_P\ P53 - \ g\ Mdm2\ \frac{P53}{k_{MP} + P53}\left(1 + \frac{R}{1 + ATM^*}\right) \\
\frac{d}{dt}mdm2 &= T_m\frac{P53}{k_{Pm} + P53} - d_m\ mdm2 \\
\frac{d}{dt}Mdm2 &= T_M\ mdm2 - d_M\ Mdm2 - d_{AM}\ ATM^*\ Mdm2 \\
\frac{d}{dt}wip1 &= T_w\frac{P53}{k_{Pw} + P53} - d_w\ wip1 \\
\frac{d}{dt}Wip1 &= T_W\ wip1 - d_W\ Wip1
\end{aligned}
\tag{1.11}
$$

A graphical scheme of the modeled interaction network is shown in figure 1.28. The only new parameters are the halflife of the Wip1 mRNA d_w, the rate by which the Wip1 protein maturates T_W and the rate by which active ATM promotes the Mdm2 degradation d_{AM}. All other parameters were already introduced in the respective sections 1.3.2 and 1.4. The naming of the parameters follows these general conventions: parameters containing the letter "T" denote production rates concerning translation or transcription, parameters starting with a "d" denote degradation rates and parameters containing "k" are the respective Michaelis constants. The subscripts encode the affiliation to the modeled species, e.g. a "m" in the subscript is associated with the Mdm2 mRNA and a "M" with the respective protein species. Thus the parameter k_{Pm}, for example, describes the Michaelis constant of the Mdm2 mRNA production induced by the p53 protein. Rate parameters which do not follow this nomenclature are: A which gives the maximal activation rate of ATM, P which describes the dephosphorylation of ATM^* by $Wip1$, g which gives the maximal $Mdm2$ dependent degradation of $P53$ and finally C which is the maturation rate of new $P53$ entering the system. An overview of all model parameters and their values is given in the appendix A.2.

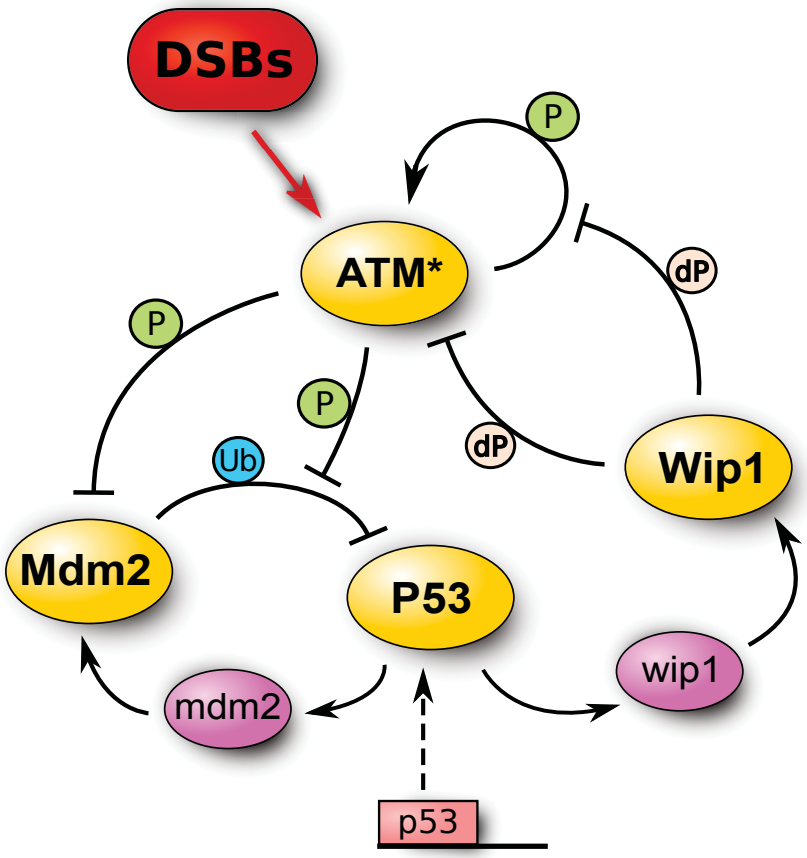

Figure 1.28.: Schematical overview of the modeled p53 interaction network in response to DSBs. A *P* at an interaction stands for phosphorylation, an *Ub* for ubiquitination and the *dP* marks dephosphorylations. The protein species involved are in yellow, magenta denotes mRNAs. The ATM kinase activation is triggered by DSBs, which enter the equation via the signal function $S(DSB)$ defined in the main text. Active ATM molecules facilitate the formation of further active ATM molecules via (auto-)phosphorylation events. These target the E3-ligase Mdm2 for phosphorylation which gets in turn destabilized by autoubiquitination and subsequent degradation. P53 gets constantly transcribed and translated, this steady influx is marked by the dashed arrow pointing from the p53 promoter. Because the antagonist Mdm2 got depleted, the P53 levels rise and the transcriptional activation of its targets Wip1 and Mdm2 is amplified. When the concentration of the matured phosphatase Wip1 increases, the direct dephosphorylation of ATM and especially the interference with the positive feedback leads to a decline of the active ATM concentration. Mdm2 gets in turn no longer suppressed and eventually brings p53 back to the steady state concentration. This completes one pulse cycle. If there are enough DSBs left a second pulse will evolve accordingly.

1.5.2. Bifurcation analysis and deterministic dynamics

The positive feedback introduced to capture the ATM-Wip1 switch dynamics has the potential to also cause bistability and excitability in the complete p53 network considered here. And indeed by choosing appropriate parameters, a regime with one stable rest state, a saddle point and an unstable fixed point can be found and is shown in figure 1.29. The value of the signal function $S \equiv S(DSB)$ was chosen as bifurcation parameter. As it should be for no DSBs present, i.e. $S = 0$, the system resides in an excitable class I regime characterized by one stable and two unstable fixed points.

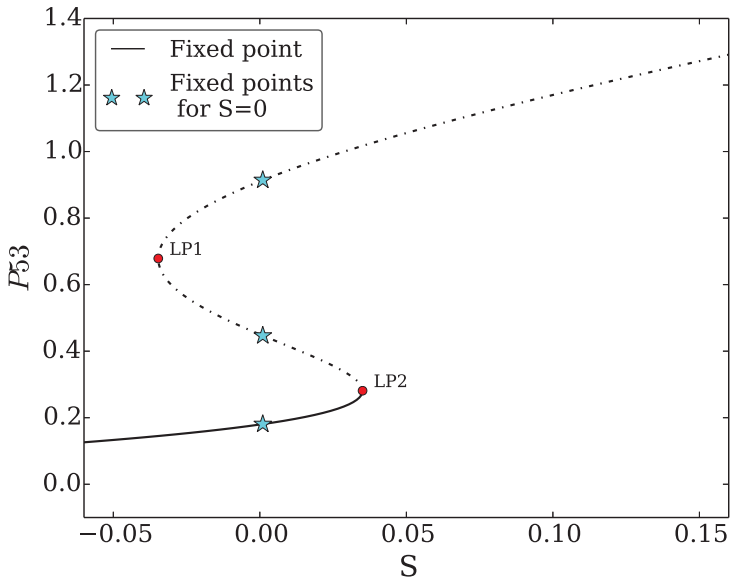

Figure 1.29.: Bifurcation diagram for the full model with the value of the signal function S to be the free parameter. The system has for $S = 0$ three fixed points, a stable rest state, a saddle point and an unstable fixed point. This fulfills the properties of an excitable class I system.

Before looking at the model dynamics, the bifurcation analysis shall be extended to other parameters and the region of excitability in the parameterspace shall be identified. It turns out, that apart for S there are only 4 types of bifurcation diagrams as depicted in figure 1.30.

The excitability class I regime is generally to be found when there are 3 fixed points present, two of them have to be unstable as depicted by the dashed curves. The size of this region is fairly large for all parameters shown in figure 1.30. The types I and II show symmetry in the sense of their asymptotic behavior. By that is meant, that for example transforming the fixed point curve F for the parameter C with $F_{tr}(C) = F(\frac{1}{C})$, the resulting diagram is qualitatively the same as the one for the parameter g in subfigure 1.30b. The types III and IV also show a symmetry with respect to a $F_{tr} = F(-C)$ transformation. An overview for all model parameters is given in table 1.3.

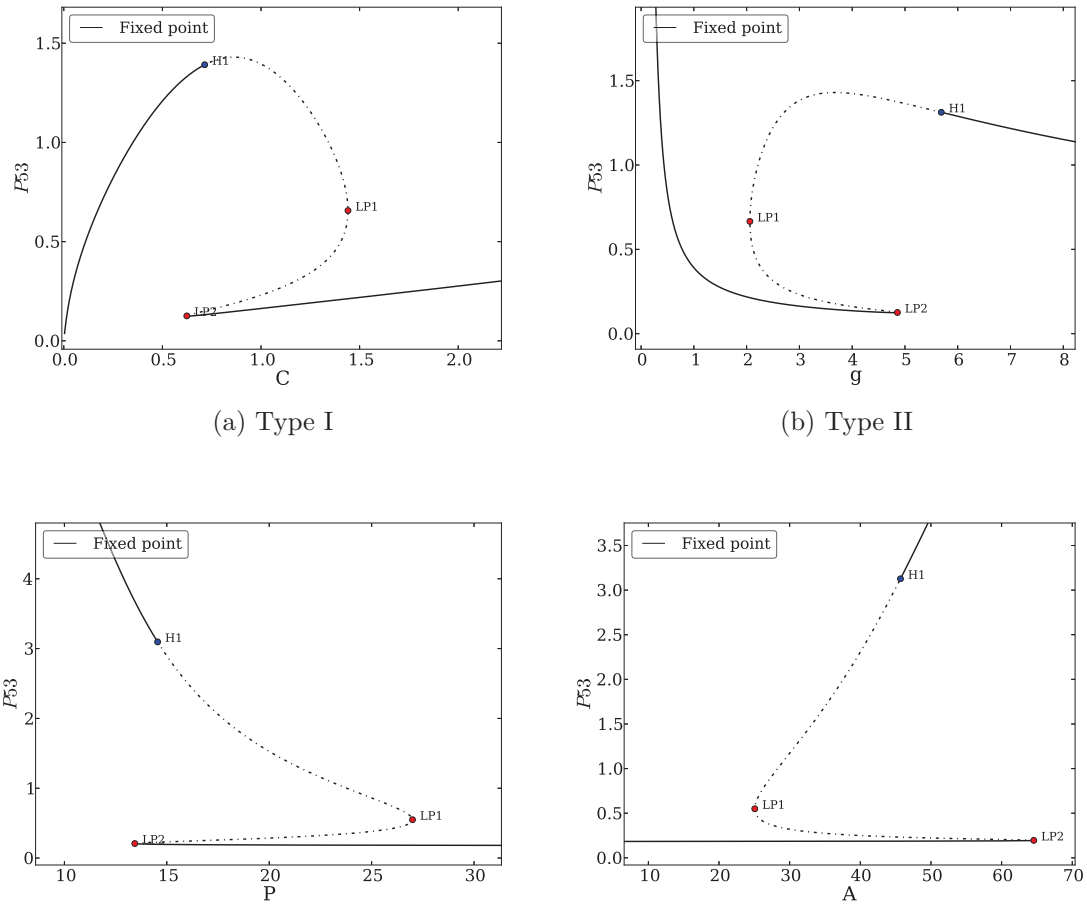

(a) Type I

(b) Type II

(c) Type III

(d) Type IV

Figure 1.30.: The four types of bifurcation diagrams obtained for the full model and exemplified by the parameters denoted on the x axes. The excitability class I regime is between the saddle-node bifurcation points *LP2* and *LP1*. If the Hopf point *HP1* lays in between the saddle node points, then there is a small region of bistability and the excitable regime ends there. The parameterized input signal is $S = 0.01$

Interestingly, there is a straightforward characterization for all types by noting the direct effect of their respective parameters on $P53$ or ATM^* . Types *I* and *II* contain all parameters controlling the P53-Mdm2 negative feedback loop, whereas types *III* and *IV* contain all parameters controlling the ATM-Wip1 switch. Although a nondimensionalization shall not be carried out for the model, mainly to preserve the biological meaning of the parameters, it can be assumed that parameters belonging to the same type would likely be condensed by it.

To further extend the bifurcation analysis, a search for codimension-2 bifurcations was performed as shown in figure 1.31. In accordance with the analysis of the FN model in section 1.3.3, a Cusp bifurcation point is found. This

Table 1.3.: Overview of the bifurcation diagram type membership for all model parameters

	type I	**type II**	**type III**	**type IV**
Parameters	C, d_m, d_M d_{AM}, k_{mp}	g, T_m, T_M R	P, T_w, T_W	A, d_w, d_W k_{WA}, k_{Pw}
Trait	positive on $P53$	negative on P53	negative on ATM^*	positive on ATM^*

marks the appearance of the phasespace structure required for the excitability class I regime. There is additionally a BT point, spawning a Hopf bifurcation curve which effectively destabilizes the upper fixed point and makes the system excitable. The specific bifurcation parameters are C and S here. However, there are actually only 2 symmetric types of these codimension-2 diagrams, the other type can be found in the appendix A.4. The region of excitability extends far into the halfplane for $S < 0$, but the signal should always be constraint to $S \geq 0$ so this is omitted in this plot.

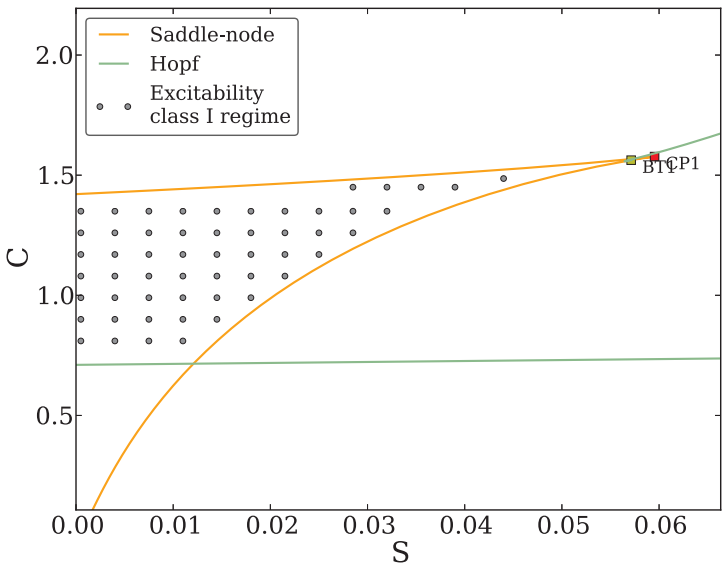

Figure 1.31.: Bifurcation set for the full p53 model, parameters are C and S. The excitability class I regime lays in between the two saddle node curves, this is the region were 3 fixed points co-exist. The destabiliziation of the 3rd fixed point occurs via a subcritical Hopf bifurcation, so that the region of excitability is additionally confined by the Hopf curve. This curve is spawned at the Bogdanov-Takens point *BT1*, which is very close to the Cusp point *CP1*.

For a wider picture of dynamical regimes present in the model, a bifurcation set with an extended parameter range is shown in figure 1.32. An oscillatory regime is nearby, this is a feature of excitable systems in general as discussed in section 1.3.3. But there are also bistable and monostable regimes. To obtain the bifurcation diagrams shown in figures 1.29 and 1.30, one just has to draw an imaginary horizontal or vertical line through the bifurcation set.

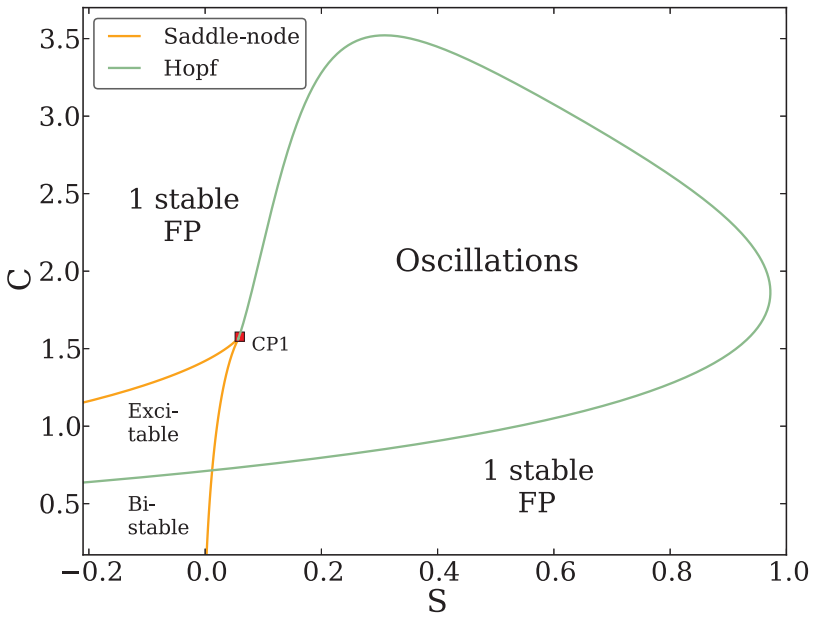

Figure 1.32.: Overview of dynamical regimes present in the p53 model. The p53 DNA damage response is modeled by exploiting the excitable and oscillatory regimes. The Bogdanov-Takens point spawning the Hopf curve is omitted for better visibility.

The bifurcation leading to the oscillations in the p53 model is the saddle-node homoclinic bifurcation [56]. This is a global bifurcation involving a local bifurcation. What happens at the bifurcation point is, that the heteroclinic connection of the saddle to the stable fixed point becomes a homoclinic orbit of the merged saddle-node. This saddle-node then disappears via the local saddle-node bifurcation and a limit cycle appears near the former homoclinic orbit. From within the excitable regime, which is considered as operating point of the model for no DSBs present, the oscillatory regime can only be reached by increasing the signal S. This is shown in figure 1.33, which is an extended version of figure 1.29.

The limit cycles of this positive feedback oscillator are born with huge amplitudes, and show only very little dependence on the signal strength up to $S \approx 0.5$. In effect, for no or low signal the system resides in an excitable state capable of showing isolated pulses. In addition, for a stronger signal after the saddle-node homoclinic bifurcation the system undergoes stable sustained oscillations. These

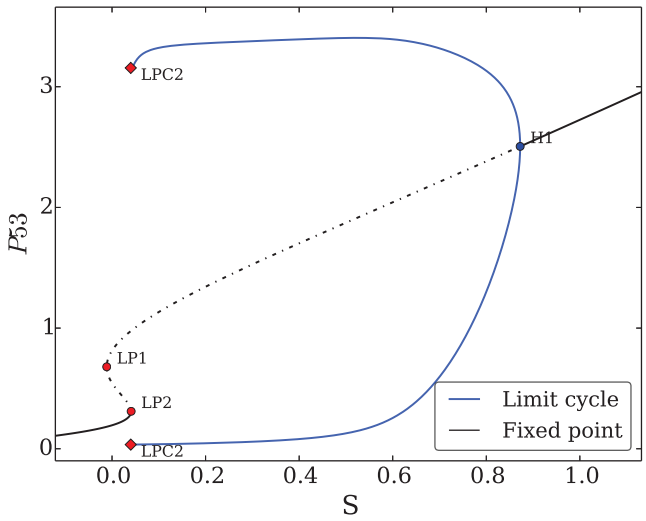

Figure 1.33.: Appearance of a stable limit cycle in the p53 model. The *LPC2* points mark the saddle-node homoclinic bifurcation. The amplitude of the oscillations is nearly constant up to $S \approx 0.5$. The production rate of p53 is set to $C = 1.4$.

are exactly the characteristics found in the p53 single cell data for low vs. high damage input, which were discussed in section 1.2. The actual functional form of $S \equiv S(DSBs(t))$ has to qualitatively reflect these dynamics depending on the number of DSBs present. This is discussed in the next section. For now what remains is to simulate some actual deterministic trajectories of the p53 model.

In figure 1.34 the system was first excited by a small initial pulse of ATM^* at $t = 0$, all other variables were initialized on steady state levels. Then after this excitation pulse the system settles down to the stable rest state. At $t = 15$ the signal is instantly set to $S = 0.4$. This moves the system in the limit cycle regime, and the oscillator is *switched on*. From the maximal stimulation an exponential decay of the signal takes place, and the system leaves the limit cycle regime at $t \approx 33$. This qualitatively resembles an experiment, in which the cells are damaged at $t = 15$. It is a feature of such positive feedback oscillators to finish the last cycle undamped. The reason for that is, that the orbit of the limit cycle smoothly transforms into the excitation loop at the homoclinic bifurcation point. It is noteworthy, that the last pulse is a bit delayed. This is an effect similar to that one briefly discussed in section 1.3.3, namely that the period of the oscillator tends to infinity close to the bifurcation point. However, in practice this region often is negligible small in parameter space, more details about that can be found in the appendix A.5. Finally, the oscillator has been *switched off* and after that the system remains silent as there is no further input. This undamped switching behavior is qualitatively very different in comparison to pure negative feedback oscillators. Their switching behavior was already studied in figure 1.16 of section 1.3.2 and it shows that damped pulses can generally not be avoided when moving in or out of the oscillatory regime in such

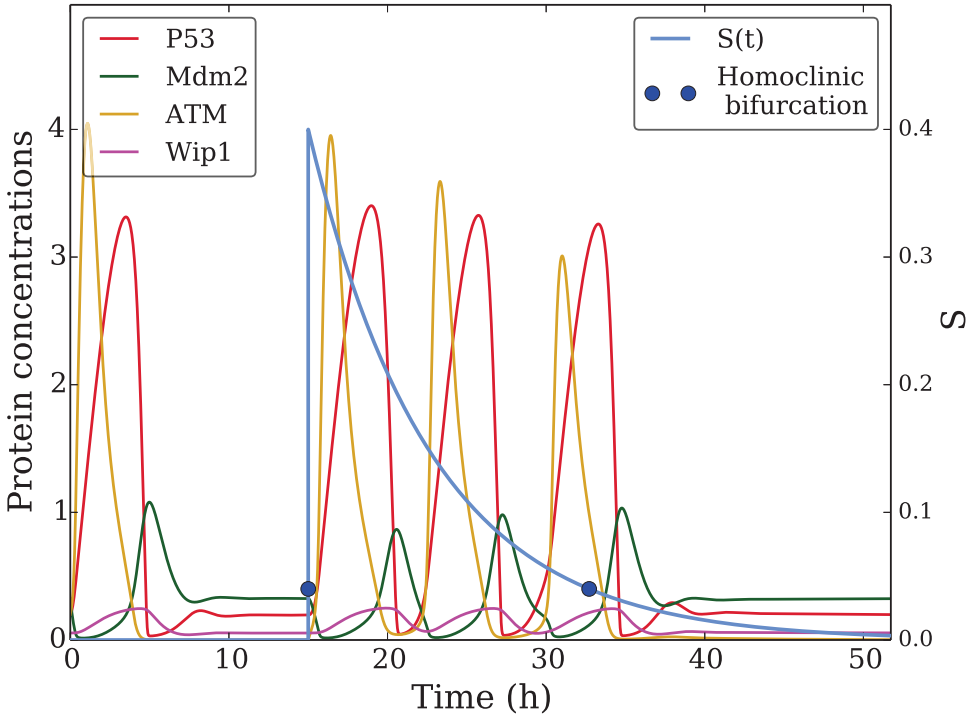

Figure 1.34.: Deterministic excitable and oscillatory dynamics of the p53 model. At $t = 0$ the system is initialized above the threshold and undergoes an excitation loop. At $t = 15$, after it settled down to the stable rest state, the signal is instantaneous set to $S = 0.4$. This switches the positive feedback oscillator *on*. The signal then exponentially decays and at $t \approx 33$ the oscillator is *switched off*. The system still undergoes a complete last cycle before returning to the rest state.

systems.

In summary the system shows a fairly large region of excitability in parameterspace. With increasing signal strength, the system becomes oscillatory via a saddle-node homoclinic bifurcation. Both regimes have been identified in the data in section 1.2, i.e. excitable dynamics for low or no external damage signal and oscillatory dynamics for the strong stimulated cells. For the latter scenario, the system responds in a digital fashion, i.e. with a discrete number of complete pulses. These oscillatory pulses are almost indistinguishable from the excitory ones, which is in agreement with the uniform pulse shapes found in the data. In the next section, the forcing of the system via an explicit time dependent signal $S(DSB(t))$ shall be studied with respect to a simple stochastic model for the DSB dynamics.

1.6. Driving the p53 model with a stochastic DSB process

1.6.1. Constructing a stochastic process for the DSB dynamics

The dynamics of the DSBs are considered as the primary input of the p53 model. Fortunately, as outlined in section 1.1, single cell trajectories of damage foci are available. While the direct relation between foci number and number of DSBs remains unclear, they can still serve as a quantitative marker [63]. Therefore, the number of foci is treated as the number of DSBs. Typically the DSB dynamics are described by an exponential model [51], which sufficiently describes the repair process. However, the half-lifes of the foci show large variability across a cell population [51, 63].

At first a pool of single cell foci trajectories is analyzed, the same raw data was already used for ref. [63]. Here the emphasis also lies on the amount of DSBs present after the repair of the inflicted damage has finished, this amount is referred to as background damage level. A modified exponential decay

$$DSB_{det}(t) = N_0 \; exp^{-\lambda t} + N_b, \tag{1.12}$$

is fitted to the data. The background damage level is captured by N_b, N_0 is the initial amount of DSBs and $1/\lambda$ is the decay rate. To capture the exponential repair process as well as the background level, a dataset with moderate damage of 5Gy and an observation time of 24h was chosen. Two examples are shown in figure 1.35.

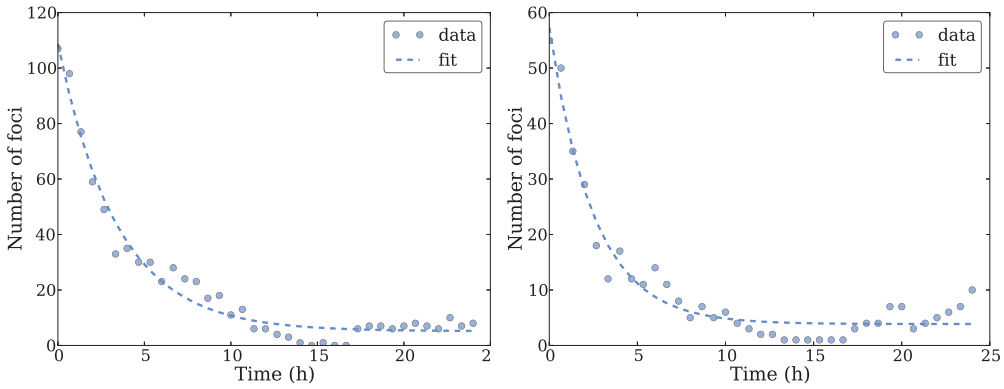

(a) $N_0 = 103.58, \lambda = 0.29, N_b = 5.15$

(b) $N_0 = 53.59, \lambda = 0.40, N_b = 3.86$

Figure 1.35.: Two representive single cell trajectories of the foci number for cells stimulated with 5Gy. The modified exponential fits are shown as dashed curves. The fitting parameters according to equation 1.12 are shown below. After an exponential decay of the foci, a mean background damage level, captured by the fitting parameter N_b, remains.

Repeating the fitting for the whole cell population yields a fitting parameter distribution shown in figure 1.36.

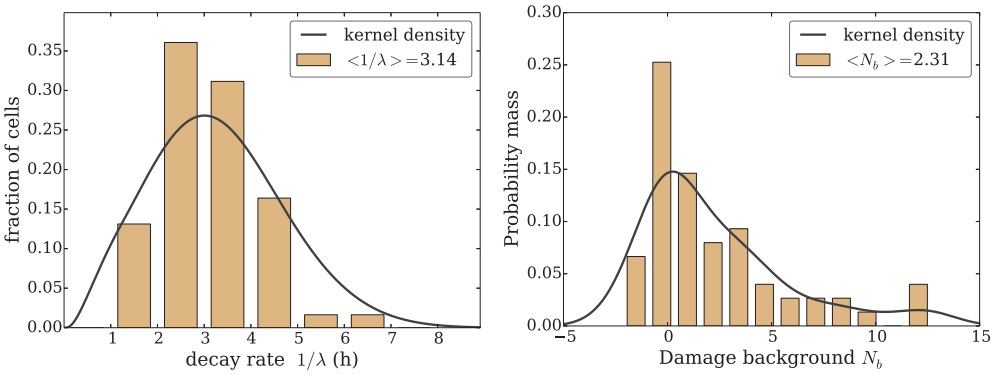

(a) Distribution of the inverse of the decay rate λ.

(b) Distribution of the damage background N_b.

Figure 1.36.: Fitting parameter distributions for the modified exponential model of equation 1.12 describing the foci dynamics. Cells were damaged with 5Gy and tracked for 24 hours in this data set. The mean fitting parameter values are shown in the legends.

As reported in the literature, a broad distribution of decay times ranging from 1-7 hours is found. This indicates a large cell-to-cell variability in the effective DSB repair times. The mean number of damage loci as captured by the modified exponential repair model is $\langle N_b \rangle \approx 2.3$.

However, in another data set where the number of foci in undamaged cells was recorded for 12 hours, the mean number of foci in the population is around $\langle N_b \rangle \approx 8.4$. The decay visible in figure 1.37 is due to photo bleaching effects. Given the unstressed conditions, the variability in the foci number within one trajectory over time could be calculated. Quantified by the variance (Var), also this quantity varies a lot between cells and ranges approximately from $7 < Var < 70$.

In summary, exact quantification of the DSB dynamics from experimental data remains a challenging task. What can be inferred from the raw data available is the following:

1. Upon damage induction, an exponential decay of the number of DSBs is observed. The decay rates show a large cell-to-cell variability,

2. After the repair of the induced damage is finished, there is a persistent number of DSBs present inside the cells also without stimulation,

3. The mean of this background damage is of the order $2 < \langle N_b \rangle < 10$,

4. This quantity significantly fluctuates over time

Given these characteristics, a stochastic process describing the DSB dynamics shall be constructed in the following. The sources of the observed stochasticity

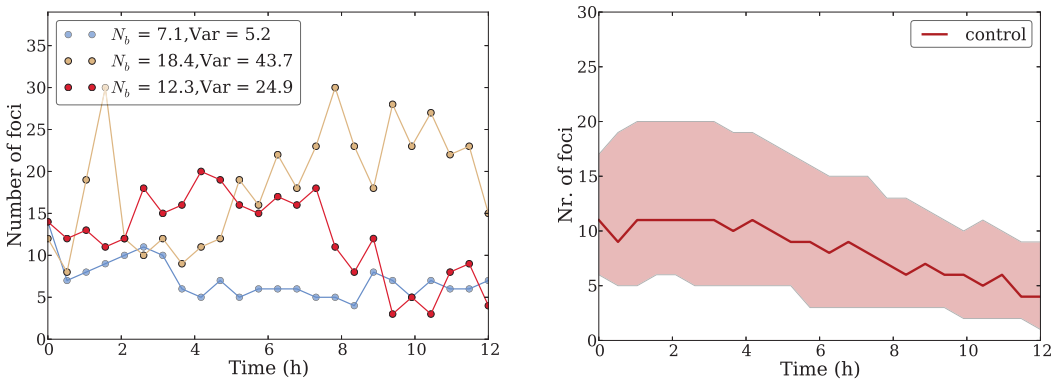

(a) Three exemplary single cell foci trajectories taken from a dataset of unstimulated cells. The number of foci variates significantly over time.

(b) Median and quartiles of the foci number for an unstimulated population of cells. The population mean for the background damage level is $\langle N_b \rangle \approx 8.4$

Figure 1.37.: Single cell foci dynamics and population dynamics of unstimulated cells.

of the DSB dynamics are both the processes which cause the DNA damage as well as the cellular repair mechanisms. The former include e.g. the errors arising from mitotic division, the occurrence of radical metabolic byproducts and cosmic radiation, which are intrinsically noisy. The latter appear to be irregular also due to various reasons, e.g. different severity of the DNA lesions or different copy numbers and spatial availability of the proteins involved in the repair process. As shown in figure 1.37a and as quantified by the variance, the trajectories show indeed a variability atypical for a deterministic process. The stochastic process describing the DSB dynamics should be of discrete state, as the number of DSBs is integer valued, and homogeneous in time for both computational and analytical tractability. A well studied and powerful theoretical framework providing these features concerns Markovian birth-death processes [37]. Under the rather weak assumption, that at a specific instant of time there is only either one DSB occurring or one is being repaired, it can be readily applied to model the DSB process.

At first, two rates b and r are defined by the following assignments of probabilities, given that there are n DSBs present at time t:

$$\begin{aligned} b\ dt &= probability\ that\ a\ new\ DSB\ occurs\ in\ [t, t+dt] \\ nr\ dt &= probability\ that\ a\ DSB\ is\ repaired\ in\ [t, t+dt]. \end{aligned} \tag{1.13}$$

The evolution of the DSB process $DSB(t)$ is now governed by the following

probabilities:

$$P(\,DSB(t+dt)=m|DSB(t)=n)\,=\begin{cases} bdt, & if\ m=n+1 \\ nrdt, & if\ m=n-1 \\ 1-(b+nr)dt, & if\ m=n \end{cases}. \tag{1.14}$$

Following to the reasoning of Gillespie in ref. [37] this process is called the *payroll process* and the quantity $(b+nr)dt$ describes the probability that the process will jump away from state n in the next infinitesimal time interval $[t, t+dt]$. Denoting the probability that the process will not leave that state in the time interval $[t, t+\tau]$ by $P_0(\tau)$ and the laws of probability give:

$$P_0(\tau+d\tau)=P_0(\tau)\ [1-(b+nr)d\tau], \tag{1.15}$$

which implies a differential equation with the solution

$$P_0(\tau)=e^{-(b+nr)\tau}. \tag{1.16}$$

Combining this result with the definitions in equation 1.13 and noting that unconditionally leaving a state at $\tau+d\tau$ and the landing at a new state $m=n+\nu$ are independent events yields the *next-jump density function* given by:

$$\rho_{DSB}(\,\tau,\nu|n,t)\,=\begin{cases} b\ e^{-(b+nr)\tau}, & if\ \nu=+1\ and\ n\geq 0 \\ nr\ e^{-(b+nr)\tau}, & if\ \nu=-1\ and\ n\geq 0 \\ 0, & otherwise \end{cases}. \tag{1.17}$$

This density can be fed into the Gillespie algorithm, and providing an initial condition, $DSB(0)=N_0$, Monte Carlo simulations of the stochastic DSB process can be readily computed. The stationary distribution of this process is the Poisson distribution given by the following density function:

$$\rho_s(n)=\frac{(b/r)^k\ e^{-b/r}}{n!} \tag{1.18}$$

The asymptotic analytical solutions for the mean and variance read:

$$\begin{aligned} \lim_{t\to\infty}\langle DSB(t)\rangle &= N_b=\frac{b}{r}, \quad and \\ \lim_{t\to\infty} Var(\,DSB(t))\,&=\frac{b}{r}. \end{aligned} \tag{1.19}$$

These relations only provide the ratio between the two rates b and r. To effectively reverse calculate the rates from the foci data, dynamical properties of the process have to be taken into account. The aim here is not to claim or provide an exact parameter estimation, but to give a reasonable estimation given the simplistic stochastic model used and the data available. In the following, the mean foci number N_b is used for the estimation, this already gives $b=N_b r$. The first moment time-evolution function for the payroll process given in ref.

[37] reads:

$$\begin{aligned}\langle DSB\rangle_t &= e^{-rt}\left(N_0 + \int_0^t be^{rt'}dt'\right)\\ &= \left(N_0 - \frac{b}{r}\right)e^{-rt} + \frac{b}{r}.\end{aligned} \tag{1.20}$$

Substituting with the asymptotic mean yields

$$\langle DSB\rangle_t = (N_0 - N_b)e^{-rt} + N_b. \tag{1.21}$$

The latter formulation remarkably resembles the modified exponential repair model introduced in equation 1.12. The notion of N_b and $\langle N_b\rangle$ might be a little confusing. For the stochastic process, these two are identical, N_b being the asymptotic time average of one realization and $\langle N_b\rangle$ being the asymptotic ensemble average. For the time series foci data, these two hardly coincide. Reasons for that are the finite and rather short period of sampling, some additional cell-to-cell variability and probably some systematic error in the measurements, as the number of foci is only a proxy for the number of DSBs. Nevertheless, to advance with the estimation, the l.h.s. of equation 1.21 is treated as an ensemble average at time t. Solving for the repair rate one obtains:

$$r = t^{-1}ln\left(\frac{N_0 - N_b}{\langle DSB\rangle_t - N_b}\right) \tag{1.22}$$

The time dependence of the rate is obviously artificial, as the rate should be time independent for a time homogeneous process. And indeed, when using this formula to reverse calculate the repair rate out of an ensemble of synthetic data, r is time independent for all $0 < t < t_c$. An example is shown in figure 1.38. However, when using equation 1.22, one carefully has to observe the denominator. From a critical time on, the ensemble average at time t_c gets very close to the asymptotic average: $\langle DSB\rangle_{t_c} \approx N_b$. This quickly leads to numerical precision issues, as the denominator converges exponentially fast to zero and might even turn negative due to fluctuations. This effect is clearly visible in figure 1.38b. Practically this means, that the estimation of the repair rate r should be carried out in a time domain, where the trajectories on average are still decaying. To improve the estimate, an averaging within the respective time domain $[0, t_c]$ can be carried out and will be done for the inference from the real data. It is noteworthy, that the relaxation dynamics are needed for the parameter estimation. An unstimulated ensemble of trajectories corresponding to stationary dynamics alone would not allow for the described method as this would correspond to $t_c = 0$.

Having demonstrated that the proposed method for rate parameter estimation works with synthetic data, now the real data shall be analyzed accordingly. Because every foci trajectory has generally a different N_0, the data is binned to form subensembles with comparable initial amount of DSBs. As can be seen in figure 1.39, the initial amount of DSBs present in the cells has a broad distribution despite the population received a fixed damage dose. This makes

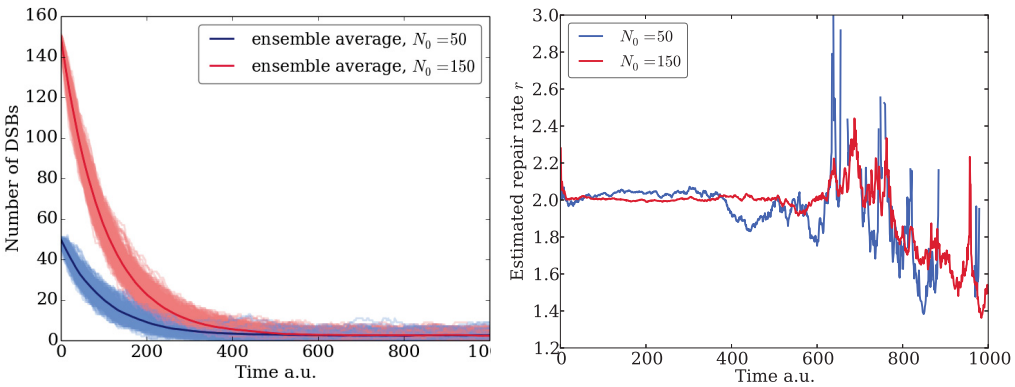

(a) Two ensembles and their ensemble averages of the stochastic DSB process. The estimation is based on 300 realisations for each starting value.

(b) Estimation of the parameter r using equation 1.22 of the main text and the observations shown in the left panel. The critical times upon numerical problems arise are approximately $t_c = 400$ and $t_c = 600$ respectively.

Figure 1.38.: Demonstration of the method for reverse calculating the repair rate given only observations of the stochastic DSB process. The synthetic data was computed using the Gillespie algorithm, parameters are $r = 2, b = 5$. By estimating the asymptotic mean and using equation 1.19 all parameters of the stochastic process can be inferred from observations.

the parameter estimation even more difficult, due to the low sample numbers in the subensembles.

As there are no principle problems in applying the method for the parameter estimation, the results for two different subensembles for the 5Gy data set are shown in figure 1.40. As expected, the results look rather poor as the chosen ensembles for the 5Gy set only contain 17 and 15 cells respectively. Given the broad initial distribution and that there are only 63 cells in total, there is no satisfactory pooling available. But nevertheless, the repair rate was estimated to be in the order of $r \approx 0.325$ per hour, which yields an average lifetime of a damage locus to be around 3 hours. Given the mean damage background level to be $\langle N_b \rangle \approx 2.3$, the corresponding spontaneous break rate for the DSB process is $b \approx 0.8$. Although a similar analysis for the 10Gy set gives comparable values for the repair rate, this data set is not considered as suitable for the estimation process. As most of the trajectories have not assumed a stationary dynamic, the estimation of the background damage level is too vague.

As stated earlier, this by no means constitutes a satisfying or exact parameter estimation. The author believes to have captured the right order of magnitude, as it is the same as the mean of the foci-lifetimes extracted from the data in ref. [63]. But the exact values may still differ substantially from this analysis. But

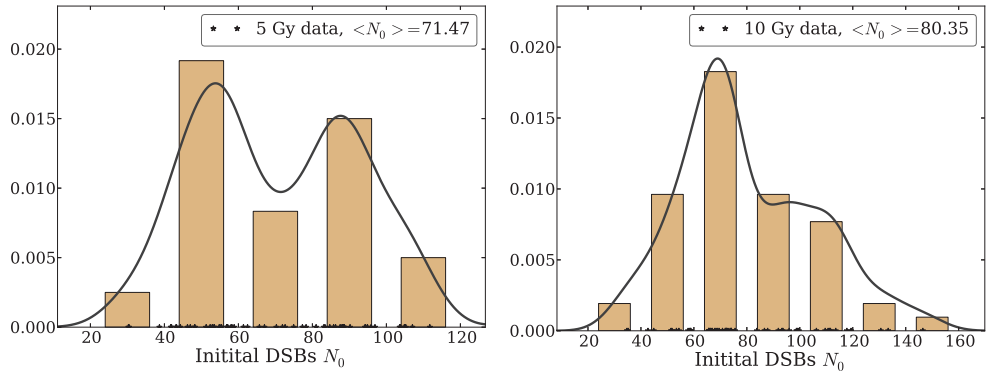

(a) Distribution of the initial amount of DSBs in the 5Gy dataset. The distribution appears to be bimodal.

(b) Distribution of the initial amount of DSBs in the 10Gy dataset.

Figure 1.39.: Initial DSB distributions for the 5Gy and 10Gy single cell foci trajectories.

instead of picking some rates by educated guessing, a method was found and applied to in principle reliably extract the needed information from the data, given the stochastic process defined above.

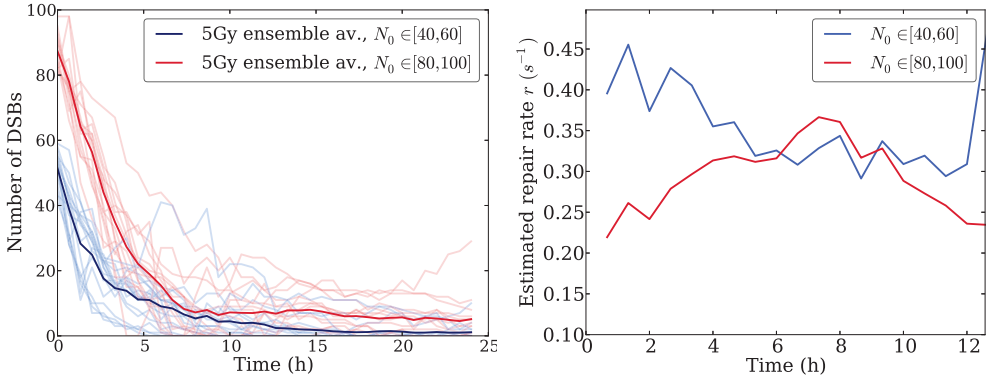

Figure 1.40.: Repair rate estimation for the 5Gy foci data set and based on the Markovian DSB model. The number of samples in the two ensembles considered is 17 and 15 respectively. This may explain at least in part the rather poor performance of the estimation performance. Nevertheless, the resulting value of $r \approx 0.35$ has a reasonable order of magnitude.

In summary, a Markovian birth-death process was formulated to model the DSB dynamics. A parameter estimation method based on relaxation dynamics of such processes was constructed, and successfully applied to synthetic data. It was further applied to the foci trajectories best suited for the estimation process,

and reasonable parameter values were obtained. In the following section this process shall be applied to the p53 model.

1.6.2. Stochastic forcing of the excitable p53 model

The general idea pursued here is, that a high number of DSBs translates into a high signal strength $S(DSB(t))$ which according to the bifurcation analysis in section 1.5 cause an oscillatory behavior of the model. As the parameters of the stochastic DSB process have been estimated in the preceding section and its exponential relaxation dynamics are in good accordance to the foci data, damaging the cells is simulated by simply starting the process away from its asymptotic mean with a $N_0 > N_b$. On the contrary, the spontaneous pulses observed in the data and treated as excitation loops in the model may captured by the stationary dynamics of the stochastic DSB process, independent of external stimulation. The fluctuations around the mean background damage may cause a spontaneous p53 pulse if the resulting signal $S(DSB(t))$ crosses the excitation threshold of the model. Hence, the specific functional form of S is crucial for the model performance. On the other hand, the exact molecular mechanism that triggers an initial amount of active ATM before the positive feedback kicks in is not known. In summary there remain the following two degrees of freedom: the threshold for the excitation loop can be adjusted by varying the parameters of the model and the function S can be chosen freely to cross this threshold for any DSB number desired. As the parameter set chosen in section 1.5 already qualitatively reflects p53 pulse properties like shape and lengths, what remains here is to make the signal function S explicit. The analysis is generally restricted to qualitatively show, that the model captures the p53 dynamics of both stimulated and unstimulated cells.

By forcing the system of ODEs with the DSB process it becomes non-autonomous, as it strictly already was in section 1.5. There, $S \equiv S(t)$ was made explicitly time dependent to illustrate the switching dynamics of the positive feedback oscillator. As the DSB process itself is stochastic, the p53 model becomes a hybrid stochastic-deterministic model. When simulating the system, it is convenient to precompute the DSB trajectory, as their is no feedback from the deterministic p53 model to this stochastic process. Upon the integration process, the precomputed realisation of the DSB process $DSB_r(t)$ can now be treated like a deterministic forcing function.

Before fixing the function $S(DSB(t))$, the 5Gy foci data set of the preceding section shall be reconsidered, this time also looking at the concomitantly recorded p53 dynamics. For that, the data is grouped in two mutually complementing sets. In the first set the data gets binned with respect to the initial damage received, measured by N_0. Then the distribution of pulse numbers is evaluated for the cell in each bin. And secondly the data is grouped according to the number of p53 pulses a single cell trajectory exhibited, and the ensemble average of the corresponding foci trajectories is plotted. The results are shown in figure 1.41, and clearly show, that cells with more initial damage and slower repair dynamics tend to have more pulses. This restates the results from the literature and also from the data analysis of section 1.2, but here the quantification is

more exact given the available foci data.

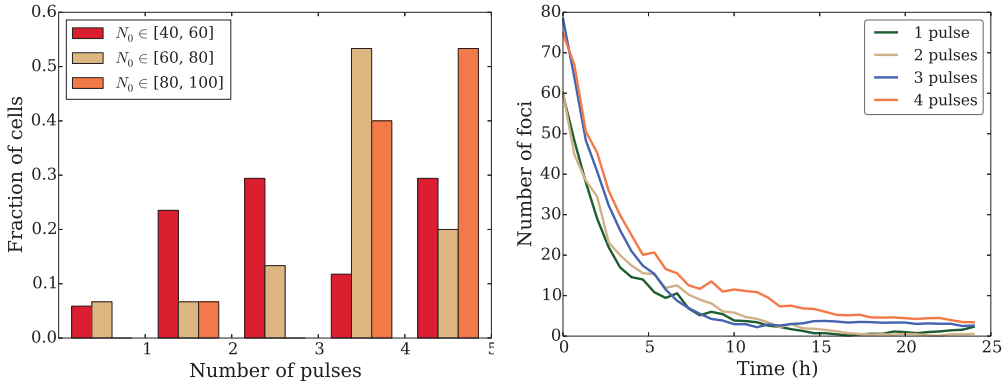

(a) Distribution of pulse numbers for the cells binned according to the initial amount of foci N_0. The higher the initial damage, the higher the average pulse number.

(b) Foci trajectory ensemble averages, grouped by the number of p53 pulses the cells exhibited. The difference between one and two, and three and four pulses, is on average more influenced by the repair kinetics than by the initial damage received.

Figure 1.41.: Relation between foci trajectories and p53 pulsing for the 5Gy data set.

The signal function $S(DSB(t))$ could be of many forms, and there is no *a priori* precedence for one or the other. For simplicity a scaled logarithm was chosen :

$$S(\,DSB(t)) \;= \gamma \; ln(\,DSB(t) + 1)\,. \tag{1.23}$$

The single parameter γ controls the sensitivity of the signal towards DSBs and is therefore very essential for the model performance. For example, setting γ to high would not allow for the excitable regime even for stationary DSB dynamics as the resulting value $S(N_b)$ would already set the system in the limit cycle regime. Given the mean number of pulses to be around one per 12 hours for the dataset analyzed in section 1.2, the sensitivity parameter was adjusted to $\gamma = 0.06$. The estimated rate parameters for the stochastic DSB process are fixed to $b = 0.8$ and $r = 0.3$, all what is needed to simulate a trajectory is to specify an initial amount of damage N_0. Some exemplary realisations are plotted in figure 1.42.

By simulating pools of trajectories, model output statistics for different initial conditions can be obtained. This facilitates the assessment if the model semi-quantitatively captures the measured data. In figure 1.43 the IPI distributions and the pulse number distributions for simulated and measured data are shown. The IPI distributions are, as discussed in section 1.2.1, a suitable measure, to demonstrate that the model depending on the initial damage exhibits both regular oscillatory behavior and irregular excitable behavior. This corresponds

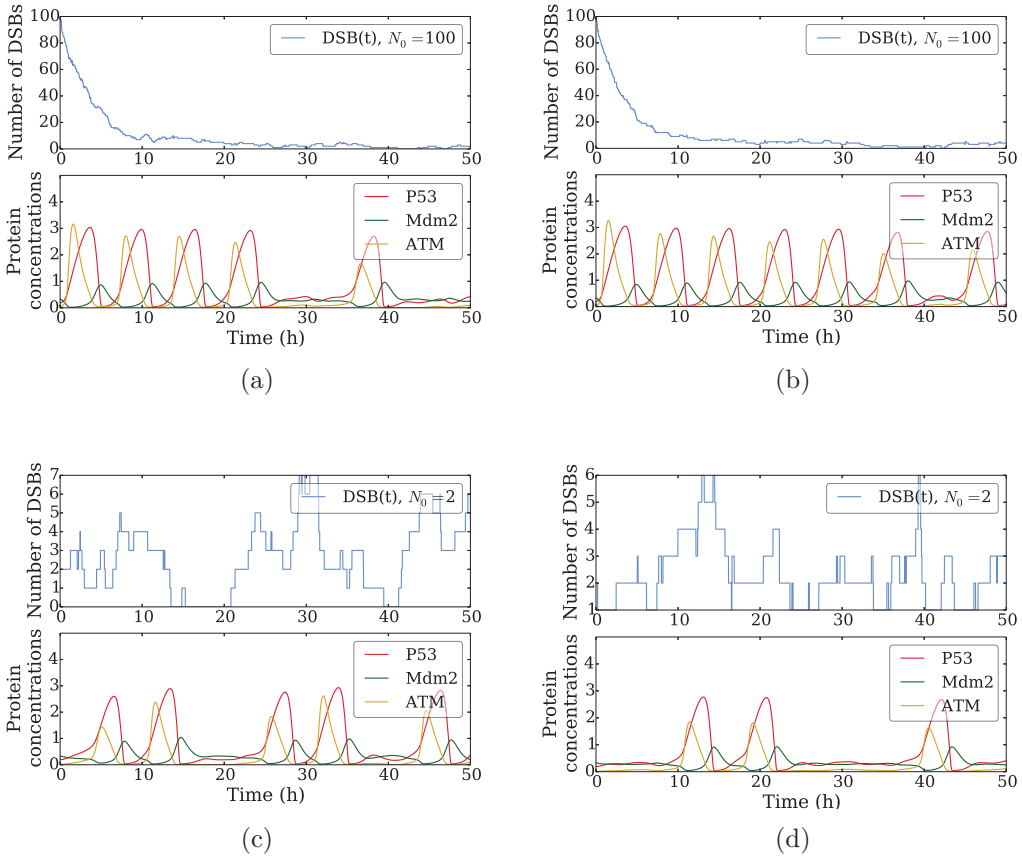

Figure 1.42.: Four exemplary p53 model trajectories. In figures (a) and (b) the initial amount of DSBs was set to $N_0 = 100$ which corresponds to a high damage scenario. Figures (c) and (d) show two trajectories initialized with $N_0 = 2$. These dynamics correspond to unstimulated cells.

to the strong and weak stimulated cells in the data respectively. The pulse number distributions illustrate the high variability in the total pulse number in between single cells for an equal amount of initial DSBs. In the model, the only source for this variability is the stochastic DSB process but it is sufficient to generate a heterogeneity similar to that found in the data. However, as shown in the preceding subsection, the broad distribution of damage loci given a fixed stimulation strength additionally amplifies the heterogeneity in the data. Another limiting factor for the congruence between simulations and real data is measurement noise, which is not assessed at all by the model. Recording fluorescence signals from living cells introduces many sources of variability in the signal, even when the tagged protein levels are constant. The measured pulses therefore show some irregularities, whereas the simulated pulses are always of equal shape. This effects, that the IPI distributions of the data are broadened even for the most regular pulsing cells similar to the effects observed for the noisy limit cycle oscillator analyzed in section 1.2.1.

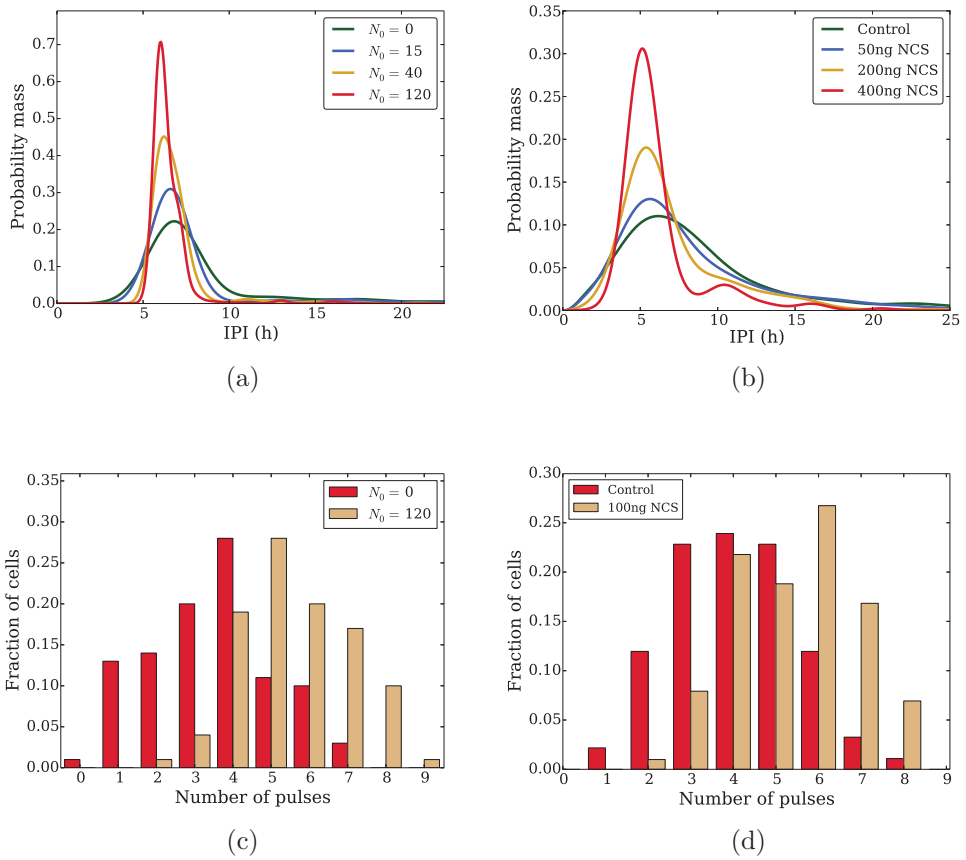

Figure 1.43.: Model output statistics (left) compared to the results from the data analysis (right). In figure (a) and (b) the IPI distributions are shown. Figures (c) and (d) show the pulse number distribution. For the simulated data, the initial amount of damage was fixed according to the legend. Whereas in the measured data, a fixed dose of the damaging agent NCS was added. Both simulated quantities are in good agreement with the data.

In this section the p53 model for the response to DSBs is finally complete. The signaling function was heuristically chosen in a way, that only one additional parameter controls its sensitivity towards the amount of damage. Taking the basal p53 activity as a benchmark, this parameter was fixed and model output statistics were generated. These showed good agreement with the data according to the IPI and pulse statistics. In the last section, the predictive power of this model shall be assessed.

1.7. Reanalysis of inhibitor experiments

The kinase inhibitor Wortmannin (Wm) was used in previous works [7, 62] to study the effects of transient activation of the p53 network. Wortmannin is a broad-range kinase inhibitor effectively abrogating the activities of many kinases, notably the upstream kinases ATM and DNA-PK. In these studies, Wm was added shortly after the cells were damaged and single cell pulse analysis was performed. The authors found a reduced number of pulsing cells dependent on the time point of Wm addition and stated an all-or-none response with respect to amplitude and widths of the p53 pulses. Consequentially it were these studies, which first introduced the concept of excitability to explain the p53 dynamics in response to DSBs.

However, by disabling ATM the p53 network considered here it the model looses its only positive feedback. The theoretical considerations undertaken in section 1.3 therefore render an excitable behavior of the model downstream of ATM as impossible, given that there is no other positive feedback on p53. Moreover, simulations show a graded dependence of pulse amplitude and width on the time point of Wm addition, results are shown in figure 1.44. By lowering the amount of active ATM within a pulse formation process, Mdm2 levels can recover sooner and P53 is set back to the steady state concentration before a full pulse can evolve. To address the question if the model maybe still lacks a prominent feedback mechanism, the raw data used in ref. [62] shall be reanalysed. In these experiments, the cells were damaged with a high dosage of NCS and subsequently imaged for six hours. Wm was added at different time points for each condition and thereafter refreshed to continuously inactivate the upstream kinases.

An important part of pulse detection for the p53 data involves a threshold for the minimum amplitude a pulse should have to be identified as such. Also the wavelet based method used for the analysis here can be deluded by some random fluorescence signal variations. The fraction of responding cells, the are ones who show a pulse, as a function of the amplitude threshold is shown in figure 1.45. As expected the number of detected pulses decreases with increasing amplitude threshold. The question about the *right* threshold is hard to answer exactly. Therefore the subsequent analysis will be done for three representative threshold values. In the results of ref. [62] a response rate of around 0.6 is reported for the control condition. This suggests, that a very high threshold was chosen in their analysis.

To make the effects of Wm on the pulse amplitudes for different thresholds and also to the results of the model comparable, the pulse amplitude of the control condition is set to one. With this, the amplitudes of the conditions with inhibitor addition are given as the ratio of the amplitude of the unperturbed p53 system. In figure 1.46 the results of the data analysis for three different thresholds and the model output are shown. The earlier the inhibitor is added the lower are the p53 pulse amplitudes to be observed. This effect gets smaller with higher thresholds for the pulse detection, as this effectively filters out the smaller pulses. In this sense, with higher thresholds the analysis here converges to the results of ref. [62]. As already seen in figure 1.44 the model qualitatively shows exactly

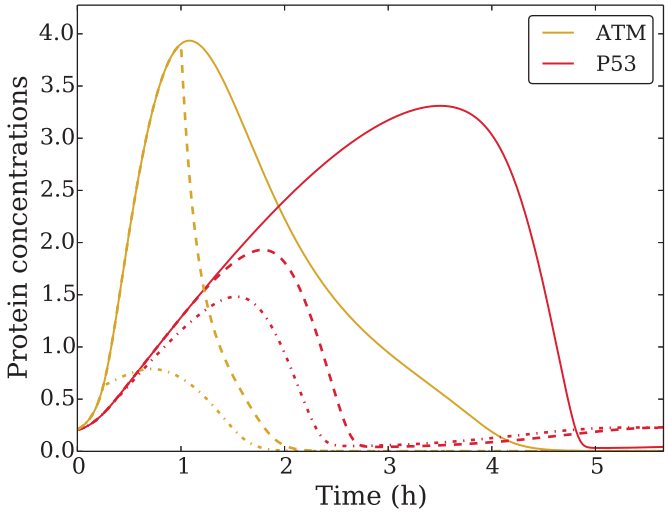

Figure 1.44.: Deterministic simulations of the inhibitor experiments. Dashed lines correspond to Wortmannin addition after 60 minutes, point-dashed lines after 15 minutes, of stimulation. The system was started above the excitation threshold. Upon the indicated time points, a strong degradation term mimicking the effects of Wm was switched on in the r.h.s. of the ATM equation of the p53 model. The model predicts lower pulse amplitudes and smaller widths compared to the control condition.

this behavior, although the effect is more pronounced. Reasons for that might be that there are some intermediate and redundant kinase species acting on the P53-Mdm2 core negative feedback which are not covered by this minimal p53 model. These may longer suppress the P53 antagonist Mdm2 and therefore buffer the sudden absence of active ATM in time, effectively adding inertness to the systems dynamics. Additionally, the kinetics of the kinase inhibition by Wm are unknown. In the model, as can be seen in figure 1.44, its inhibiting action kicks in instantly after addition. Lowering this rate of inhibition would trivially lead to bigger p53 pulses in the model. The same analysis for the pulse widths yields comparable results. However, given the low time resolution in this data set of only 25 time points for the whole observational period, this analysis has more uncertainties and is therefore omitted here, As a last remark it should be stated here, that the analysis was supported by visual inspection of single trajectories to double check that detected low amplitude pulses are indeed present in the data and not artefacts of the detection algorithm.

The observation of figure 1.45, that the addition of the kinase inhibitor Wm lowers the response rate of a stimulated cell population in a time dependent manner is not captured by the model simulations. This can be understood by noting, that the timing of the first pulse is very heterogeneous within a cell population. This is shown in figure 1.47, where the distribution of the peak times is shown. It is striking that the timing of the detected pulses is shifted

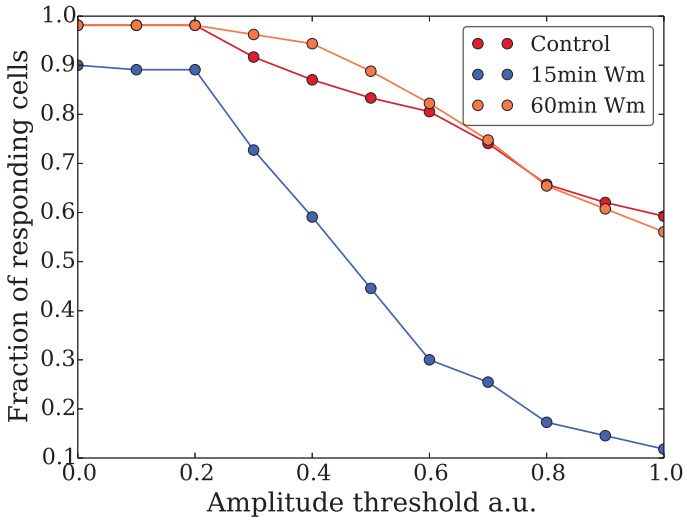

Figure 1.45.: The fraction of cells to be identified as responding as a function of the amplitude threshold used for the pulse detection. The addition of the inhibitor Wm generally decreases the number of cells showing a pulse. The earlier Wm is added, the more cells show no p53 pulse at all. A comparison to the results reported in ref. [62] show, that a very high threshold was used in their analysis.

towards earlier time points the earlier Wm is added. It is evident that the initiations of the individual pulse formations shift accordingly. But this means that compared to the control condition, the potentially later forming pulses are much stronger inhibited or completely abrogated by the kinase inhibitor. These are surely contributing to the lower response rates. As the cell state is modeled completely homogeneous there is no cell-to-cell variability present in the model to account for the observed different pulse timings. This explains at least in part that the lower population response rates upon Wm addition can not be captured by simulations so far.

In this section the predictions of the model led to a careful reanalysis of published data. In accordance with the simulations, the inhibitor Wm indeed has an influence on the pulse amplitude. This is a strong check for model consistency. If the reanalysis would not have shown such effects, the assumed underlying regulatory network would have been rendered incomplete, as this would be a strong evidence for another upstream kinase independent positive feedback present in the system to predominantly account for the excitability. Therefore, these results assure, that the positive feedback employed in the model is indeed important for the excitable pulse formation.

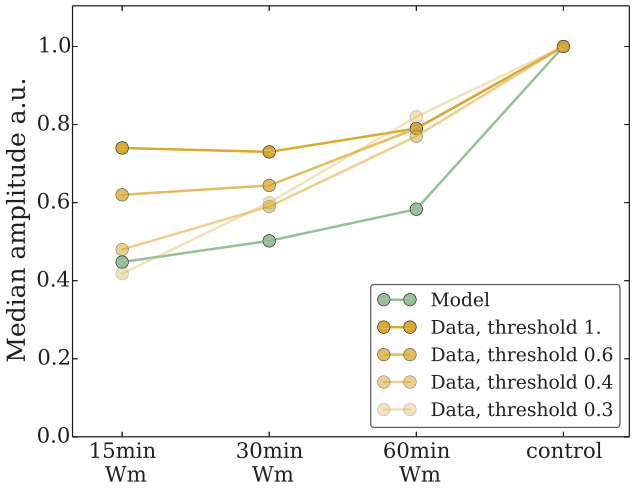

Figure 1.46.: Comparison of median amplitudes extracted from the data for different time points of Wm addition with model predictions for different detection thresholds. The earlier the inhibitor Wm is added, the lower are the resulting p53 pulses. This effect gets smaller with higher thresholds. The model qualitatively reflects this behavior, although the effect of the inhibitor is more pronounced in the simulations.

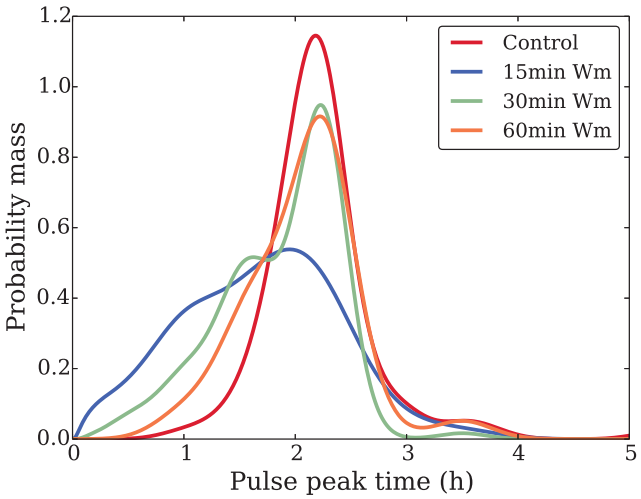

Figure 1.47.: Distribution of the p53 pulse peak timing for strongly stimulated cells. The kinase inhibitor Wm is added as indicated in the legend. The earlier it is added, the more of the detected pulse peak times are shifted towards earlier time points. Cells in which the pulse formation started later will not develop a pulse depending on the time point of Wm addition. This explains at least in part the lower response rates observed in figure 1.45.

1.8. Discussing the p53 modeling approach

Every approach to quantitatively describe cellular processes faces the immense complexity of the molecular interactions constituting a specific cellular function. This is still puzzling for both the theoretical as well as the experimental biologist. It is therefore of utmost importance to define and confine the biological problem as much as possible to keep the complexity as low as possible. One can argue that especially for p53 this idea is doomed to fail, as the number of feedbacks involved with p53 are of the order 100 [14]. Even when only considering the specific regulation of p53 in response to DSBs, the amount of potentially important interactions is still hard to anticipate [64].

It was therefore very advantageous for the model construction that experimental findings, especially the ones documented in refs. [7, 62, 87, 96], provided strong clues, that the four protein species $P53$, $Mdm2$, $Wip1$ and ATM are the key players for orchestrating the signalling cascade in response to DSBs. Incorporating the respective mRNA species which are actively regulated during that response, a p53 model consisting of only six species could be developed which semi-quantitatively captures the observed p53 dynamics for both stimulated and unstimulated cells. In contrast to most published models also the basal dynamics which are characterized by isolated pulses can be reproduced. The model also shows a *digital response* (see figure 1.34 in section 1.5.2) after damage induction, reported already for the first single cell studies in ref. [57]. The theoretical concept which allows for that complex model behavior is excitability, which is a well studied subject of dynamical systems theory. A detailed introduction to excitability based on the famous FitzHugh-Nagumo model was developed in section 1.3.3. Applying this theory to molecular interaction networks lead to the insight, that only systems comprised of at least one positive feedback can exhibit an excitable regime. Models prior to this work either did not incorporate a positive feedback at all [6, 35, 65], or relied on positive feedbacks which lack a strong experimental evidence [15, 97]. Besides, the concept of excitability was still not explicitly exploited by the latter. A careful scan of potential positive feedbacks was done in close collaboration with the Loewer lab which also provided transcriptome analysis of some promising candidates, e.g. Caspase-2 [75]. This lead to the conclusion, that the positive feedback is most likely to be found in the upstream kinases, most notably ATM. The reported switch like activation of ATM, as it is very sensitive towards low numbers of DSBs, made it a prominent candidate. However, its specific interactions with other kinases like DNA-Pks, the MRN repair complex or the phosphorylated histone variant γH2AX leading to the positive feedback remain elusive. Further experimental studies are very eligible here. In the end only a phenomenological self activation term for the ATM activation was added to the model, which is presumably an oversimplification. Incorporating the phosphatase Wip1 which effectively destabilizes active ATM and interferes with the positive feedback was sufficient to introduce excitability into system (see section 1.4).

The model construction was generally supported by extensive single cell raw data analysis (section 1.2). To reliably detect and characterize the p53 pulses a novel peak detection algorithm was developed (see Appendix A.1). It

exploits the favorable properties of wavelet analysis of noisy data. In short, by smoothing the data on many scales the typical data analysis problem of over- or under-smoothing is circumvented. The distribution of inter pulse intervals was found to reliably identify dynamical regimes which deviate from noisy limit cycle oscillators. Applying this tools to measured p53 trajectories lead to the conclusion that both oscillatory and excitable regimes are present in the data. The former are most prominent in strong stimulated cells whereas the latter are found in weak or unstimulated cells. Even for a fixed and high amount of damage, the pulsatile responses are very heterogeneous with respect to the number of pulses on a single cell level.

This observed heterogeneity could be further assessed by analysing single cell damage foci trajectories. Similar to the results of ref. [63], a high cell-to-cell variability of the DSB repair kinetics has been observed. However, special attention has been given here to the background damage levels. These fluctuating DSB dynamics after repair or without stimulation at all serve as the input for the basal p53 dynamics. A simple yet plausible stochastic process for the DSB dynamics was proposed to be a Markovian birth and death process (section 1.6.1). It captures the two essential events, repair of a single DSB and occurrence of a new DSB, with two rates. Despite the quantitative uncertainties in the experimental assessment and discrepancies between different data sets, reasonable values for the rates of the stochastic DSB process could be estimated from the data. A promising extension of the stochastic process devised here, would be to make the rates time dependent. By varying the repair rate, different repair processes dominant in different cell cycle phases as reported in ref. [51] could be captured. A time dependent break rate could directly reflect the increase of breaks naturally occurring during DNA replication in the S phase of the cell cycle. However, these alterations would make the stochastic process non-homogeneous in time which is beyond the scope of this work. The conversion of the number of DSBs present and their effective signal strength $S(DSB(t))$ for the excitable p53 model has been achieved by an ad hoc one parametric logarithmic transformation.

The proximity of an oscillatory regime in parameter space is a hallmark of every excitable regime. This is naturally exploited in the model, as it is the signal strength which determines the transition between these two regimes (see section 1.5.2). Therefore the number of DSBs determines weather p53 oscillates or shows isolated infrequent pulses. The time an individual cell spends in the oscillatory regime is given by the stochastic repair dynamics incorporated in the Markovian DSB process. Therefore the same amount of initial damage can lead to different pulse number responses as observed for the measured p53 trajectories (section 1.6.2).

Despite the simplifications and assumptions made during model construction, it proved to improve the mechanistic understanding of the p53 signaling modul. Simulations but also just theoretical reasoning pointed to the existence of smaller and partial p53 pulses upon ATM inhibition some time after stimulation. Driven by the model predictions, published p53 trajectories obtained from inhibitor experiments were carefully reanalyzed and such lower amplitude pulses were indeed discovered (section 1.7). Thus, data analysis and modelling suggest that

there is no excitability, e.g. *all or none responses*, downstream of the kinase network targeted by the kinase inhibitor Wortmannin. This hypothesis could be tested experimentally in future studies.

Having all sources of cell-to-cell variability reside in the stochastic DSB dynamics is most likely the major limitation of the model. It is well known that protein abundances as well as responsiveness to uniform stimuli differ widely between cells in a clonal population [95]. One major source of this variability is stochastic gene expression [29]. Fluctuations around the steady state protein levels are especially functionally important for low abundances. However, studies like the one in ref. [85] showed that the key players considered here, namely p53, Mdm2, Wip1 and ATM, are all highly abundant in mammalian cells. This, and also the observation of rather smooth and regular p53 pulses, greatly reduces the possible impact of stochastic gene expression on the p53 system. This should not be that surprising, given the crucial role p53 plays in securing the genomic integrity and cell cycle progression. A fact which might play an important role is that also the levels of highly abundant proteins are variable within a cell population and they can have long, i.e. several cell cycles, mixing times [88]. On the contrary, the steady state concentrations and also all the production and degradation rates are the same for all "cells" described by the model. Another potential source of variability in cell responses given the same number of DSBs is the spatial distribution of the damage loci. The exact processes triggering the fast and global ATM activation are not well understood so far. If nucleation processes play an important role, the location of the damage loci and the spatial availability of damage sensors and other mediators may be important. In summary, for the present model a fixed trajectory of DSBs, deterministically translated into the signal strength $S(t)$, will trigger identical system responses for all simulated cells. This is needless to say not observed in experiments [63]. Including a meaningful cell-to-cell variability in the model downstream of the DSB process is a challenging task for the future. It will ultimately effect the excitation threshold and could thereby explain the observed variability in responsiveness.

An interesting finding which might be of more general significance concerns the switching behavior of biological limit cycle oscillators. Oscillatory dynamics are reported for a broad range of cellular processes including metabolism, signaling, locomotion or cell division. For many of these oscillatory processes it can be expected that the oscillations are not running forever, but instead that they are a well regulated response towards a changing environment. For example oscillatory signaling might be initiated or terminated by extracellular stimuli, or metabolic oscillations might depend on the available nutrients. By observing the onset or the termination of such oscillations, results from dynamical systems theory allow for a qualitative inference of the regulatory network which accounts for these oscillations. The route to limit cycle oscillations for a negative feedback system always implies strong damping in amplitude during the switching between an oscillatory regime and a steady state. On the contrary, for a positive feedback oscillator the oscillations are generally born with huge amplitudes. The reason for that distinct qualitative behavior is the type of bifurcation leading to the oscillations. For negative feedback oscillators this is the supercritical Hopf

bifurcation, which directly yields stable oscillations of arbitrary small amplitudes. In the case of the positive feedback system the route to oscillations is more complicated. A subcritical Hopf bifurcation with a subsequent bifurcation of limit cycles is one way to reach stable oscillations. Another possibility is the saddle-node homoclinic bifurcation, where the saddle collides with a stable limit cycle. Excitability class I regimes are most likely to be found in the proximity of such bifurcations. Also, strictly speaking, positive feedbacks are only necessary for these type of oscillators, they do not guarantee such complex bifurcation structure. However, reversing this argument implies that pure negative feedback systems are incapable of excitable dynamics and switch oscillations *on* and *off* always with varying amplitudes. This was the main argument for the conclusion that the known feedbacks of p53 involving Mdm2, Wip1 and ATM are insufficient to explain the systems behavior. It should be noted, that when omitting the switching behavior and no isolated pulses are observed, the popular negative feedback oscillator models certainly match the observations of sustained oscillations and are comparatively simple to employ. The future prospective would be to survey other cellular oscillators and check their established regulatory network for consistency in this regard, e.g. the transforming growth factor β might be a promising candidate [2, 110].

2. Hierarchic stochastic modelling of intracellular Ca^{2+}

So far, an intracellular signaling system focused on p53 was modeled by an underlying deterministic dynamical system exhibiting regular limit cycle behavior and irregular excitable behavior driven by noisy DSB dynamics. The observed pulsatile dynamics indicated a regulatory network comprised of at least one strong positive feedback, which precise molecular basis still has to be found. In the second chapter of this work another important intracellular signaling system, focused on the messenger molecule Ca^{2+} , shall be investigated. Interestingly, it also exhibits irregular pulsatile, although more spiky, dynamics. However, the positive feedback allowing for such sharp excitable dynamics is well known in the case of Ca^{2+} signaling. It is termed calcium induced calcium release (CICR) mechanism and will be explained in the following introductory section. Because the Ca^{2+} spikes themselves are very short compared to a typical inter spike interval, the system can be modeled adequately by focusing on the stochastic spike occurrence times. In contrast, for p53 the IPIs were of the same order of magnitude as the p53 pulse width. Additionally, the recorded single cell Ca^{2+} trajectories generally show a very high degree of variability. Therefore all mechanistic processes are captured by probabilities and the Ca^{2+} signaling model to be discussed is completely stochastic.

The results and findings presented here are based on recently published work [72, 105] by the Falcke group. Experimental results shown were done by co-authors Kevin Thurley from the Falcke group and Stephen C. Tovey and Abha Meena from the Colin W. Taylor lab at the University of Cambridge.

2.1. Introduction to intracellular Ca^{2+} signaling

Ca^{2+} is a ubiquitous intracellular messenger transmitting information by repetitive cytosolic concentration spikes. It is involved in key cellular functions like proliferation, metabolism and apoptosis, as well as in cell type specific functions like muscle contraction or insulin secretion [9, 30]. The intracellular Ca^{2+} dynamics can be captured by life cell imaging using fluorescent calcium sensitive dyes [9, 30]. A typical outcome of such an experiment are single cell Ca^{2+} spike trains, a few examples are shown in figure 2.1. The main descriptor of these spike trains is the interspike interval (ISI) distribution. The ISI was originally defined in the exact same way as the IPI is defined in the case of p53 signals discussed in the first part of this work. It is simply the time period between two consecutive Ca^{2+} spikes. It has been demonstrated by analysis of the ISI distribution that these Ca^{2+} signals are repetitive stochastic events [26, 90]. The main argument here is, that the average ISI (T_{av}) is of the same order of

magnitude as its standard deviation σ. Moreover, a large cell-to-cell variability of T_{av} is observed. Strikingly, the relationship between T_{av} and σ is linear, and its slope is a robust cell type specific property [90, 103].

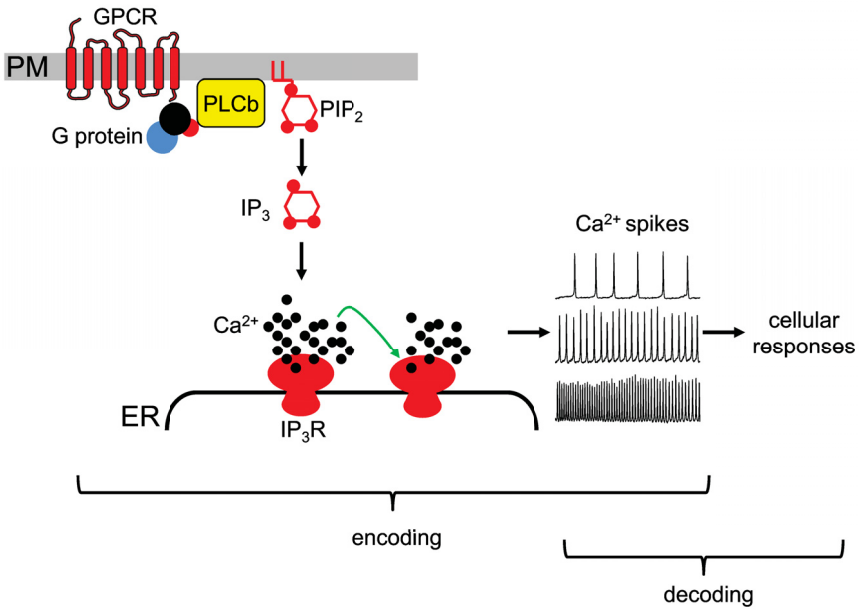

Figure 2.1.: Schematic overview of the Ca^{2+} release mechanism, a detailed description can be found in the main text. Additionally three exemplary Ca^{2+} spike trains are shown. Analysis of the interspike interval distribution revealed the stochasticity of these intracellular Ca^{2+} signals. Figure taken from ref. [105]

An important class of Ca^{2+} signals is mediated by Inositol-1,4,5-trisphosphate (IP_3), whose production is facilitated by G protein coupled cell surface receptors [9, 30]. Upon binding of an extracellular ligand to the receptor, phospholipase C (PLC) gets activated and cleaves membrane phospholipids which yields IP_3 . This then binds IP_3 receptors (IP_3Rs) in the endoplasmatic reticulum (ER) and thus sensitizes them for activation by Ca^{2+}. Active IP_3Rs act as Ca^{2+} channels, releasing Ca^{2+} ions from the ER lumen into the cytosol. Sarco-endoplasmatic reticulum Ca^{2+} ATPases pump Ca^{2+} back into the ER after release. The transient increases in cytosolic $[Ca^{2+}]$ trigger downstream effects like activation of protein kinase C [9, 74]. IP_3Rs are organized as clusters of about 1 to 20 IP_3R molecules [68, 91, 98]. A schematic overview of the release mechanism is shown in figure 2.1. Upon sensitization by IP_3, the clusters are successively activated by Ca^{2+}-induced Ca^{2+} release (CICR). This mechanism is based on the opening probability of IP_3Rs, which increases with the local Ca^{2+} concentration, up to a threshold value where further increase of the Ca^{2+} concentration becomes inhibitory [10, 99]. The clustering of IP_3Rs implies that cellular Ca^{2+} signals result from a hierarchic cascade of single channel opening ('blips') over cluster opening ('puffs') to opening of several clusters ('wave' or 'spike'). Stochasticity is reported for all of these events [67]. Thus, the Ca^{2+} spikes arise by a multiscale

stochastic process emerging by clustering of IP_3 receptors.

An approach to model such complex stochastic systems was coined hierarchic stochastic modeling (HSM), its theoretical developments started already some years ago [61, 79]. The successful application to Ca^{2+} dynamics was achieved recently [103] and further analytical insights were gained even more recently [72] and shall be presented in the following.

2.2. An analytical approach to hierarchic stochastic modelling

In this section the general theoretical framework involved in hierarchic stochastic modeling (HSM) shall be developed. At first, the general idea to refrain from a pure Markovian description shall be motivated. The formal consequences including semi-Markovian processes, the correspondent non-Markovian Master equations and the concept of probability fluxes will be discussed subsequently. Finally, a specific Ca^{2+} model developed in ref. [103] shall be analytically solved in the context of a first passage time problem.

2.2.1. What is HSM ?

The main goal of HSM is a state space reduction without fully neglecting the microscopic dynamics of the system. As to be seen in the following, this effectively implies a semi-Markovian description. However, the greater theoretical challenge is paid off well by a substantial reduction in the number of free parameters in the model. Additionally, it makes the theory readily applicable to experiments, which especially in molecular biology rarely observe microscopic state changes directly. This is due to the enormous complexity of actual molecular interactions often found for elementary cellular processes such as transcription, translation or Ca^{2+} signaling. The many cooperative interactions translate via combinatorics to high dimensional state spaces which in turn make the application of standard methods like the chemical master equation often intractable. The integration of many microscopic states into one mesoscopic observable state is therefore a naturally choice for the description of intracellular processes and is the core idea of HSM.

When describing a receptor channel molecule, often the main question of interest is if the channel is open or closed. The receptor molecule might have many internal states where only one corresponds to the channel being open [22, 93]. However, in a standard Markovian description, all internal state transitions have to be described, also the ones which are not leading to an opening event. The classical master equation reads

$$\frac{\partial}{\partial t} P_i^j(t) = \sum_{l=1}^{N} \left[q_{li} P_l^j(t) - q_{il} P_i^j(t) \right]. \tag{2.1}$$

Here, N is the number of system states and $P_i^j(t) = P(i,t|j,0)$ is the conditional probability that the system is in state i at time t conditioned by being in state

j at time $t = 0$. The q_{il} are the rates for the microscopic state transitions $i \to l$. As an example the state space of a single hypothetical channel molecule with four internal states is shown in figure 2.2. The system becomes quickly intractable if one considers multiple, say N_{ch} copies, of such a receptor as the state space dimension grows by a power law $N \sim 4^{N_{ch}}$. However, only transitions to or from state x_4 change the functional state of the channel, all other internal transitions do not trigger an opening or closing event. Thus, on a higher systems level where these internal dynamics are of no explicit interest, an integration of all microscopic states corresponding to the observable *closed* state is reasonable. Together with a corresponding *open* state this effectively reduces the number of states per receptor to two, S_1 and S_2. Given that realistic channel models often consider eight or more internal states [22], this greatly reduces the state space dimension, which now grows according to $N \sim 2^{N_{ch}}$.

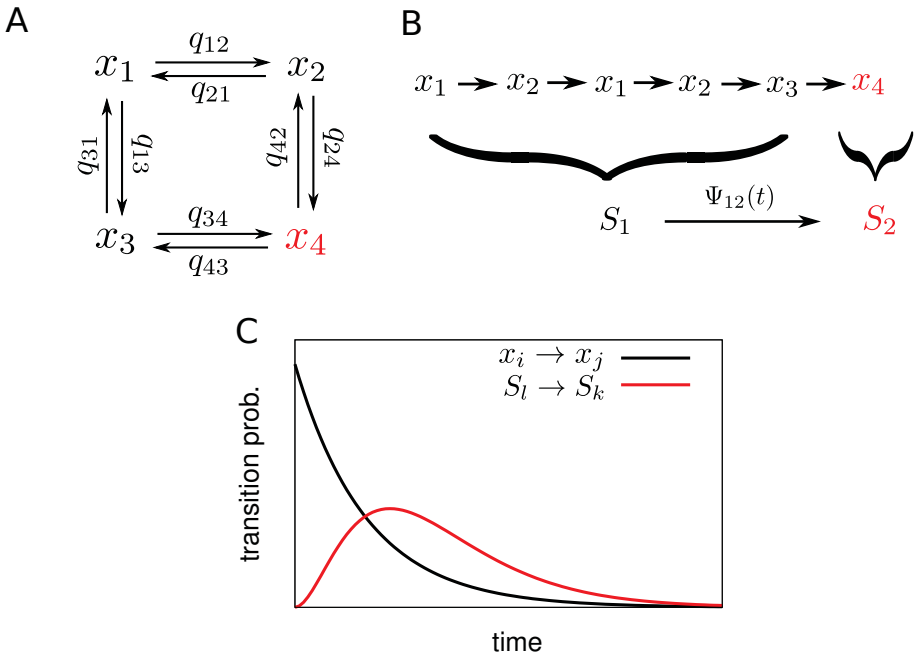

Figure 2.2.: (A) State space of a hypothetic Ca^{2+} channel with four microscopic states and associated Markovian transition rates $q_{i,j}$. The channel is considered as open only for state x_4 and closed for all other states. (B) Sketch of the HSM ansatz which combines many microscopic states x_i to fewer functional observable states S_i. (C) The transitions between this functional states are modeled by non-exponential waiting time densities $\Psi_{i,j}$ in contrast to the exponential waiting times with rates given by the $q_{i,j}$ describing the Markovian transitions between microscopic states. Figure taken from ref. [72]

In a standard coarse-grained stochastic systems description, simple rates would be assigned to the transitions between S_1 and S_2 to preserve the Markovian properties of the model. This would, however, completely neglect the underlying microscopic dynamics. A more realistic approach is to consider explicitly non-

exponential waiting times $\Psi_{i,j}$ for the observable state transitions, as these still carry information about the underlying microscopic state transitions. In the following, the corresponding mathematical framework called semi-Markov processes shall be introduced. The concept of ordinary Markov processes shall also be briefly discussed in that context.

2.2.2. Semi-Markov processes

The stochastic process of consideration $X(T_n)$ has the finite sample space $\Omega = \{0, 1, ..., N\}$ consisting of all states the process can visit. The $T_n \in \mathbb{R}^+$ form the sequence of transition times between these states with $T_0 < T_1 < ... < T_n$. Now transition probabilities according to

$$Q_{i,j}(\tau) = \mathrm{P}\{X_{n+1} = j, T_{n+1} - T_n \leq \tau | X_n = i\} \tag{2.2}$$

can be formulated. The process is temporally homogeneous by noting the independence of $Q_{i,j}(\tau)$ from n, and it is also assumed $Q_{i,j}(0) = 0$.

A process which is governed by Eq. 2.2 is called a semi-Markov process [16, 20, 83], with $Q = \{Q_{i,j}(\tau); i, j \in \Omega, \tau \in \mathbb{R}^+\}$ forming a so called semi-Markovian kernel. The reasoning behind that terminology will be briefly summarized. By defining

$$p_{i,j} = \lim_{\tau \to \infty} Q_{i,j}(\tau) \tag{2.3}$$

one gets the transition probabilities for the $i \to j$ transition of the embedded Markov chain with normalization condition $\sum_j^{N_i} p_{i,j} = 1$. In case of a pure Markov process with unconditioned transition rates $q_{i,j}$

$$p_{i,j} = \frac{q_{i,j}}{\sum_{k,i \neq j}^{N} q_{i,k}} \tag{2.4}$$

holds. Now one can define the following probability distributions:

$$G_{i,j}(\tau) = \frac{Q_{i,j}(\tau)}{p_{i,j}} = \mathrm{P}\{T_{n+1} - T_n \leq \tau | X_n = i, X_{n+1} = j\}. \tag{2.5}$$

The successive visits of the process X_n form a Markov chain with transition probabilities $p_{i,j}$, whereas the length of the sojourn time intervals $[T_n, T_{n+1})$ are given by the distribution functions $G_{i,j}(\tau)$. If these distributions can be written as $G_{i,j}(\tau) = 1 - \mathrm{e}^{-\sum_k q_{i,k}\tau} \equiv G_i(\tau)$, than the process is a pure Markov process with rates $q_{i,j}$, the sojourn times are exponentially distributed and independent of the next state. In that case the process is memoryless, which means that

$$\mathrm{P}\{T_{n+1} - T_n > s + t | T_{n+1} > t\} = \mathrm{P}\{T_{n+1} - T_n > s\}, \tag{2.6}$$

for $s, t > 0$ applies.

In conclusion, a semi-Markov process (X, T_n) still fulfills the Markov property with respect to the subsequent state transitions, but allows arbitrary (with respect to $\sum_j \lim_{\tau \to \infty} Q_{i,j}(\tau) = 1$) sojourn time distributions and hence looses its memorylessness with respect to the transition times $T_{n+1} - T_n$. It is therefore

the ideal framework to apply the desired non-exponential waiting times used by the HSM approach, now exactly defined by:

$$\frac{d}{d\tau}Q_{i,j}(\tau)d\tau = \Psi_{i,j}d\tau = \mathrm{P}\{t < T_{n+1} - T_n < \tau + d\tau | X_{n+1} = j, X_n = i\}. \quad (2.7)$$

Therefore, the term conditioned waiting time seems appropriate. By noting that the transition probabilities of the embedded Markov chain are given by $p_{i,j} = \int_0^\infty \Psi_{i,j}(\tau)dt$, the semi-Markov process is completely defined by a set of conditioned waiting time densities. Also note that by definition of the transition probabilities in Eq. 2.2, the time variable τ does not correspond to a systems time, but describes the wait after the last transition T_n.

2.2.3. Non-Markovian master equations and first passage times

By substituting the Markovian rates $q_{i,j}$ with the semi-Markovian waiting time densities $\Psi_{i,j}$ to describe the state transitions $i \to j$, the conventional Master equation is no longer applicable. It is replaced by a more general formulation:

$$\frac{dP_{i,j}(t)}{dt} = \sum_{l\neq j}^{N} I^i_{l,j}(t) - \sum_{l\neq j}^{N} I^i_{j,l}(t), \quad (2.8)$$

which employs the concept of probability fluxes. $I^i_{l,j}(t)$ denotes the probability flux for the transition from state l to j under the condition that the process started at state i at time $T_0 = 0$. Following the arguments of ref. [79] these fluxes are in turn recursively determined by the waiting time densities:

$$I^i_{l,j}(t) = \int_0^t \Psi_{l,j}(t-\tau) \sum_{k}^{N_{in}} I^i_{k,l}(\tau)d\tau + f^i_{l,j}(t). \quad (2.9)$$

This is a convolution of the conditioned waiting time to go from state j to l and all incoming fluxes to the state j. The $f^i_{l,j}$ are the initial fluxes with $f^i_{l,j}(t) \equiv 0$ for $i \neq l$. Plugging this equation into the non-Markovian Master equation 2.8 yields an integro-differential equation for the probabilities $P_{i,j}(t)$. Because the integral equation for the fluxes constitutes a convolution kernel, a solution by the Laplace Transform $\mathcal{L}\{f(t)\} = \int_0^\infty e^{-st} f(t)dt = \tilde{f}(s)$ seems promising as

$$\mathcal{L}\{f(t) * g(t)\} = \mathcal{L}\{f(t)\}\mathcal{L}\{g(t)\} \quad (2.10)$$

holds. This effectively turns equation 2.9 into an algebraic problem for the Laplace transformed fluxes $\tilde{I}^i_{l,j}$, which can be solved by standard methods given a transition structure defined by a set of $\Psi_{i,j}$'s. The application to a specific Ca^{2+} spiking model is the subject of the next subsection.

An important quantity for stochastic processes with many applications is the first passage time (FPT), given by a FPT density $F_{i,j}(t)$. It assigns a probability that the stochastic process started in state i at time $t = 0$ will first visit state j at time t. The state j often constitutes a threshold or is special by other means, so it is of interest to assess its FPT distribution. An elegant way of obtaining an

expression for the FPT is the renewal equation [107]. It formulates the general identity that the probability to start in state i at time 0 and to be in state j at time t with $i \neq j$ is equal to the probability to arrive there for the first time at any time between 0 and t and to recur there at time t

$$P_{i,j}(t) = \int_0^t d\tau F_{i,j}(t-\tau) P_{j,j}(\tau). \tag{2.11}$$

This constitutes an integral equation with convolution kernel for $F_{i,j}(t)$, by using equation 2.10 the algebraic equation for the Laplace transformed FPT reads

$$\tilde{F}_{i,j}(s) = \frac{\tilde{P}_{i,j}(s)}{\tilde{P}_{j,j}(s)}. \tag{2.12}$$

As the Laplace transform is also used to solve for the probability fluxes, what remains is to transform the non-Markovian Master equation 2.8:

$$s\tilde{P}_{i,j}(s) - \delta_{ij} = \sum_l \tilde{I}^i_{l,j}(s) - \sum_l \tilde{I}^i_{j,l}(s). \tag{2.13}$$

Putting everything together one obtains a formula for the Laplace transformed FPT density:

$$\tilde{F}_{i,j}(s) = \frac{\sum_l \tilde{I}^i_{l,j}(s) - \sum_l \tilde{I}^i_{j,l}(s)}{\sum_l \tilde{I}^j_{l,j}(s) - \sum_l \tilde{I}^j_{j,l}(s) + 1}. \tag{2.14}$$

Together with equation 2.9, a set of waiting time densities $\Psi_{i,j}$ completely determines the FPT problem as an algebraic problem in Laplace space. The big advantage of this approach emerges by noting that

$$-\frac{\partial}{\partial s}\tilde{f}(s)\Big|_{s=0} = \int_0^\infty t\ f(t)dt, \tag{2.15}$$

which equals the first moment of t when $f(t)$ is a probability density. By successive application of the derivative with respect to s one obtains for the moments of the FPT density:

$$\langle t^n \rangle = (-1)^n \frac{\partial^n}{\partial s^n}\tilde{F}_{i,j}(s)\Big|_{s=0}. \tag{2.16}$$

Hence, it is possible to calculate arbitrary moments from the Laplace transformed FPT density $\tilde{F}_{i,j}$ without facing the often cumbersome back transformation to the time domain.

Before directly applying this analytical method to a complex real life example, namely stochastic Ca^{2+} signaling, it shall be demonstrated on a small example system in the next section. There, also the conceptual differences between Markovian and semi-Markovian system descriptions shall be briefly discussed.

2.2.4. A simple semi-Markovian system

In this section, the developed analytic method to solve the FPT problem for semi-Markovian systems shall be demonstrated on a small example system.

Additionally, some considerations about the equivalence of semi-Markovian and Markovian systems in the context of FPTs shall be developed. The system under consideration is a linear chain comprised of only three states. Therefore, the system exhibits a simple transition structure shown in figure 2.3.

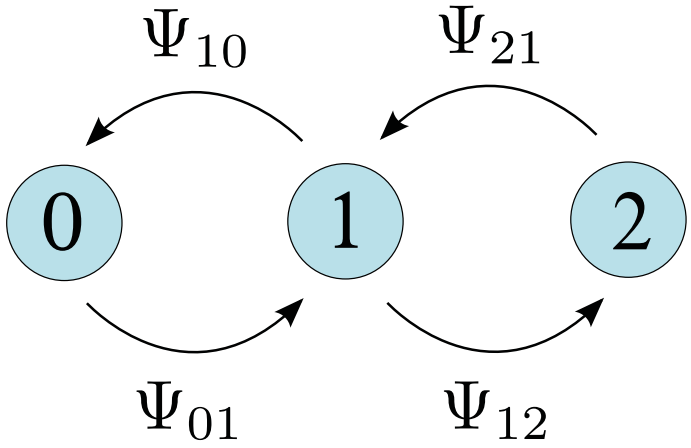

Figure 2.3.: Schematic state space and transition overview of a small example system, which only has three states and constitutes a linear chain. Is is used to demonstrate the developed first passage time formalism in the preceding section. If this system is Markovian or semi-Markovian depends on the definitions of the conditioned waiting times $\Psi_{i,j}$. Both cases will be studied in the main text.

Without fixing the conditioned waiting times $\Psi_{i,j}$, the transition structure imposed in figure 2.3 is sufficient to derive a general solution of the FPT problem to go from state 0 to state 2. Equation 2.14 of the preceding section gives the Laplace transformed FPT density in terms of the Laplace transformed fluxes. The fluxes in turn are given by the solution of equation 2.9, which in Laplace space is a matrix equation:

$$\tilde{\mathbf{I}}^j = \tilde{\mathbf{\Psi}}\tilde{\mathbf{I}}^j + \tilde{\mathbf{f}}^j, \tag{2.17}$$

basic algebra yields

$$\tilde{\mathbf{f}}^j = (\mathbb{1} - \tilde{\mathbf{\Psi}})\tilde{\mathbf{I}}^j. \tag{2.18}$$

Here $\tilde{\mathbf{I}}^j$ denotes the vector of the probability fluxes $\tilde{\mathbf{I}}^j = (\tilde{I}^j_{01}, \tilde{I}^j_{10}, \tilde{I}^j_{12}, \tilde{I}^j_{21})$ and the $\tilde{\mathbf{f}}^j$ are the initial function vectors $\tilde{\mathbf{f}}^0 = (\tilde{\Psi}_{01}, 0, 0, 0)$ and $\tilde{\mathbf{f}}^2 = (0, 0, 0, \tilde{\Psi}_{21})$. The superscript denotes the respective initial state of the system, where both the starting (0) and the destination (2) state are needed given the renewal approach in equation 2.11. Finally $\tilde{\mathbf{\Psi}}$ is the matrix of conditioned waiting times, which is completely determined by the transition structure of the simple example system:

$$\tilde{\mathbf{\Psi}} = \begin{pmatrix} 0 & \tilde{\Psi}_{01} & 0 & 0 \\ \tilde{\Psi}_{10} & 0 & 0 & \tilde{\Psi}_{10} \\ \tilde{\Psi}_{12} & 0 & 0 & \tilde{\Psi}_{12} \\ 0 & 0 & \tilde{\Psi}_{21} & 0 \end{pmatrix}.$$

The matrix equation 2.18 is an inhomogeneous linear system of equations for the Laplace transformed fluxes $\tilde{I}_{il}$ which can be solved exactly by standard algebraic methods. The solution yields all Laplace transformed fluxes as algebraic expressions of the Laplace transformed waiting times. Plugging these in equation 2.14 gives the general solution of the FPT problem in Laplace space:

$$\tilde{F}_{0,2}(s) = \frac{\tilde{\Psi}_{01}\tilde{\Psi}_{12}}{1-\tilde{\Psi}_{01}\tilde{\Psi}_{10}}. \tag{2.19}$$

Following equation 2.16 the mean first passage time is given by:

$$\langle t\rangle_{0,2} = -\frac{\partial}{\partial s}\tilde{F}_{0,2}(s)\Big|_{s=0}. \tag{2.20}$$

After differentiation and defining $\Upsilon = 1-\tilde{\Psi}_{01}\tilde{\Psi}_{10}$ one obtains:

$$\langle t\rangle_{0,2} = -\frac{1}{\Upsilon}\left[\left(\frac{\tilde{\Psi}_{01}\tilde{\Psi}'_{01}\tilde{\Psi}_{10}}{\Upsilon}+\tilde{\Psi}'_{01}\right)\tilde{\Psi}_{12}+\left(\frac{\tilde{\Psi}_{01}\tilde{\Psi}_{12}\tilde{\Psi}'_{10}}{\Upsilon}+\tilde{\Psi}'_{12}\right)\tilde{\Psi}_{01}\right]\Bigg|_{s=0}, \tag{2.21}$$

where the variable s was suppressed for better readability. This equation only contains expressions of the form $\tilde{\Psi}_{i,j}(0)$ and $\tilde{\Psi}'_{i,j}(0)$ which have a straightforward interpretation. By using the Laplace transformation property shown in equation 2.15 and the definitions of the preceding section about semi-Markovian systems (equations 2.5 and 2.7) one obtains:

$$\begin{aligned}\tilde{\Psi}_{i,j}(0) &= \int_0^\infty \Psi_{i,j}(t)dt = p_{i,j}\\ \tilde{\Psi}'_{i,j}(0) &= -\int_0^\infty t\ \Psi_{i,j}(t)dt = -p_{i,j}T_{i,j}.\end{aligned} \tag{2.22}$$

Here the $p_{i,j}$ are the familiar transition probabilities of the embedded Markov chain and the $T_{i,j}$ are the individual mean waiting times to go from state i to the adjacent state j. Applying these relations to equation 2.21 finally gives:

$$\langle t\rangle_{0,2}^{semi} = \frac{1}{p_{12}}\left(T_{01}+p_{10}T_{10}+p_{12}T_{12}\right). \tag{2.23}$$

Hence, the mean FPT only depends on the mean individual waiting times $T_{i,j}$ and the transition probabilities $p_{i,j}$. This general solution, i.e. no specific $\Psi_{i,j}$'s have been used yet, allows to compute the mean FPT without the need for a single explicit Laplace transformation. It additionally paves the way to assess the equivalence of Markovian and semi-Markovian systems with respect to FPTs.

To introduce a Markovian systems description, rates are assigned for each transition:

$$0 \underset{\gamma}{\overset{\lambda}{\rightleftharpoons}} 1 \underset{\gamma}{\overset{\alpha}{\rightleftharpoons}} 2$$

The theory of continuous time Markov chains [37] states that the unconditioned waiting time densities are the following: $\Phi_0(t) = \lambda e^{-\lambda t}, \Phi_1(t) = (\alpha+\gamma)e^{-(\alpha+\gamma)t}$ and $\Phi_2(t) = \gamma e^{-\gamma t}$. By considering the transition probabilities of the embedded (discrete time) Markov chain, namely $p_{01} = 1$, $p_{10} = \frac{\gamma}{\alpha+\gamma}$, $p_{12} = \frac{\alpha}{\alpha+\gamma}$ and $p_{21} = 1$, we can define the Markovian conditioned waiting times according to the definitions of section 2.2.2:

$$\begin{aligned} \Psi_{01} &= p_{01}\Phi_0 = \lambda e^{-\lambda t} \\ \Psi_{10} &= p_{10}\Phi_1 = \gamma e^{(\alpha+\gamma)t} \\ \Psi_{12} &= p_{12}\Phi_1 = \alpha e^{(\alpha+\gamma)t} \\ \Psi_{21} &= p_{21}\Phi_2 = \gamma e^{-\gamma t}. \end{aligned} \tag{2.24}$$

The individual mean waiting times are $T_{0,1} = 1/\lambda$, $T_{1,0} = T_{1,2} = 1/(\alpha+\gamma)$ and $T_{2,1} = 1/\gamma$. Noting the symmetry $T_{1,0} = T_{1,2}$ simplifies equation 2.23 even further, therefore the solution of the Markovian FPT problem is:

$$\langle t \rangle_{0,2}^{Markov} = \frac{1}{p_{1,2}} \left(T_{0,1} + T_{1,2}\right) = \frac{\lambda+\alpha+\gamma}{\lambda\alpha} \tag{2.25}$$

A striking feature of Markovian systems is that the waiting time distributions are the same for all possible transitions from a specific state i. This symmetry implies for the conditioned waiting times

$$\Psi_{i,j}^{Markov}(t) \equiv p_{i,j}\Phi_i(t) = q_i e^{-\sum_j q_{i,j} t}, \tag{2.26}$$

where the sum goes over all directly adjacent states. The Markovian waiting times are given by $\Phi_i = \sum_j q_{i,j} e^{-\sum q_{i,j} t}$ and the transition probabilities by $p_{i,j} = q_i / \sum_j q_{i,j}$. Moreover, for Markovian systems the transition probabilities and the individual waiting times are not independent, but are both determined by the rates $q_{i,j}$. On the contrary, for semi-Markovian systems, transition probabilities and transition times are completely independent:

$$\Psi_{i,j}^{semi}(t) \equiv p_{i,j}\Phi_{i,j}(t). \tag{2.27}$$

Here the $\Phi_{i,j}$'s are arbitrary probability density functions on the non-negative reals and the transition probabilities can be freely chosen as long as $\sum_j p_{i,j} = 1$ is fulfilled. This has far-reaching consequences, e.g. highly probable transitions can be arbitrarily slow and vice versa. In the spirit of HSM, it is interesting to think about how to (re-)construct the large Markovian (microscopic) system, which, with the right state space partitioning, operates a specific semi-Markovian (observable) systems dynamic. Although, this is beyond the scope of this work.

Finally, Markovian and semi-Markovian systems with the same transition structure are equivalent with respect to the mean FPT, if the transition probabilities and the mean individual waiting times are the same for both systems. In particular that means that $T_{i,j} = T_i$ must hold for the semi-Markovian system, which is a symmetry Markovian systems naturally obey. Although this does not necessarily impose a symmetry on the semi-Markovian waiting times (i.e.

$\Phi_{i,j} \equiv \Phi_i$), as only their first moment must coincide. It is straightforward to extend this argumentation to the nth moment of the FPT, as this would lead to an expression for $<t^n>$ containing all derivatives of the waiting times: $[\tilde{\Psi}_{i,j}(0), \tilde{\Psi}'_{i,j}(0), ..., \Psi^n_{i,j}(0)]$. Hence, if also higher moments of the individual waiting times coincide, there is still equivalence. Although in practice, already the variances (2nd moment) of the semi-Markovian $\Phi'_{i,j}s$ will generally differ from the variances of the Markovian exponential waiting times, which are simply given by $T^2_{i,j} = 1/(\sum q_{i,j})^2$.

Having now assembled and demonstrated all theoretical tools needed for an application of HSM to Ca^{2+} signaling, a specific analytically treatable Ca^{2+} model shall be analysed in the following. The non-exponential waiting times defined in the context of semi-Markov processes will be employed to describe the intracellular stochastic Ca^{2+} release process. The inter spike interval statistics will be treated as a FPT problem, which solution strategy was outlined in the previous section.

2.2.5. Explicit solutions for the tetrahedron Ca^{2+} model

The intracellular Ca^{2+} release mechanism functions, as introduced in section 2.1, by subsequent openings of IP_3 receptor clusters. These IP_3Rs are sensitive both towards IP_3 , which concentration is controlled by an external stimulus, and Ca^{2+} , which concentration is dependent on already open IP_3Rs . This calcium induced calcium release (CICR) mechanism constitutes a positive feedback, where the opening of a single IP_3R may eventually trigger a global Ca^{2+} wave. Such an event is characterized by the short-lived cellular state where the majority of the IP_3R clusters are open, evoking a sharp Ca^{2+} concentration spike. The CICR mechanism heavily relies on spatial coupling between the IP_3Rs , mediated by Ca^{2+} diffusion. The diffusion profile upon the opening of an IP_3R had been characterized as very steep [101]. This effectively means, that the IP_3Rs constituting a cluster are almost certainly coupled, whereas all other more distant IP_3R clusters only open with a certain probability determined by the local Ca^{2+} concentration. This opening probability is therefore generally dependent on the number of already opened IP_3R clusters and their respective distances. The model under consideration here exploits the spatial symmetry of a tetrahedral arrangement and consequentially consists of only four clusters [103]. All states with the same number of open clusters are equivalent with respect to the resulting Ca^{2+} concentration profile. For this specific setting, the clusters are interchangeable and the opening probabilities are only dependent on the total number of open clusters as they are all equidistant. In summary the system consists of $N = 5$ distinct states $S_0, ..., S_4$ ordered in a linear chain, corresponding to $(0, 1, 2, 3, 4)$ open clusters. A schematic overview of the model is shown in figure 2.4. The HSM approach applies to the cluster opening and closing probabilities, the 'puffs', which are described by non-exponential waiting times. The microscopic single channel dynamics, the 'blips', within a cluster are not explicitly considered, which greatly reduces the state space. A Ca^{2+} spike is defined to occur when the system is in state S_4. The ISI is therefore defined by the time the system takes for the transition from state S_0 to state S_4

and corresponds to the FPT $F_{0,4}$. The moments of the ISI distribution can be analytically calculated according to the method devised in the previous section 2.2.3. Before constructing the model, the meaning of such an idealized and small Ca^{2+} model shall be discussed briefly. Firstly, the initiation of a global cellular Ca^{2+} release wave, called wave nucleation, often arises from an initial event with a few clusters involved. Preferred nucleation areas have indeed been observed, e.g. in hepatocytes [25]. The minimal number of open clusters causing a global spike with almost certainty is called the critical nucleus. In that sense, modeling only a small number of clusters can be sufficient to capture the global Ca^{2+} dynamics. Secondly, this simplified Ca^{2+} model has led to powerful predictions which were experimentally verified [105] and which shall be discussed later in this work in section 2.5.

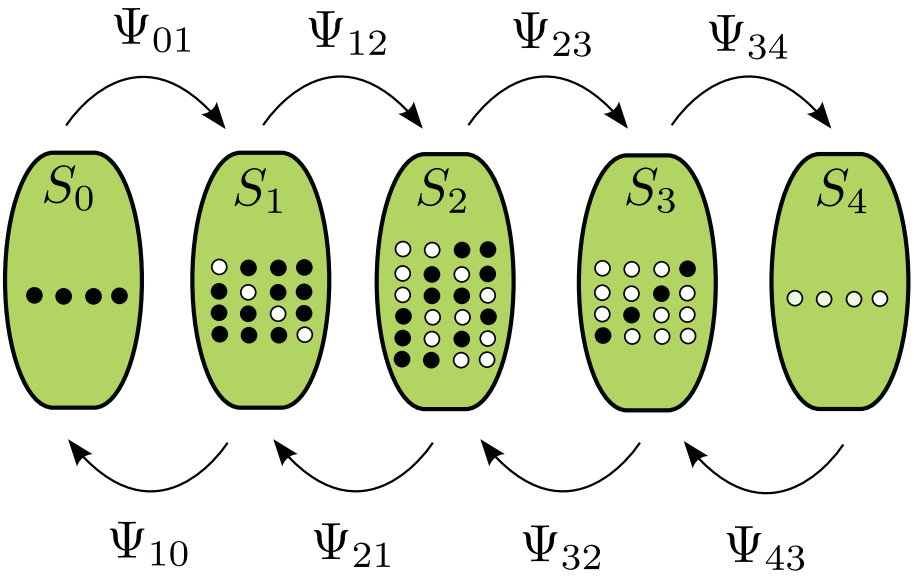

Figure 2.4.: Schematic state space and transition overview of the tetrahedron Ca^{2+} model, constituting a linear chain. Four clusters are considered, which due to symmetry make up to five states, corresponding to $(0, 1, 2, 3, 4)$ open clusters, in total. The interchangeable system states are depicted as sets of four circles each, a $\bullet$ marks a closed cluster and a $\circ$ marks an open cluster. Without the enforcement of spatial symmetry, the system would consist of up to 16 disparate states.

At first, the waiting time density for the closing of a single IP_3R cluster, $\Psi_c(\tau)$ shall be examined. As stated earlier, such a cluster consists of a number of single IP_3Rs acting as Ca^{2+} channels. The individual channels in a cluster close independently with closing rate γ, which does not depend on the Ca^{2+} concentration and is a molecular property of the IP_3Rs [91]. The channel closing rate has recently been determined by total internal reflection fluorescence (TIRF) microscopy and is $\gamma = 59\ s^{-1}$ in SH-SY5Y cells [91]. Based on that, the waiting time density for closing of an IP_3R cluster with on average N_{ch} channels involved

in a puff is given by:

$$\Psi_c(\tau) = \mathrm{N_{ch}}\gamma e^{-\gamma\tau}\left(1 - e^{-\gamma\tau}\right)^{\mathrm{N_{ch}}-1}. \tag{2.28}$$

For the opening probability densities, no such straightforward derivation as for the closing times is possible. Their general form has been experimentally assessed by inter puff interval analysis of single IP_3R clusters [104], and approximations by gamma distributions have shown reasonable simulation results [103]. Here another two-parameter distribution, termed generalized exponential (GE) function [42], shall be used to capture the opening transition of a single cluster $\Psi_o(\tau)$. The main reason for this specific choice is, that GE functions are better suited for an analytical treatment involving Laplace transformations, as needed to solve for the FPT problem. Besides, their closeness to the gamma distribution has been established [41]. It reads

$$\Psi_{o,i}(\tau) = \alpha_i\lambda_i\ \left(1 - e^{-\lambda_i\tau}\right)^{\alpha_i-1}\ e^{-\lambda_i\tau}, \tag{2.29}$$

$\alpha \geq 1$ is the shape parameter and $\lambda > 0$ is the scale parameter. The waiting time distributions depend on $[Ca^{2+}]$ and consequently on the number of open clusters. Therefore a subscript i is added, i.e. $\Psi_{o,i}$ which describes the opening probability of a cluster at system state i. The determination of the dependence of the parameters α_i and λ_i on cellular parameters is based on computations by a method developed in an earlier study by the Falcke lab [46, 102]. The method uses the De Young-Keizer model [22] for the description of the individual IP_3Rs . On the basis of that model, the $\Psi_{o,i}$'s can be computed from the master equation describing the random channel state changes. Briefly, the De Young-Keizer model assumes that a channel is open when three out of the four subunits of the IP_3R are bound by IP_3 and activating Ca^{2+}, but not by inhibiting Ca^{2+}. The transition rates between the states could be determined by experiments to some extent. Analytical approximations to the simulation results then give functional relations of the form $\alpha_i(x)$ and $\lambda_i(x)$, where $x = [Ca^{2+}]$, $[IP_3]$, $\mathrm{N_{ch}}$. Details can be found in the SI of ref. [72]. The opening of the very first cluster, a puff, is well described by a Poisson process which has a exponential waiting time density [103, 104]. Hence, for $\Psi_{o,0}$ one has $\alpha_0 = 1$ and the puff rate was experimentally [104] determined to be $\lambda_0 = 0.31s$.

The probability not to have left a state by time τ after arrival at time 0 is $\bar{\psi}_{o,c}(\tau) = 1 - \int_0^\tau \psi_{o,c}(\tau')d\tau'$, for opening or closing of a single cluster, respectively. It is noteworthy to restate, that in accordance with the frame work of semi-Markov processes introduced in section 2.2.2, the time variable τ does not correspond to a systems time, but describes the wait after the last transition to state i. A specific transition from i to $i \pm 1$ open clusters, is the product of the probabilities that all but one cluster remain at their respective states multiplied by a opening or closing waiting time density:

$$\begin{aligned}
\Psi_{i,i+1} &= (4-i)\psi_{o,i} \times \left(\bar{\psi}_c\right)^i \times \left(\bar{\psi}_{o,i}\right)^{3-i} \\
\Psi_{i,i-1} &= i\psi_c \times \left(\bar{\psi}_c\right)^{i-1} \times \left(\bar{\psi}_{o,i}\right)^{4-i},
\end{aligned} \tag{2.30}$$

where the prefactors account for the multiplicity of the transitions. The individual opening time and closing time probability densities as well as the constructed conditioned waiting times $\Psi_{i,j}$ are shown in figure 2.5.

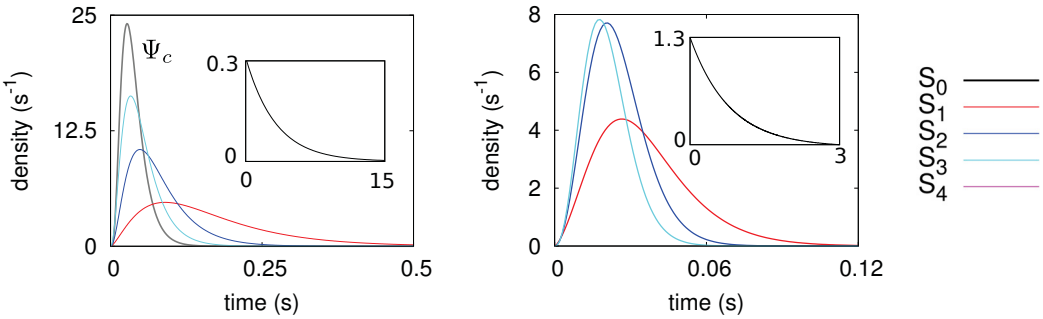

Figure 2.5.: Individual opening time and closing time probability densities $(\Psi_{o,i}, \Psi_c)$ and the conditioned waiting time densities for the consecutive opening transitions, constructed out of the closing (Ψ_c) and opening $(\Psi_{o,i})$ densities for the tetrahedron model according to equation 2.30. The colors in the legend depict the system state in terms of the number of open clusters $(S_i, i = 0, 1, 2, 3, 4)$.

Now that the transition network for the Ca^{2+} model, constituting a simple linear chain, has been fixed, the solution strategy for the FPT problem can be explicitly employed. At first the set of probability fluxes shall be calculated. By writing the set of fluxes as a vector $\mathbf{I}^j(t)$ and by writing the conditioned waiting time densities in an appropriate matrix $\mathbf{\Psi}(t)$, the system of integral equations given by equation 2.9 can be written in Laplace space as

$$(\mathbb{1} - \tilde{\mathbf{\Psi}})\tilde{\mathbf{I}}^j = \tilde{\mathbf{f}}^i. \tag{2.31}$$

This is an inhomogeneous linear system of equations for the Laplace transformed fluxes $\tilde{I}_{il}$ which can be solved exactly by standard algebraic methods. The solution yields all Laplace transformed fluxes as functions of the Laplace transformed waiting times. The flux vector can be written as $\mathbf{I}^j = (I^j_{01}, I^j_{10}, I^j_{12}, ..., I^j_{N-1,N}, I^j_{N,N-1})$ with $N = 4$ and the initial function vectors for the r.h.s. of Eq. 2.31 are $\tilde{\mathbf{f}}^0 = \left\{\delta_{i0}\tilde{\Psi}_{0,1}\right\}$ and $\tilde{\mathbf{f}}^8 = \left\{\delta_{i8}\tilde{\Psi}_{4,3}\right\}$, $i = 1, \ldots, 8$. The waiting time matrix $\mathbf{\Psi}$ is completely determined by the set of equations given in Eq. 2.9 and reads

$$\tilde{\mathbf{\Psi}} = \begin{bmatrix} 0 & \tilde{\Psi}_{0,1} & 0 & 0 & 0 & 0 & 0 & 0 \\ \tilde{\Psi}_{1,0} & 0 & 0 & \tilde{\Psi}_{1,0} & 0 & 0 & 0 & 0 \\ \tilde{\Psi}_{1,2} & 0 & 0 & \tilde{\Psi}_{1,2} & 0 & 0 & 0 & 0 \\ 0 & 0 & \tilde{\Psi}_{2,1} & 0 & 0 & \tilde{\Psi}_{2,1} & 0 & 0 \\ 0 & 0 & \tilde{\Psi}_{2,3} & 0 & 0 & \tilde{\Psi}_{2,3} & 0 & 0 \\ 0 & 0 & 0 & 0 & \tilde{\Psi}_{3,2} & 0 & 0 & \tilde{\Psi}_{3,2} \\ 0 & 0 & 0 & 0 & \tilde{\Psi}_{3,4} & 0 & 0 & \tilde{\Psi}_{3,4} \\ 0 & 0 & 0 & 0 & 0 & 0 & \tilde{\Psi}_{4,3} & 0 \end{bmatrix}. \tag{2.32}$$

As can be seen in Eq. 2.31 there are actually two sets of fluxes, reflecting the two distinct initial states needed for the FPT calculation based on the renewal equation. This formula 2.14 simplifies for the tetrahedron model to

$$\tilde{F}_{0,4} = \frac{\tilde{I}^0_{3,4} - \tilde{I}^0_{4,3}}{\tilde{I}^4_{3,4} - \tilde{I}^4_{4,3} + 1}. \tag{2.33}$$

Plugging in the solutions of the linear system given in equation 2.31 yields the Laplace transformed FPT density:

$$\tilde{F}_{0,4} = \frac{\tilde{\Psi}_{0,1}\tilde{\Psi}_{1,2}\tilde{\Psi}_{2,3}\tilde{\Psi}_{3,4}}{1 - \tilde{\Psi}_{0,1}\tilde{\Psi}_{1,0} - \tilde{\Psi}_{1,2}\tilde{\Psi}_{2,1} - \tilde{\Psi}_{2,3}\tilde{\Psi}_{3,2} + \tilde{\Psi}_{0,1}\tilde{\Psi}_{1,0}\tilde{\Psi}_{2,3}\tilde{\Psi}_{3,2}} \tag{2.34}$$

It is an algebraic expression consisting solely of Laplace transformed transition waiting times $\tilde{\Psi}_{i,j}(s)$. The Laplace transformations of the underlying opening and closing waiting times are given in the Appendix B.1. The first moment of this FPT density corresponds the average ISI ($\mathrm{T_{av}}$) in the tetrahedron Ca^{2+} model. In practice, the analytical approximations for the waiting time distribution parameters [72] are used to explicitly set up the $\Psi_{i,j}$'s depending on cellular parameters like [IP_3] or the average number of channels in a cluster N_{ch}. Then, assisted by a computer algebra program [113], $\mathrm{T_{av}}$ can be calculated using equation 2.16 of the previous section. Results are shown in figure 2.6. Equation 2.16 also allows to analytically calculate higher moments of the ISI distribution. By calculating the 2nd moment $< t^2 >$ it is possible to compute the Coefficient of Variation (CV), given by T_{av}/σ with σ denoting the standard deviation. Additionally, by calculating the 3rd moment $< t^3 >$ the skewness, given by $< t^3 > /\sigma^3$, of the ISI distribution can be computed as well. An examination of both quantities, as shown in figure 2.7, identifies the ISI distribution to be of exponential type for the parameters used in the tetrahedron model. This is in agreement with the earlier result of ref. [103] that a global feedback is necessary to reach the regime $\sigma < \mathrm{T_{av}}$, which is typically observed in experiments [90]. Unfortunately, global feedback does not allow for an exact analytical solution for the moments of the FPT density, as it makes an explicit systems time necessary. In other words, the ISI distribution is a rescaled puff distribution given by $\Psi_{o,0}$, which is exponential. The reason for that is the time scale separation between the slow single puff dynamics and the very fast consecutive cluster opening dynamics. As indicated in figure 2.5, the mean waiting time between single puffs, determined by the conditioned waiting time Ψ_{01}, is of the order of $1/4\lambda_0 \sim 1$ s. Whereas the mean waiting time for the consecutive cluster openings, determined by Ψ_{12}, Ψ_{23} and Ψ_{34}, is of the order of ~ 0.05 s. By artificial lowering the channel closing rate γ, this time scale separation becomes weaker. As depicted in figure 2.7 the ISI distribution then clearly deviates from the exponential distribution, and this effect gets even stronger with growing puff rate λ_0. This observations will be deepened and used to construct a much simpler Ca^{2+} model, called generic model, in the next section.

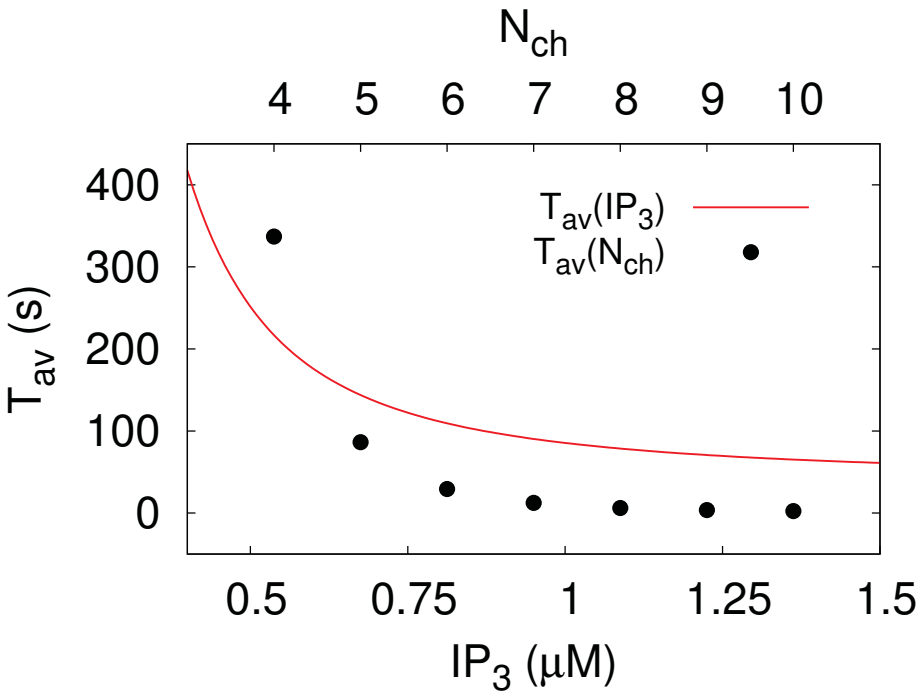

Figure 2.6.: The average ISI (T_{av}) for the tetrahedron Ca^{2+} model in dependence of two cellular parameters. Different [IP_3] correspond to different external stimulation strengths, the stronger the stimulus the lower the T_{av} and therefore the faster the spiking. N_{ch} is the average number of channels a IP_3R consists of, more channels lead to higher total opening probabilities and therefore also to shorter average ISIs. T_{av} is analytically calculated as the first moment of the first passage time density defined in the main text.

2.3. Exploiting time scale separation - The generic Ca^{2+} model

As discussed in the previous section, the single puff dynamics constituting the $S_0 \to S_1$ transitions are about 20 times slower, than the consecutive cluster openings described by the $S_i \to S_j$ transitions with $i, j = (1, 2, 3, 4)$. These are very fast and may potentially lead to a Ca^{2+} spike with all clusters open. This means, that the system upon being in state S_1, with respect to the puff time scale, almost instantaneously decides with a certain probability if this single puff becomes a global spike, or if it relaxes back to the ground state S_0 without reaching S_4. This probability is denoted the splitting probability C_{14} and is given by [103]

$$C_{14} = \frac{C_{12}C_{23}C_{34}}{1 + C_{12}(C_{23} - 1) + C_{23}(C_{34} - 1)}, \tag{2.35}$$

with the one-step splitting probabilities $C_{i,i+1} = \int_0^\infty \Psi_{i,i+1}(t)dt$. This expression is derived by considering all possible transition routes from S_1 to S_4 without touching the ground state S_0. This probability can be calculated in dependence

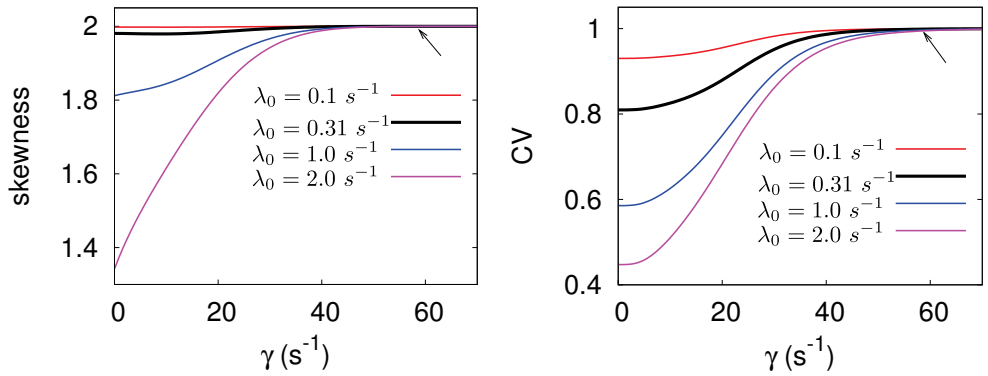

Figure 2.7.: Skewness and Coefficient of Variation of the ISI distribution of the tetrahedron Ca^{2+} model. The parameter values used for the stochastic Ca^{2+} model are indicated by the arrows. For these, the ISI distribution is of exponential type, as the CV indicates $\sigma = T_{av}$ and the skewness is exactly two. By artificially varying the channel closing rate γ the time scale separation between single puff dynamics and consecutive openings gets weaker, and the ISI distribution clearly deviates from an exponential distribution. This effect grows stronger with increasing puff rate λ_0.

on cellular parameters with the setup of the tetrahedron model, results regarding the IP_3 concentration and the number of channels N_{ch} are shown in figure 2.8. Pursuing this perspective on the system lead to the idea to separate the stochastic Ca^{2+} spike generating process into one Poisson process describing the puffs, and a Bernoulli trial with success probability C_{14}. This effectively constitutes a splitting of an inhomogeneous Poisson process which shall be elucidated in the following.

2.3.1. Model Construction

At first, the puff process shall be modeled more realistically by incorporating a negative feedback. The now time dependent puff rate is recast as

$$\lambda(t) = \lambda_0(1 - e^{-\xi t}). \tag{2.36}$$

The feedback ensures that the probability for a puff to occur at $t = 0$ is equal to zero. This better reflects physiological constrictions like internal Ca^{2+} storage depletion which inhibit puffs right after a global Ca^{2+} spike. The probability for a puff then recovers with a rate given by ξ. Equation 2.36 constitutes an inhomogeneous Poisson process for the Ca^{2+} puff dynamics. The specific form of the feedback is borrowed from ref. [90], where it was used to incorporate a global negative feedback on the global Ca^{2+} spike rate.

One can now ask for the probability that at a time point t a puff occurs and triggers a global Ca^{2+} spike. Conditioned on the ground state S_0 the time for

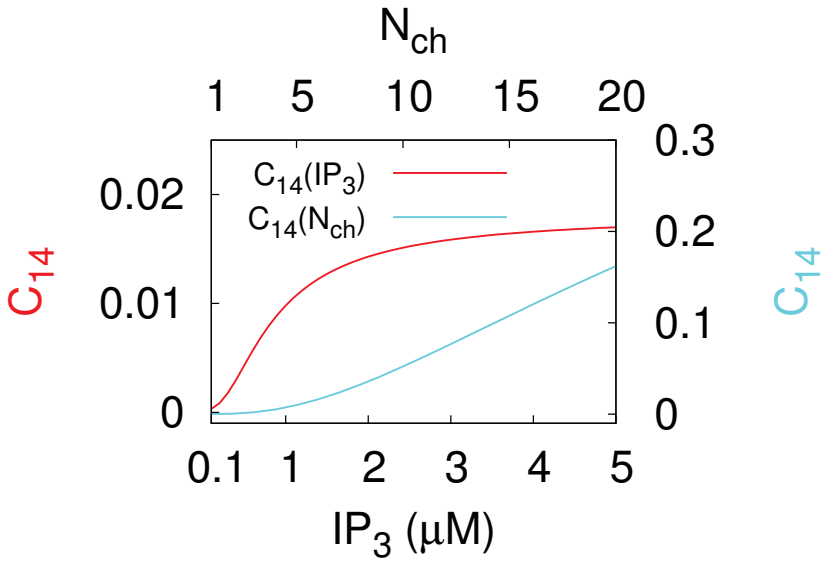

Figure 2.8.: Parameter dependencies for the splitting probability C_{14} to reach the spiking state S_4 out of a single puff state S_1 for the tetrahedron model. The axis are differently scaled for the cytosolic IP3 concentration ($[IP_3]$) and the mean number of Ca^{2+} channels per cluster participating in an opening event (N_{ch}) respectively. The splitting probability saturates for both parameters, however for the N_{ch} dependency only for a unrealistic high number of Ca^{2+} channels (N_{ch} >100)

the first Ca^{2+} spike to occur, the ISI, is of interest. Formally this leads to:

$$\begin{aligned} p_s(t) &= C_{14}\lambda(t) \times \Big(e^{-\Lambda(t)} \\ &\quad +(1-C_{14}) \int_0^t e^{-\Lambda(t_1)}\lambda(t_1) \\ &\quad +(1-C_{14})^2 \int_0^t \int_{t_1}^t e^{-\Lambda(t_1)}\lambda(t_1)e^{-(\Lambda(t_2)-\Lambda(t_1))}\lambda(t_2)e^{-(\Lambda(t)-\Lambda(t_2))}dt_1dt_2 \\ &\quad + ...\Big) \\ &= C_{14}\lambda(t)e^{-\Lambda(t)}\Big(1+(1-C_{14})\int_0^t \lambda(t_1)dt_1 \\ &\quad + (1-C_{14})^2 \int_0^t \int_{t_1}^t \lambda(t_1)\lambda(t_2 1)dt_1dt_2 + ...\Big) \end{aligned} \tag{2.37}$$

This expression contains the probabilities for all possible puffs occurring before t not leading to a spike, the failed Bernoulli trials with probability $(1-C_{14})$. The Poisson intensity at a time t is given by $\Lambda(t) = \int_0^t \lambda(t)$. The very first term is the probability that at t a puff occurs and becomes a global spike and no other puff occurs in $[0,t)$, the second term is the probability for one failed puff in $[0,t)$,

the third term handles two failed puffs and so on. Following permutation and symmetry arguments outlined in the book by Van Kampen [107] one may write:

$$\begin{aligned} p_s(t) &= C_{14}\lambda(t)e^{-\Lambda(t)}\Big(\sum_{n=0}^{\infty}\frac{1}{n!}\big((1-C_{14})\Lambda(t)\big)^n\Big) \\ &= \kappa(t)e^{-C_{14}\Lambda(t)}. \end{aligned} \tag{2.38}$$

The resulting stochastic process for the Ca^{2+} ISIs is also an inhomogeneous Poisson process with the spike rate $\kappa(t) = C_{14}\lambda(t)$ and intensity $\Lambda(t) = \int_0^t \lambda(\tau)d\tau$. The new rate is just the puff rate refined with the splitting probability C_{14}, this property is known as Poisson splitting. By writing the global spike rate as $\kappa(t) = C_{14}4\lambda_0(1-e^{\xi t})$ it is clear, that this approach yields an expression for the global Ca^{2+} spike rate: $\kappa_0 = C_{14}4\lambda_0$. The specific parameterization and structure of the tetrahedron model is by no means necessary for the generic Ca^{2+} model and its structure can be in principle generalized to multiple puff sites with individual splitting probabilities:

$$\kappa_0 = \sum_{i=1}^{N}\lambda_{0,i}C_{1N,i}. \tag{2.39}$$

This equation combines the local puff dynamics, determined by the $\lambda_{0,i}$'s, and the spatial coupling of the cluster arrangement, given by the $C_{1N,i}$'s, to yield a simple expression for the global Ca^{2+} spiking rate. Accompanied by the feedback the generic model gives results which are in good agreement with experimental data, as to be seen in the following.

2.3.2. Results of the generic model

The great advantage of the generic model is its capability of providing a closed expression for the ISI distribution, incorporating a global negative feedback and the local puff dynamics. This allows for analytically reproducing the moment relation between the standard deviation σ and the average T_{av} of spike trains found experimentally.

As the algebraic structure of the ISI distribution of the generic model, termed $p_s(t)$ in the preceding subsection, is the same as in ref. [90], the analytical expressions for the moments of the ISI derived in that work can be readily applied here. They read for the tetrahedron model setup:

$$\begin{aligned} \langle t^1\rangle &= T_{av} = \frac{e^{\Theta}(\Theta)^{1-\Theta}}{4\lambda_0 C_{14}}\Big[\Gamma(\Theta) - \Gamma(\Theta,\Theta)\Big], \\ \langle t^2\rangle &= \frac{2e^{\Theta}}{(4\lambda_0 C_{14})^2}\mathcal{F}\Big[(\Theta,\Theta),(1+\Theta,1+\Theta),-\Theta\Big], \end{aligned} \tag{2.40}$$

where $\Theta = 4\lambda_0 C_{14}/\xi$, $\Gamma(x)$ denotes the Euler gamma function, $\Gamma(x,y)$ the incomplete gamma function and $\mathcal{F}[x]$ is the generalized hypergeometric function.

These equations allow for an analytical analysis of the moment relation between T_{av} and σ for different feedback strengths ξ. As shown in figure 2.9,

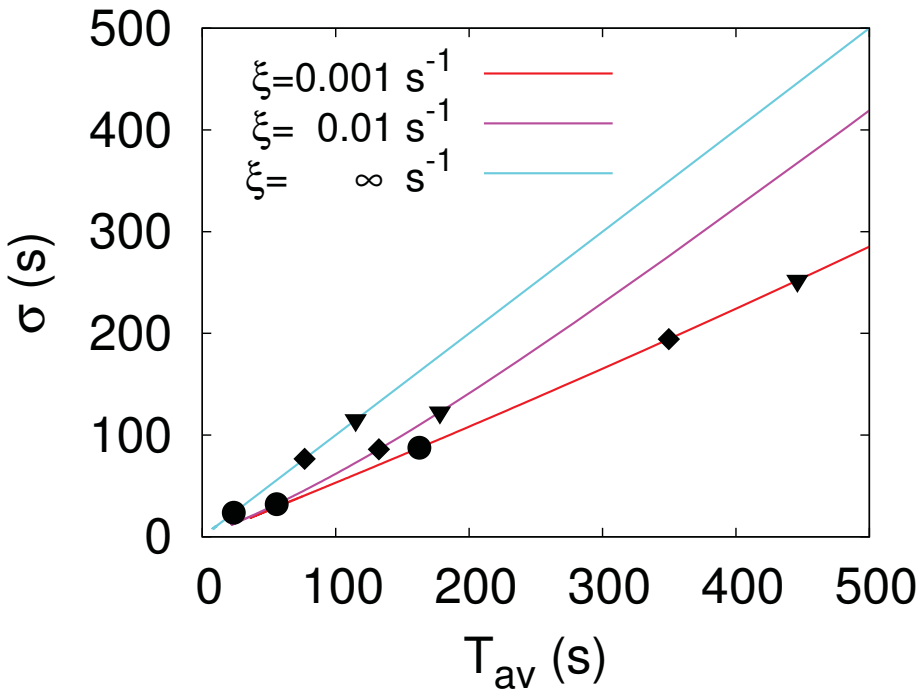

Figure 2.9.: The σ-T_{av} relations calculated with the generic Ca^{2+} model for different feedback strengths. The relations are linear with the slope being cell type specific and controlled by ξ. The position of an individual cell on a moment relation is determined by cell specific properties like cluster arrangement. This cell-to-cell variability is captured by the splitting probability C_{14} which compactly accounts for all factors contributing to the spatial coupling of the channel clusters. Individual values of T_{av} for three different values of C_{14} (● 0.05, ■ 0.01, ▲ 0.008) were added to each line. Modifications of the coupling strength merely lead to a shift of the cell along the σ-T_{av} relation and do not affect the slope of the relation.

this relation is linear with the slope controlled by ξ, which is considered as cell type specific [90, 103]. This is exactly what is observed experimentally when a cell population is analysed, and the σ-T_{av} relation is calculated for every single cell. Interestingly, the theoretical information content of Ca^{2+} spike trains is solely determined by the slope of this σ-T_{av} relation, which in turn is a robust property of a cell population [89].The individual position of a cell on the moment relation is determined by cell specific properties, like cluster arrangement. This cell-to-cell variability is in the generic model completely captured by the splitting probability C_{14} which condenses all factors contributing to the spatial coupling of clusters into one quantity. Variation of the coupling strength mediated by the value of C_{14} leads to a shift of the cell along the σ-T_{av} relation and does not affect the slope of the relation. This behavior was found in buffer experiments [89], where different buffer concentrations decreased the spatial coupling of the IP_3R clusters. This affected both σ and T_{av} of the recorded spike trains and

shifted individual cells in the σ-T_{av} plane with a slope similar to the slope of the moment relation obtained from a population of unperturbed cells.

The generic model is only an approximation of the real stochastic process governing the Ca^{2+} spike generation. Although, as demonstrated, the results are in good agreement with experiments, a quantification of the error of the approximation would be eligible. This shall be done in the following subsection.

2.3.3. Error analysis

The applied Poisson splitting ansatz completely neglects the dynamics of the system between the individual states, instead it implicitly sets all transition times except for the $S_0 \to S_1$ transition to zero. So it is expected to underestimate the true average ISI, $T_{av}^{gm} < T_{av}^{tr}$, with the generic Ca^{2+} model. The time the system spends in processing the failed puffs, the ones which do not reach the highest state S_4, is a major source for the underestimation. The number of those failed puffs is given on average by $1/C_{14}$, as these are the odds for the Bernoulli trial experiment to fail. For standard parameters this accounts for ~ 100 failed puffs to occur on average before a successful spike occurs. So the error made by using the Poisson splitting is expected to scale exactly with $1/C_{14}$. By letting the recovery rate approach infinity, $\xi \to \infty$, the negative feedback is turned off, and the results of the generic model are comparable to the exact analytic results obtained with the presented FPT formalism for the semi-Markovian tetrahedron model of section 2.2. As shown in figure 2.10 the absolute error of the average ISI, given by $T_{av}^{tr} - T_{av}^{gm}$, indeed scales linearly with $1/C_{14}$ and is of the order of ~ 10 seconds. The relative error in dependence on the IP_3 concentration, given by $(T_{av}^{tr} - T_{av}^{gm})/T_{av}^{tr}$, was also computed and remains below 10% for the physiological relevant parameter range. Additionally, the relative error saturates for $IP_3 \to \infty$ and approaches zero for $IP_3 \to 0$. The main argument for the generic model is the time scale separation between single puff dynamics and the consecutive cluster openings. In accordance with that the approximation error gets bigger with weaker time scale separation, realized by a smaller channel closing rates γ as indicated in the figures 2.10.

In summary the main source for the approximation error was identified as the neglected cluster state dynamics after a puff not leading to a spike. This error was quantified by turning off the feedback in the generic model and comparing the results for T_{av} to the exact analytic results for the tetrahedron model. It is small enough to make the Poisson splitting ansatz valid for describing the Ca^{2+} spiking dynamics, as long as the time scale separation between puff and spike dynamics is strong enough. It gets even smaller when compared to numerical results for the tetrahedron model with global feedback, as presented in the following.

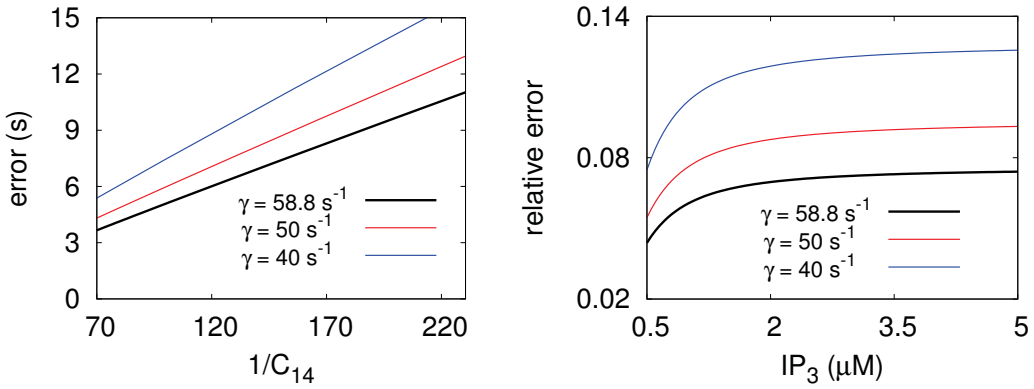

Figure 2.10.: Absolute (right) and relative (left) errors in T_{av} of the generic Ca^{2+} model, obtained by comparison with the exact results of the semi-Markovian tetrahedron model. The number of failed puffs is on average $1/C_{14}$ and the absolute error scales accordingly, as these dynamics are completely neglected by the Poisson splitting ansatz of the generic model. The relative error remains below 10% for the physiological relevant parameters and is bounded. Weakening the time scale separation by artificially varying the channel closing rate γ increases the error.

2.4. Numerical Analysis of the HSM Ca^{2+} model

A serious limitation of the analytical treatment of the tetrahedron model in section 2.2 is the impossibility of incorporating a global feedback. This is due to the formal constraints of the semi-Markovian framework: writing $\Psi_{ij}(\tau)$ for a conditioned waiting time the variable τ describes the time it will take to leave state i and land at state j. The instant $\tau = 0$ describes the event of the system just arriving at state i, there is no systems time which could for example monitor how long it has been since the spiking state S_4 was last visited. However, exactly this information is needed to incorporate a global feedback which introduces a process of recovery after a Ca^{2+} spike has occurred. As approved by analytical calculations in section 2.2 and the results of the generic model of the preceding section, such a feedback is required to reproduce the non-Poissonian σ-T_{av} relations found experimentally. As demonstrated in figure 2.7, non exponential ISI distributions can be obtained in principle within the semi-Markovian tetrahedron setup. However, the exponential puff waiting time Ψ_{01} in combination with the strong time scale separation enforced by the physiological parameters do not allow for that. However, as done in ref. [103], by falling back to numerical procedures to compute the ISIs a systems time and therefore a global feedback can be readily introduced into the tetrahedron model. A standard method for the simulation of Markovian systems is the Gillespie algorithm [36], as to be seen in the following with a slight enhancement is also applicable for semi-Markovian systems. At first, an already established algorithm shall be applied and the results compared to the generic model with global feedback.

2.4.1. The DSSA algorithm

An algorithm to simulate the semi-Markovian tetrahedron system was termed *Delayed Stochastic Simulation Algorithm* (DSSA) and developed in ref. [103]. It readily simulates realisations of the Ca^{2+} spiking process, an example is shown in figure 2.11. The global feedback is introduced in the puff transition waiting time by explicitly memorizing the time of the last spike, stored in t_{sp}, and it additionally also keeps track of the last state transition time, stored in t_p. The opening waiting time density for the first cluster to open is therefore given by [103]:

$$\begin{aligned} \Psi_{o,0}(t, t_p, t_{sp}) &= \lambda_0 (1 - e^{-\xi(t-t_{sp})})\; e^{-\lambda_0 \int_{t_p}^{t_{sp}} 1 - e^{-\xi(\tau - t_{sp})} d\tau} \\ &= \lambda_0 (1 - e^{-\xi(t-t_{sp})})\; e^{-\frac{\lambda_0}{\xi}[-e^{-\xi(t-t_{sp})} + e^{-\xi(t_p - t_{sp})} - \xi(t-t_{sp})]} \end{aligned} \tag{2.41}$$

Here, the variable t corresponds to the total systems time and the algorithm works by iterating over all timesteps between $t = 0$ and a total time T with a fixed step size dt. For every step of the iteration and for every cluster a random number U_j is drawn from a uniform distribution $U(0, 1)$ and the respective transition probabilities for every cluster j are calculated according to $P_j(t) = \int_{t-\tau}^{t-\tau+dt} \Psi_{o/c,j}(t')dt'$. The transition type is determined by the actual

state of cluster j, so Ψ_o if the cluster is closed and vice versa. If $P_j(t) > U_j$ for some epoch t, the cluster state is changed accordingly and the the time of the last transition is updated to $\tau = t$. A more detailed description of the algorithm can be found in the SI of ref. [103].

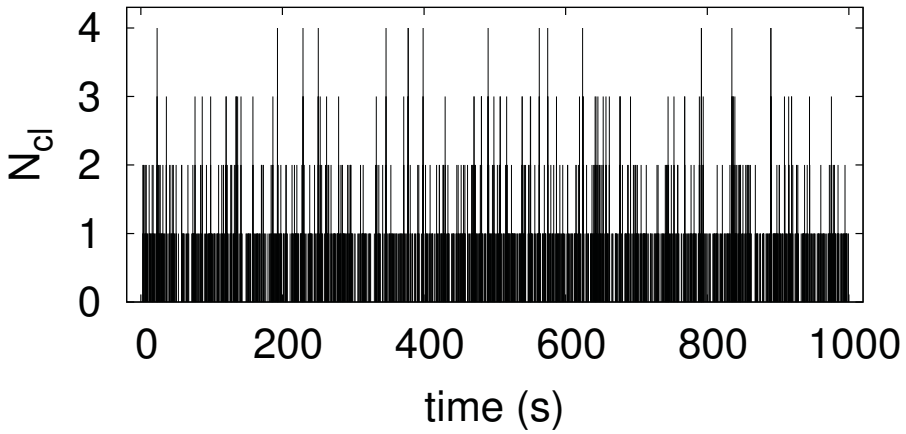

Figure 2.11.: Stochastic simulations of spike trains of the tetrahedron with the DSSA algorithm for $[IP_3] = 1\ \mu$M. There are frequent puff events with less than four clusters open in contrast to the rather isolated global spike events characterized by $N_{cl} = 4$. Such simulations with runtimes up to 10^7s can be used to compute ISI statistics by means of sample mean and sample variance.

By running very long Monte Carlo simulations, values of T_{av} and σ can be reliably computed by means of the sample mean and sample variance in dependence on cellular parameters. Their goodness has been approved by comparing this results to the analytically tractable case already in ref. [103]. Here the simulations shall be used, to demonstrate the accuracy of the generic model introduced in the preceding section with the global feedback present. As shown in figure 2.12, its results are very close to the numerical results for T_{av} . The approximation error gets even smaller for increasing feedback strengths, which cover the biologically more relevant cases as these produce σ-T_{av} relations more close to experimental data as discussed in the preceding section. The reason for that is simply, that a strong global feedback introduces a longer recovery after a Ca^{2+} spike and therefore increases the time scale separation between puff and consecutive cluster opening dynamics. This in turn lowers the relative amount of time the system spends on transitions not covered by the Poisson splitting ansatz of the generic model. These results confirm the effectiveness and elegance of the generic model, as it produces results for the moments of the ISI distribution as good as the Monte Carlo simulations of the full model with muss less effort.

The DSSA algorithm works fine for the specific setup of the tetrahedron Ca^{2+}

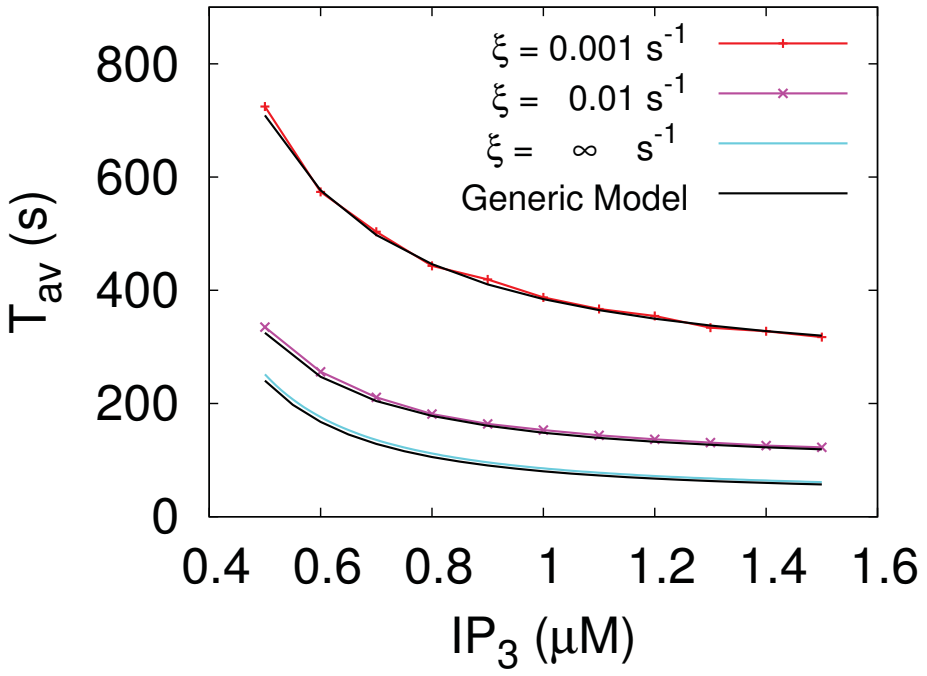

Figure 2.12.: Comparison of numerical results obtained with the DSSA algorithm for the IP_3 dependence of T_{av} with the results obtained from the generic Ca^{2+} model with global feedback. The value of ξ introduces a recovery rate of the puff probability after a global Ca^{2+} spike has occurred, the smaller ξ the longer the recovery and hence the stronger the global negative feedback. The analytical results of the generic model are very close to the simulation results, with the approximation error getting smaller for stronger feedbacks. For ξ =0.001 the values for T_{av} are almost identical, confirming the goodness of the generic model also for the biological more relevant cases with enabled feedback.

model. However, it is not readily applicable to general semi-Markovian systems as it makes no explicit use of the conditioned waiting times $\Psi_{i,j}$. Therefore a more general algorithm for semi-Markovian systems with discrete states shall be developed in the following.

2.4.2. An exact semi-Markovian simulation algorithm

The great advantage of the Gillespie algorithm (ref. [37] is a good introduction) is, that it is exact for discrete states. The DSSA algorithm is not exact in that sense, because it introduces a numerical time discretization with a step size dt and is therefore missing all possible transitions with a transition time smaller than the step size. Additionally, the original Gillespie algorithm needs exactly N iteration steps for a realisation with N transitions, which makes it in combination with the cost-effective sampling from an exponential waiting time distribution very computationally efficient. The DSSA algorithm, on the contrary, iterates

over all T/dt timesteps, irrespective of system state changes. So the goal is to devise an algorithm which shares more of the favorable properties of the original Gillespie algorithm and is generally applicable to semi-Markovian systems. As to be seen in the following this actually only requires minor changes of the original algorithm.

As discussed in section 2.2.2, semi-Markovian processes possess an embedded Markov chain with the transition probabilities given by $q_{ij} = \int_0^\infty \Psi_{ij}(\tau)d\tau$. This is completely analogue to pure discrete state Markovian systems, and in accordance to the original algorithm the next state of a realisation can be computed by simply sampling from the discrete distribution given by the set of the transition probabilities $\{q_{ij}\}$ for every state i. What is different is the determination of the next jump epoch. For a pure discrete state Markovian system, when being in state i this epoch is determined by sampling from the exponential waiting time density, often called sojourn time in the literature, given by $\Phi_i(\tau) = \sum_{k,i\neq j} q_{ik}\ e^{-\sum_{k,i\neq j} q_{ik}\tau}$. In the semi-Markovian case (see also section 2.2.4), having already determined the next state j, the next jump epoch is given by sampling from the distribution $\Phi_{i,j} = \frac{1}{q_{ij}}\Psi_{ij}(\tau)$, which is generally a non-exponential probability density function. This step will generally be more costly than in the original Gillespie algorithm, where the inverse sampling method can be used. In cases where the inverse of the distribution belonging to the waiting time Φ_{ij} is not available, other sampling methods like rejection sampling may be used to generate the next jump epoch. Having determined the next state and the next jump epoch makes the algorithm complete and it reads in pseudo code:

Define conditioned waiting time densities $\Psi_{ij}(\tau)$
Calculate transition probabilities $q_{ij} = \int_0^\infty \Psi_{ij}(\tau)d\tau$
Set total simulation time T
Set initial system state i
Set $t = 0$
while $t < T$ do:

  sample next state j from the discrete density given by the $\{q_{ij}\}$
  sample next jump epoch τ by sampling from the continuous density $\Phi_{ij}(\tau)$
  Set $t = t + \tau$
  Set new systems state $i = j$
  Record as needed transition epoch t and state j

The output of this algorithm are the cumulative transition times ($t_0 = 0,\ t_1 = \tau_1,\ t_2 = \tau_1+\tau_2, ..., t_N = \sum_0^N \tau_i$) and the respective system states ($S(t_0), S(t_1), ..., S(t_n)$). For systems with many or even an infinite number of states, the algorithm can be augmented by subprocedures which generate the Ψ_{ij}'s inside the main loop according to rules which specify the stochastic process.

This algorithm needs exactly N iterations for a realisation with N transitions and is also exact in the sense the original Gillespie algorithm is exact as there is no time discretization needed. Given a total simulation time T, the expected

number of iteration steps needed is given by the expected number of transition events happening in the interval $[0, T]$. It is clear, however, that this algorithm generally outperforms the DSSA algorithm. For that, the number of iterations needed is exactly T/dt, with dt being the step size for the time discretization. As the step size dt has to be significantly smaller than the average inter-event time $<\tau_{ev}>$ of the stochastic process to achieve a reasonable numerical precision, the exact semi-Markovian algorithm presented above will on average be $<\tau_{ev}>/dt$ times faster than the DSSA algorithm. For the parameters used for the Monte Carlo simulations shown in figure 2.12, this speedup is about a factor of 100. Setting up the Ψ_{ij}'s for the specific tetrahedron Ca^{2+} model is a bit tedious, as the conditioned waiting times according to equations 2.30 are products of powers of individual density functions for this system. But this has to be done only once, and after that the algorithm produces reliable results as shown in figure 2.13.

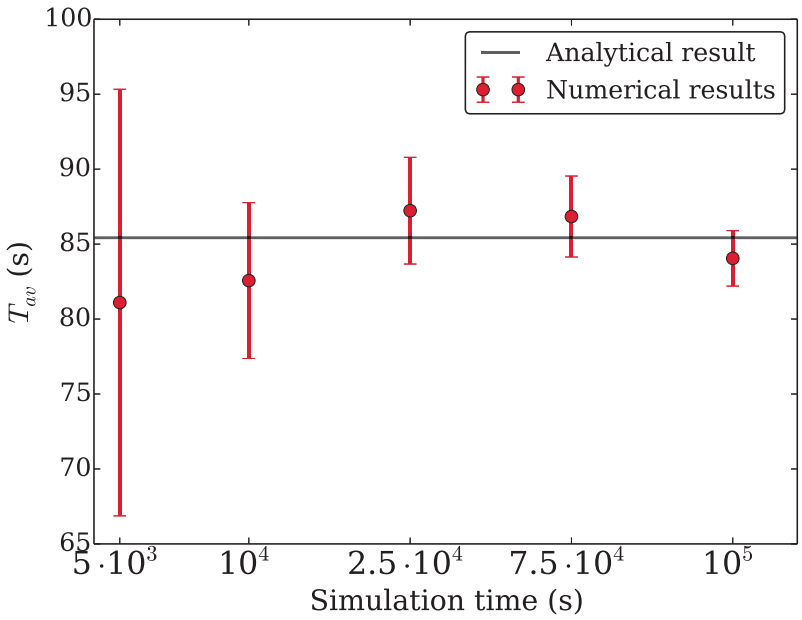

Figure 2.13.: Validation of the exact semi-Markovian algorithm devised in the main text by comparison to an analytical result obtained by solving the FPT problem for the tetrahedron model with $[IP_3] = 1\mu M$. The sample standard deviations of the algorithmic solutions were calculated by simulating 50 realisations for every total simulation time indicated on the x-axis.

Incorporating a global feedback for the puff dynamics can be done akin to the DSSA algorithm by memorizing the time of the last spike t_{sp} and introducing a inhomogeneous Poisson rate by $\lambda(\tau, t, t_{sp}) = \lambda_0 \ (1 - e^{-\xi(\tau+t-t_{sp})})$. The systems time t in this algorithm is only updated when a transition occurs, so that the total distance in time from the last spike event will be the actual jump epoch τ

plus the systems time t, holding the last $S_1 \to S_0$ transition time, minus the time of the last spike t_{sp}. The waiting time density for the first cluster opening then reads:

$$\begin{aligned}\Psi_{o,0}(\tau, t, t_{sp}) &= \lambda_0 \left(1 - e^{-\xi(\tau+t-t_{sp})}\right) e^{-\lambda_0 \int_0^\tau (1-e^{-\xi(\tau+t-t_{sp})}} \\ &= \lambda_0 \left(1 - e^{-\xi(\tau+t-t_{sp})}\right) e^{-\lambda_0 \tau} \; e^{\frac{-\lambda_0}{\xi} e^{-\xi(t-t_{sp})}(e^{-\xi\tau}-1)}.\end{aligned} \tag{2.42}$$

In summary an exact and cost-effective simulation algorithm was devised by extending the Gillespie algorithm with respect to the determination of the next jump epoch by non-exponential waiting time densities. It is generally applicable to all well defined semi-Markovian processes with discrete states.

2.5. Encoding Stimulus intensities in random spike trains

Having established a profound understanding about the intracellular Ca^{2+} spike generating process, the next question is how cells actually reliably encode extracellular stimulus intensities with these stochastic spike sequences. Earlier studies analyzed the theoretical information content of sequences originating from an inhomogeneous Poisson process [90, 103], and found that this information content is solely dependent on the slope of the σ-T_{av} relation. This slope is determined by a refractory global negative feedback as discussed in the preceding sections, and is a cell type specific robust property. However, given the huge cell-to-cell variability found for the characteristics of the individual spike sequences, e.g. for the average ISI, no direct and absolute relation between stimulus intensity and Ca^{2+} spiking could be established on a single cell level until recently. The pioneering idea that a fold change in the average ISI (T_{av}) reliably encodes stimulus intensity changes was first deduced from theoretical studies of the hierarchic Ca^{2+} spiking model, and then confirmed by extensive experimental studies [105]. Accordingly the theoretical considerations shall be presented first followed by a brief review of the experimental results.

2.5.1. Theoretical predictions

For all theoretical analysis of the intracellular Ca^{2+} spiking done in this work the Ca^{2+} signaling pathway is simplified by only considering processes which are downstream of the IP_3 formation. This means that processes involving the binding of the extracellular ligand to the G protein coupled cell surface receptors as well as the subsequent cleavage of membrane phospholipids to IP_3 are not explicitly considered in the model. This includes potentially important factors like surface receptor density or IP_3 activation. The mathematical Ca^{2+} model takes the concentration of active IP_3 directly as input, and treats different IP_3 concentration as different stimulus intensities. However, this simplification can be expected to be reasonable by making the rather weak assumption that the intracellular IP_3 concentration is a monotone function of the extracellular ligand concentration. An additional simplification applies to the structure of the ISIs. In real cellular Ca^{2+} spike sequences, the interspike intervals are comprised of

the spike duration, a physiological refractory period and the stochastic period. The former lead to a minimal ISI (T_{min}). For the mathematical description by a stochastic process, the deterministic T_{min} is neglected and only the stochastic period is considered. For low to intermediate stimulus intensities, this stochastic period constitutes the major component of the ISI [105].

To assess the relative impact of different stimulus intensities on the modeled Ca^{2+} spike sequences, the change of T_{av} for two different IP_3 concentrations, $\Delta T_{av} = T_{av1} - T_{av2}$, is analyzed. The values of T_{av} (IP_3) are calculated using the generic model and, similar to the calculations shown in figure 2.9, the coupling strength C_{14} is varied to mimic the cell-to-cell variability. As shown in figure 2.14 the relative change of the average ISI is a linear function of T_{av1}. This leads to a simple expression, termed the *encoding relation*, for the change of the average ISI by applying a stimulus step of size ΔIP_3:

$$\Delta T_{av} = \beta(\Delta IP_3)\ T_{av1}, \tag{2.43}$$

with β being the slope of the relations shown in figure 2.14.

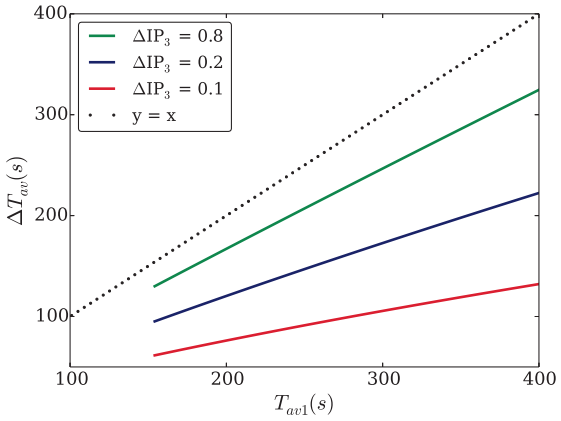

Figure 2.14.: Relation between the change of T_{av} (ΔT_{av}) and the value of the average ISI before the second stimulation (T_{av1}). Shown are analytical results for different stimulation steps with the stimulus intensity for T_{av1} being $[IP_3] = 0.5\mu M$. The functional relationship is clearly linear, which indicates a fold change response given by the slope of the depicted curves.

Rewriting equation 2.43 by expanding $\Delta T_{av} = T_{av1} - T_{av2}$ as

$$\beta = \frac{T_{av1} - T_{av2}}{T_{av1}} \tag{2.44}$$

shows that β can be defined as the fold change of T_{av} when applying a second stimulus which determines T_{av2}. The interpretation is that slower spiking cells of a population still remain slower after an increase of the stimulation and the same is true for the faster spiking ones. But the relative change of the average ISI is the same for all cells and is given by the fold change β. This means, that there

is no absolute value of T_{av} encoding a stimulus intensity, but cells do encode stimulus changes by a constant factor which is independent of the value of T_{av1} of a specific cell. This remarkably resembles Weber's law from sensory perception theory which originates from observations of the just-noticeable difference of physical stimuli for human observers [23].

Model calculations also allow to systematically compute the fold change $\beta(\Delta IP_3)$ in dependence on the stimulation step size by evaluating the r.h.s. of equation 2.44 for different values of $[IP_3]$. Results are depicted in figure 2.15 and show that the larger the stimulation step the larger the fold change. That the value of β is bounded by $0 < \beta < 1$ is obvious by noting that equation 2.44 can be written as $T_{av2} = T_{av1}(1 - \beta)$. The theory states that the actual course of the $\beta(\Delta IP_3)$ functions is dependent on the value of IP_3 for the first T_{av} . As to be seen in the following, this is not recovered experimentally.

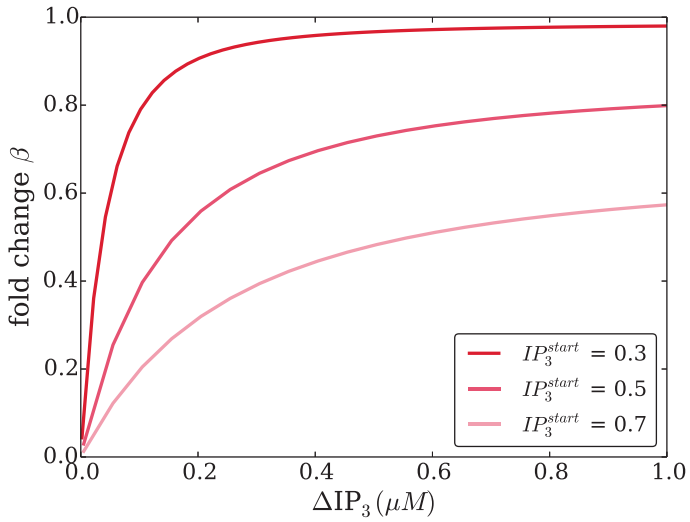

Figure 2.15.: Functional relationship between the fold change β and the stimulation step size ΔIP_3. The fold change generally grows with ΔIP_3 and is bounded by $0 < \beta < 1$. These result were obtained by evaluating the r.h.s. of equation 2.44 for different values of IP_3 . The needed average ISIs were calculated using the analytical solution of the tetrahedron Ca^{2+} model. Theory predicts, that the values of β are also dependent on the IP_3 -level for the first T_{av1}: IP_3^{start}.

The main prediction of the theoretical considerations presented here, is that absolute values of T_{av} are not informative on a single cell level about an external stimulus intensity. However, the relative change of the stimulus intensity, in the model captured by ΔIP_3 , is reliably encoded in the fold change β of the average ISI. This fold change is predicted to be the same for all cells and is therefore robust against the huge cell-to-cell variability in T_{av} . In the next section, the experimental effort and results to successfully confirm this prediction shall be presented.

2.5.2. Experiments supporting the fold change encoding hypothesis

Experimental stimulation of intracellular Ca^{2+} signaling can be achieved in human embryonic kidney (HEK) 293 cells by exposing the cells to carbachol (CCh). This binds to muscarinic acetylcholine cell surface receptors and activates the Ca^{2+} pathway leading to sustained Ca^{2+} spike sequences which can be recorded for up to one hour [105]. To test for the fold change experimentally a paired stimulation protocol was used, in which the HEK293 cells were stimulated with one concentration of CCh and afterwards were exposed to a higher concentration of CCh by switching the medium. This difference in the CCh concentration (Δ[CCh]) constitutes the stimulus step size experimentally. ISIs were recorded accordingly and the respective averages T_{av1} and T_{av2} were individually calculated for all cells. Plotting the results in the ΔT_{av} - T_{av1} plane consistently allowed for a linear fit with the encoding relation defined in equation 2.43 and β could be determined for different stimulation step sizes. In the results shown in figure 2.16 two different Δ[CCh] are shown, and the fold change β given by the slope indeed increases for larger steps in the CCh concentration as predicted from theory in the preceding subsection, i.e. represented in figure 2.14.

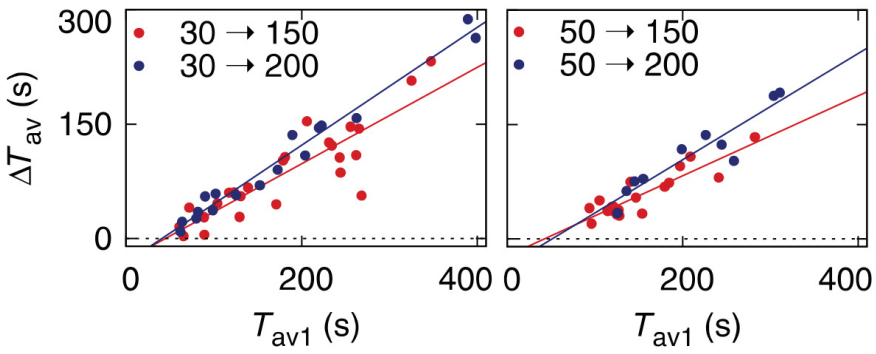

Figure 2.16.: Relation between the change of T_{av} (ΔT_{av}) and the value of the average ISI of the first stimulation (T_{av1}) for two paired stimulation experiments [105]. Shown are each two different stimulation steps with the indicated CCh concentrations in μM. The single dots represent the average ISI values for the spike trains of the single cells. A linear model according to the encoding relation $\Delta T_{av} = \beta T_{av1}$ was fitted to the data. The larger step sizes of 170 and 150 μM Cch respectively in blue lead to larger slopes compared to the smaller Δ[CCh] of 120 and 100 μM respectively shown in red. This confirms that the fold change β reliably encodes changes of stimulus intensities.

These results were further assured by repeating these experiments with another cell type. Sequentially stimulating hepatocytes with phenylephrine showed a similar linear relationship in the ΔT_{av} - T_{av1} plane. The goodness of the linear model expressing the fold changes was assessed by using Pearson's correlation coefficient and analysis of explained uncertainty. As shown in figure 2.17 these

analyses additionally confirmed the fold change hypothesis.

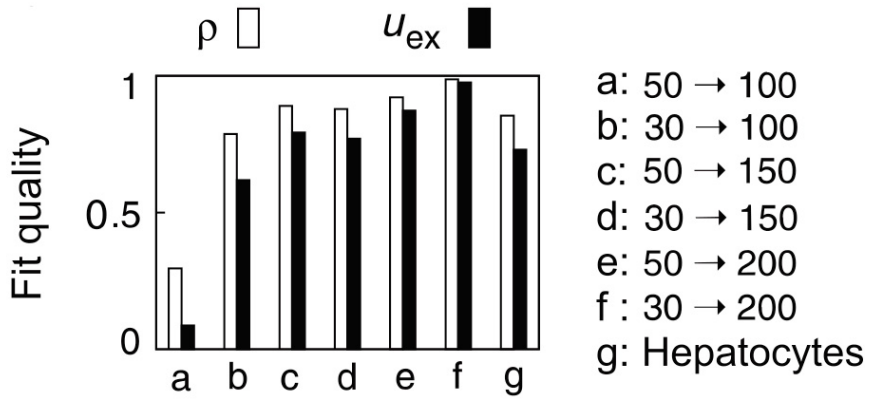

Figure 2.17.: Pearson's correlation coefficients (ρ) and explained uncertainties (u_{ex}) for the linear model $\Delta T_{av} = \beta T_{av1}$ constituting the fold change response. The stimulation steps in CCh concentration (μM) of the HEK293 cells are indicated on the right. The hepatocytes were stimulated with 0.6 μM and then 1.0 μM phenylephrine. As a value of 1 for both ρ and u_{ex} indicates a perfect linear correlation the fold change hypothesis is well confirmed for all but the smallest Δ[CCh].

These paired stimulation experiments with HEK293 cells lead to the observation, that the fold change β only depends on the step size Δ[CCh] and not the initial CCh concentration. This is shown in figure 2.18, where the measured values of β do not support for a dependence of the fold change on the initial CCh concentration. Writing the encoding relation equation 2.43 as a difference equation

$$T_{av}([\text{CCh}] + \Delta[\text{CCh}]) - T_{av}([\text{CCh}]) = -\beta(\Delta[\text{CCh}])T_{av}([\text{CCh}]), \tag{2.45}$$

and making a first order approximation of the fold change dependence on the stimulation step size according to

$$\beta(\Delta[\text{CCh}]) = \frac{\partial\beta}{\partial\Delta[\text{CCh}]}\,\Delta[\text{CCh}], \tag{2.46}$$

finally leads by taking the limit $\Delta[\text{CCh}] \to 0$ to the differential equation

$$\frac{dT_{av}}{d[\text{CCh}]} = -\gamma\, T_{av}, \quad \gamma = \left.\frac{\partial\beta}{\partial\Delta[\text{CCh}]}\right|_{\Delta[\text{CCh}]=0}. \tag{2.47}$$

The solution of this equation yields an exponential dependence of the average ISI on the CCh concentration:

$$T_{av} = e^{-\gamma([\text{CCh}] - [\text{CCh}]_{ref})}\, T_{av,ref}. \tag{2.48}$$

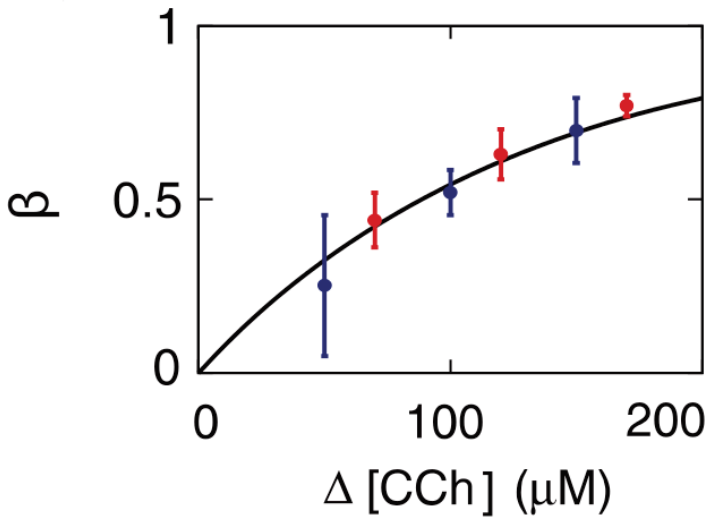

Figure 2.18.: Measured values of the fold change β of HEK293 cells for paired stimulation experiments with stimulation step sizes (Δ[CCh]) as indicated on the x-axis. The reference concentrations were $[\mathrm{CCh}]_{ref}$ = 30 μM (red) and $[\mathrm{CCh}]_{ref}$ = 50 (blue). The line shows the exponential relationship between the fold change and Δ[CCh] formulated in equation 2.49 in the main text.

The average ISI measured at a reference CCh concentration is given by $T_{av,ref}$, which also captures the differences between individual cells in the response to the reference stimulus $[\mathrm{CCh}]_{ref}$. The single parameter γ describes the sensitivity of $\mathrm{T_{av}}$ on the stimulus intensity. Reinserting this expression into the encoding relation shows that β obeys an exponential dependence on the stimulation step $\Delta[\mathrm{CCh}] = [\mathrm{CCh}] - [\mathrm{CCh}]_{ref}$:

$$\beta = 1 - e^{-\gamma \Delta[\mathrm{CCh}]}. \tag{2.49}$$

This relation can be reliably fitted to measured values of the fold change β as shown in figure 2.18. However, according to results from the mathematical Ca^{2+} model, depicted in figure 2.15, there is a dependence of the fold change on the reference CCh concentration. There is currently no straightforward explanation for this discrepancy. One source of it might be that the model neglects all processes of the Ca^{2+} pathway upstream to IP_3 and directly takes the IP_3 concentration as stimulus input.

By noting that γ according to the fold change hypothesis has to be the same for all cells in a population, equation 2.48 can be recast on the population level as

$$T_{pop} = e^{-\gamma([\mathrm{CCh}] - [\mathrm{CCh}]_{ref})}\, T_{pop,ref}. \tag{2.50}$$

Here T_{pop} and $T_{pop,ref}$ are the population averages of $\mathrm{T_{av}}$ and $T_{av,ref}$ respectively. The universality of the exponential concentration-response of T_{pop} could be strikingly verified not only by the measured data used for the derivation, but

also for published data for hepatocytes [81] and insect salivary glands [76]. In each case shown in figure 2.19 the effects of the stimulus intensity on T_{pop} were well described by equation 2.50.

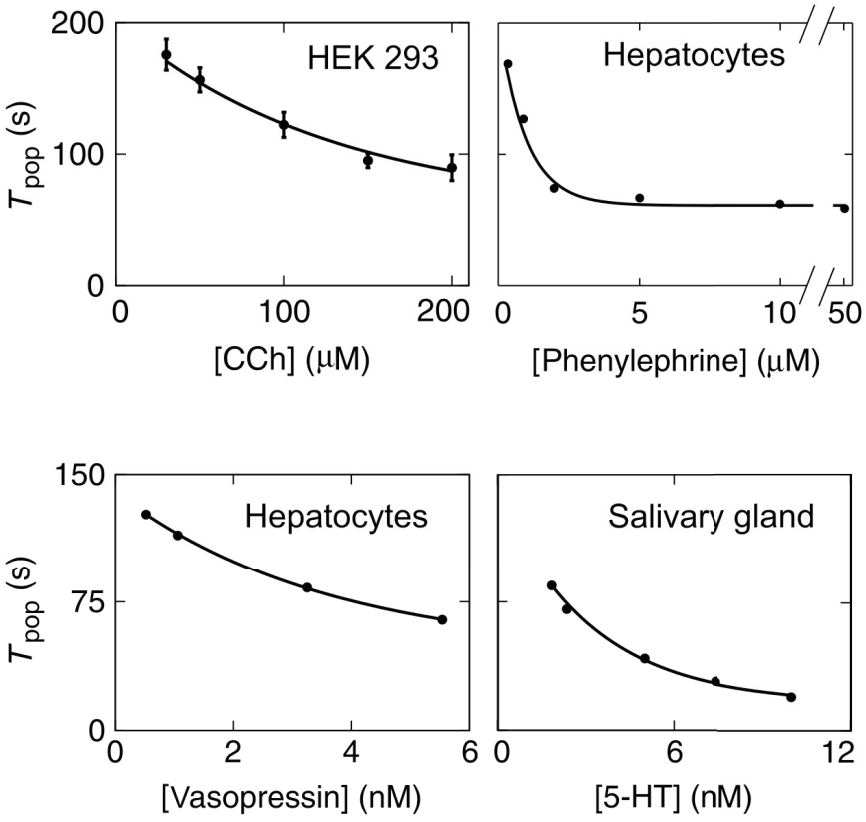

Figure 2.19.: Applying the exponential stimulus concentration-response derived in the main text to different measured data sets. The HEK293 data was actually used for the derivation, the other data sets have long been published. Hepatocytes were stimulated with either phenylephrine or vasopressin [81], the population averages of the average ISIs (T_{pop}= <T_{av} >) nicely follow the exponential relationship on the ligand concentration. The same is true for data from insect salivary glands stimulated with 5-HT [76].

The experimental evidence gathered to support the fold change hypothesis is compelling. It showed that there is a constant fraction β by what individual cells change their T_{av} according to a stimulus step size, and this measured relation between T_{av1} and T_{av2} is well described by the encoding relation first deduced from theory. Although the dependence of β on the initial stimulus intensity was not recovered experimentally, this observation in turn lead to a phenomenological derivation of the concentration-response which strikingly and universally explains the average ISI for different cell types and stimuli.

2.6. Discussion of the stochastic Ca^{2+} modeling

The initial goal of the investigations presented here was to progress the efforts made by the Falcke group to adequately model intracellular Ca^{2+} signaling. Most notably, this included the extension and deepening of the mathematical concepts employed in ref. [103]. The established theoretical and experimental findings of the Falcke group revealed the immanent stochasticity of the Ca^{2+} spike trains and identified the ISI distribution as the key descriptor of the single cell Ca^{2+} signals [90]. Exploiting spatial symmetries, stationary Ca^{2+} diffusion profiles ([101]) and results from fluorescence microscopy of single puff sites ([104]) lead to the stochastic tetrahedron Ca^{2+} model described in ref. [103].

From this perspective, which is the starting point for the main analytical result derived in this work, the interspike interval is given by the first passage time to go from the state of all Ca^{2+} release sites (the IP_3R clusters) closed to the state where all release sites are open. To incorporate information from single Ca^{2+} channel dynamics into the full model but to avoid a state space explosion the concept of hierarchic stochastic modeling was introduced already in ref. [103]. It relies on partitioning the huge microscopic state space into functional or observable states. This is nothing new, but by employing non-exponential waiting times for the transitions between these functional states as opposed to assigning simple rates, not all information from the microscopic dynamics is lost. In section 2.2.2 this concept was embedded in the mathematical theory of semi-Markov processes where the conditioned waiting times Ψ_{ij} were rigorously defined. The correspondent Master equation is comprised of a probability flux balance, similar to the discretized continuity equation in physics, and the fluxes are given by a recursive integral equation containing the non-exponential waiting times [79]. Combining this non-Markovian Master equation with the renewal approach ([107]) lead to a convenient analytical solution in Laplace space of the first passage time problem (section 2.2.3). The possibility to compute arbitrary moments of the FPT distribution without the need for the often cumbersome back-transformation from Laplace space accounts for the high practical value of this solution. Its application to the tetrahedron Ca^{2+} model was straightforward and analytical results for the first four moments of the FPT distribution in dependence on cellular parameters were calculated in section 2.2.5. The values of the moments, in particular the $\sigma \approx T_{av}$ relation, indicate an exponential ISI distribution for physiological parameter values.

This result was, taken into account the complex semi-Markovian modeling framework, a bit puzzling. However, it could be eventually explained by noting the time scale separation between the isolated puff events, described by the exponential waiting time Ψ_{01}, and the subsequent cluster openings described by non-exponential waiting times. Loosely speaking, the puff events get filtered by the very fast subsequent cluster dynamics, and the average fraction of puffs successfully culminating to a spike without touching the ground state is given by the splitting probability C_{14}. This is exactly the Poisson splitting ansatz employed for the generic Ca^{2+} model of section 2.3. Poisson splitting states that given a Poisson process with some rate $\lambda(t)$ and its arrivals are accepted with a probability p the new process is also a Poisson process with rate $p\lambda(t)$. From

that perspective it is quite evident that an exponential puff waiting time, with constant λ_0, will result in an exponential ISI distribution when splitted with probability C_{14}. Hence, incorporating a global negative feedback on the puff rate, assuring that $\lambda_0(t) = 0$, will result in a non-exponential ISI distribution. These are found experimentally and are characterized by a σ-T_{av} relation with a slope smaller than one [90]. In the model, the feedback strength ξ is given by the recovery rate of the puff rate. However, the detailed molecular mechanism constituting this predicted global feedback still remains elusive. In summary, the exploitation of the time-scale separation both explains the performance of thetetrahedron model without feedback and allows for the generic model, which analytically reproduces the experimental findings with much less effort. The crucial splitting probability C_{14} couples the local puff dynamics to the spatial cluster arrangement which in combination determine the Ca^{2+} spiking process. It also conveniently allows to introduce cell-to-cell variability, e.g. of cluster coupling strength, into the model. For this work, the dependence of C_{14} on cellular parameters like stimulus strength was adopted from the tetrahedron model. Other parameterizations or inhomogeneous puff sites, i.e. multiple $\lambda_{i,o}$'s, offer plausible extensions of this general approach. The validity of the generic model was confirmed analytically (section 2.3.3) and numerically (section 2.4.1).

Having characterized the stochastic process exhibited by the tetrahedron model as semi-Markovian, a faster and more general applicable Monte Carlo simulation algorithm than the one used in ref. [103] was devised in section 2.4.2. It is an extension of the famous Gillespie algorithm ([37]) and therefore does not rely on a time discretization which makes it both exact and cost effective. There have been, except for this work, no applications of semi-Markov processes to cell biology so far, at least to the authors knowledge. However, they are known for a long time and in the context of machine learning and hidden semi-Markov processes have been successfully applied to various areas, such as speech recognition or human activity prediction [115]. As the HSM modeling scheme naturally leads to a semi-Markovian description, there might be further applications to stochastic cellular processes where a state space reduction is inevitable for feasible modeling. For example, to describe stochastic gene expression a standard Markovian description bears the risk of oversimplification which could be attenuated by a semi-Markovian approach.

In the last section 2.5 the predictive power of the presented Ca^{2+} signaling modeling approach could be demonstrated. Calculations of the cellular response characterized by the average ISIs with respect to two different stimuli, predicted a fold change encoding of stimulus intensity changes. This paradigm explains very consistent how a cell population with large cell-to-cell variability in spiking patterns coherently reacts to a changing extracellular signal. Strikingly, this behavior could be recently established experimentally in close collaboration with the Taylor lab [105]. The experimental data allowed for a more phenomenological description of the cellular response towards extracellular stimuli. The deduced exponential relationship between T_{av} and the stimulus concentration proved also to be applicable to different cell and stimulus types. It relies on the independence of the fold change value β from the reference stimulus intensity. This is not captured by the Ca^{2+} modeling so far, and closing this gap demands further

theoretical efforts.

As Ca^{2+} serves as a versatile messenger molecule, the bigger question of course is how the adaptive stochastic spike sequences get decoded to ultimately change the cellular state, e.g. altering the expression profile or changing the functional state of enzymes, in a coordinated manner. There have been numerous studies on the downstream effects of intracellular calcium [9], a prominent example concerns the transcription factor NFAT which is important for an effective immune response [48]. It gets activated by the phosphatase calcineurin which activity in turn is calcium dependent. As calcium signals were predominantly viewed as oscillatory, many decoding models involve frequency decoding [69, 84], which is naturally unsuitable for stochastic signals. Other decoding models rely on signal integrators [18], but these are inconsistent with the large cell-to-cell variability of T_{av} . In summary, elaborating a coherent decoding model incorporating the stochastic nature of the Ca^{2+} signals as well as the fold change encoding of stimulus intensities is a challenging but essential task for the future.

3. Concluding remarks

Every model, irrespective of its elaborateness, should prove itself by reasonable predictions. Subsequent experiments based on theoretical predictions which successfully establish new findings are challenging and rare, especially in molecular biology. Nevertheless, this often proved to be a very effective and insightful way of doing science. With respect to the studies presented here, it could be achieved in the field of Ca^{2+} signaling in a concerted effort by the Falcke group and the experimentalists from the Taylor lab [105]. For p53, corresponding new successful experiments are still lacking. Although, the theoretical analysis conducted in this work provides advice for the focus of new experiments. Despite all differences between the p53 and the Ca^{2+} signaling systems, the versatility of the possible downstream effects of both pathways is astonishing. If there is an evolutionary design principle of cellular signaling systems, to steadily augment the inputs, the information content and the scope of an already established signaling pathway, is open to speculation. Subsequent theoretical and experimental studies should and will reveal more details on cellular signal processing. Furthermore, positive feedbacks play a central role in both systems. As these generally have the potential to decouple signal strength from stimulus strength, it appears plausible to expect that they are a common design principle of cellular signaling pathways. Finally, elaborate single cell experiments formed the basis for all investigations presented here. They opened the door for a much deeper understanding of intracellular processes, and will continue to challenge and enlighten theoretical and experimental cell biologists in the future.

A. Appendix p53

A.1. Peak detection with wavelets

Most real life data is noisy, which generally limits the efficiency of feature extraction from the data. Especially peak detection is difficult when the noise amplitude is high, as the number of missed peaks (false negatives) and erroneously detected peaks (false positives) can easily spoil the results. A standard strategy to deal with noisy data is to apply some form of smoothing. This naturally will either reduce false negative detections (under-smoothing) or false positive detections (over-smoothing). It is generally impossible to achieve both desirable properties at the same time with a standard smoothing approach, which typically works by convoluting the data with some window (or sometimes called filter) function. The wavelet transform, however, has the favorable property of smoothing the data on many scales at once. This, as to be seen in the following, allows for a peak detection algorithm which is capable of optimizing both the false negative and the false positive detection rate.

Wavelets were originally developed for signal processing, to allow for a good resolution in both time and frequency domain. They are extensively used for the spectral analysis of times series in various fields, they are especially popular in the geosciences [50]. The continuous wavelet transform is formally defined as:

$$W_\Phi(t,s)[f] = \frac{1}{\sqrt{s}} \int_{-\infty}^{+\infty} \Phi^*\Big(\frac{t-\tau}{s}\Big) f(t) d\tau \tag{A.1}$$

Here $f(t)$ is the signal and the $\Phi_{s,\tau}(t)$ are the *wavelets*. The resulting wavelet spectrum $W_\Phi(t,s)$ is a two-dimensional time-frequency representation of the original signal, where s denotes the scale and t the time. Wavelets are a family of functions which can be used to construct a basis for the Hilbert space $L^2(\mathbb{R})$. An important property of wavelets is, that they have "finite energy" or as a corollary are square-integrable. Loosely speaking, this property stems from their time-localization (see example in figure A.1). This is for example not true for the basis functions of the Fourier transform. Another important property concerns the vanishing mean $\int_{-\infty}^{+\infty} \Phi_{s,\tau}(t) dt = 0$. A specific wavelet basis function can be derived from a *mother wavelet* by two operations, dilation (s) and translation (τ), so that one may write $\Phi_{s,\tau}(t) = \frac{1}{\sqrt{s}} \Phi\Big(\frac{t-\tau}{s}\Big)$. An example for such a mother wavelet is the Ricker wavelet which reads

$$\Phi(t) = \frac{2}{\sqrt{3}\pi^{\frac{1}{4}}} \left(1 - t^2\right) e^{-\frac{t^2}{2}}. \tag{A.2}$$

It is the negative second derivative of the Gaussian function. By substituting $t \to \frac{t-\tau}{s}$ the whole family $\Phi_{s,\tau}$ of Ricker wavelets can be derived from that

equation.

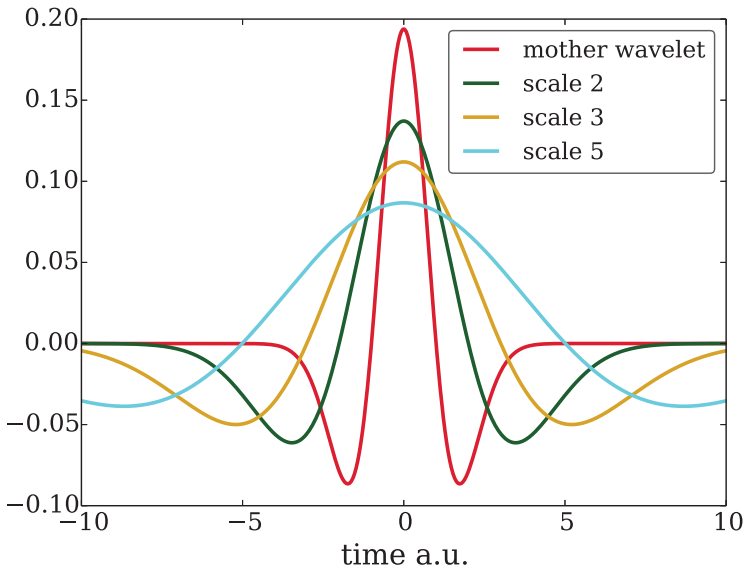

Figure A.1.: The Ricker wavelet for $\tau = 0$ and the scale parameter s as indicated in the legend, the mother wavelet corresponds to $s = 1$.

To illustrate the peak detection algorithm, a synthetic trajectory is constructed out of a slow sinusoidal signal plus additive white Gaussian noise. Then, two Gaussian peaks are added, one narrow on top of a sinusoidal arc and one wider at the bottom. The test trajectory is shown below in figure A.2.

Visualizations of wavelet transforms are called scaleograms and are easy to comprehend by noting that for a fixed scale s, equation A.1 constitutes the convolution (i.e. an unnormalized cross-correlation) of the signal $f(t)$ with the wavelet function of scale s. Therefore, the scaleogram can be interpreted as stacked convolutions with increasing scale over some range from s_{min} to s_{max}. A value of the spectrum at a point (t, s) corresponds to the unnormalized correlation of the signal with the wavelet of scale s centered at t. Two horizontal slices, meaning two selected convolutions, of the wavelet transform are shown in figure A.3b.

The scale range $[s_{min}, s_{max}]$ is very critical for the scaleogram. Wavelets with the smallest scale determine the widths of the narrowest peaks which can still be detected. Wavelets with larger scales are very good noise filters, but if too big start to capture global trends of the trajectory. Hence, wavelets have a *bandpass* character. To illustrate this, two scaleograms of the synthetic trajectory with ill-chosen scale ranges are shown in figure A.4.

To progress with the peak detection so called *ridges* are identified in the scaleogram. A ridge is the vertical connection of relative maxima within the stacked convolutions. This strategy was originally devised in the context of feature detection in mass spectra [24]. An important parameter for the ridge line construction controls the maximal acceptable horizontal distance (i.e. the

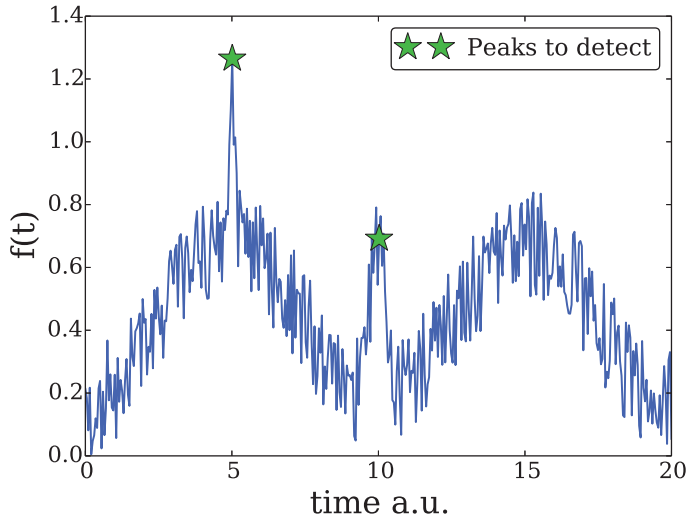

Figure A.2.: The synthetic test trajectory. White noise was added to a slow sinusoidal background signal. Then, the two peaks to detect are placed at times 5 and 10 respectively. They are scaled Gaussians with standard deviation $\sigma = 0.1$ and $\sigma = 0.5$. Its wavelet transform is shown in figure A.3a.

time-lag) of two relative extrema coming from adjacent convolutions to get connected. Unsymmetric peaks, for example, will generally show a tilted ridge line in the scaleogram, corresponding to a drift in time of the relative extrema for increasing scales. Loosely speaking, a ridge line is a vertical, but not necessarily straight, slice through the scaleogram. To give a real life example, the output of the peak detection algorithm devised for the p53 data analysis is shown in figure A.5.

The final step of the peak detection is to filter the constructed ridge lines. This is an intricate process, as there are no *a priori* perfect filter criteria available. A powerful criteria is obviously the maximum value of a ridge line, as it is effectively an amplitude filter. Also the length of a ridge line, as it is an indicator of the vertical extent of a feature in the scaleogram, can be very informative. Random fluctuations usually have, if any, very short ridge lines. Howver, the performance of the filter criteria are not independent on the scale range $[s_{min}, s_{max}]$ and obviously not on the ridge line construction . So for an application to real data, many sensible adjustments depending on, among others, peak shapes, noise level and sampling frequency have to be made.

The ridge line representation of a peak in the scaleogram is the core idea behind the peak detection method presented here. It allows to assess a features significance over many (smoothing) scales at once, and therefore allows a more robust detection performance for highly irregular data. In conclusion, peak detection with wavelets is incredibly versatile, but on the downside also more difficult to master.

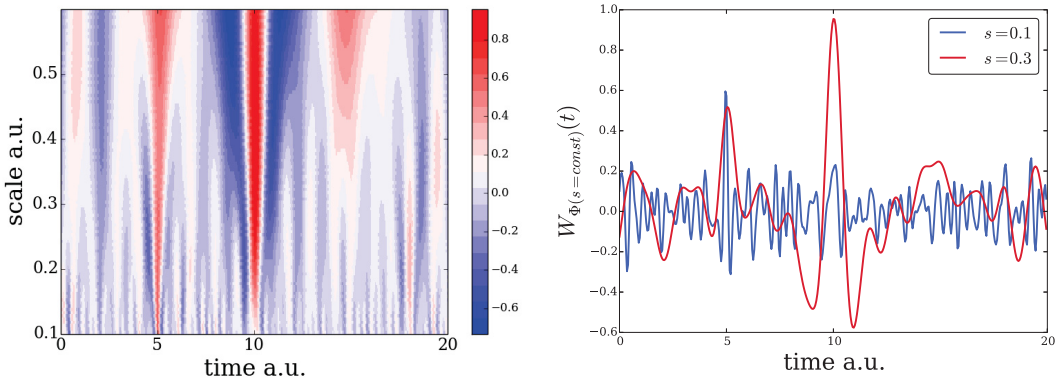

(a) (b)

Figure A.3.: (a) The wavelet transform, or scaleogram, of the test trajectory shown in figure A.2. The scale range used for the Ricker wavelets goes from $s_{min} = 0.1$ to $s_{max} = 0.6$. Positive correlation is indicated in red, negative correlation in blue. The two noticeable stripes of positive correlation are the wavelet representation of the peaks to detect in the trajectory. (b) Two horizontal slices through the scaleogram in (a). These correspond to two convolutions of the signal with the Ricker wavelet for two different scales as indicated in the legend. Wavelets with larger scales naturally smooth the data more, but have problems to distinguish the sinusoidal background from the narrow peaks. Smaller scales capture also narrow features, but are more prone to noise.

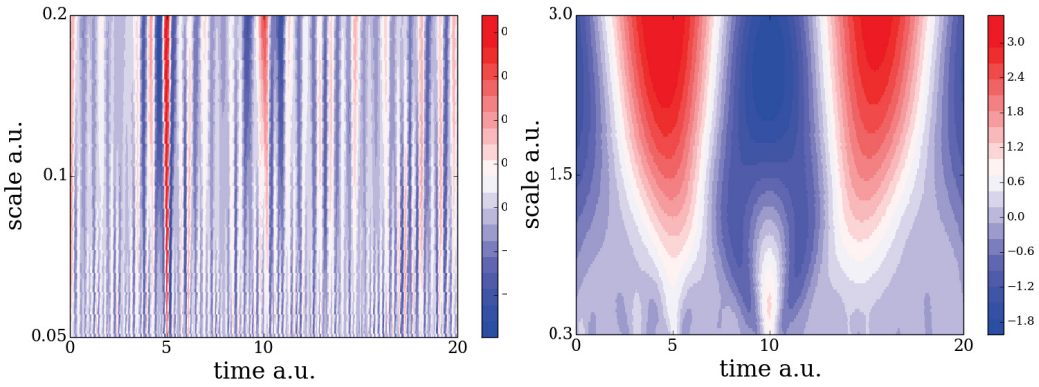

(a) (b)

Figure A.4.: Wavelet transforms of the synthetic trajectory shown in figure A.2 with ill-chosen scale ranges $[s_{min}, s_{max}]$ (a) Scaleogram with the scale range [0.05,0.2], the noise is not effectively filtered out. (b) Scaleogram with the scale range [0.2,3.], the noise is almost completely suppressed but the global sinusoidal background signal dominates the scaleogram.

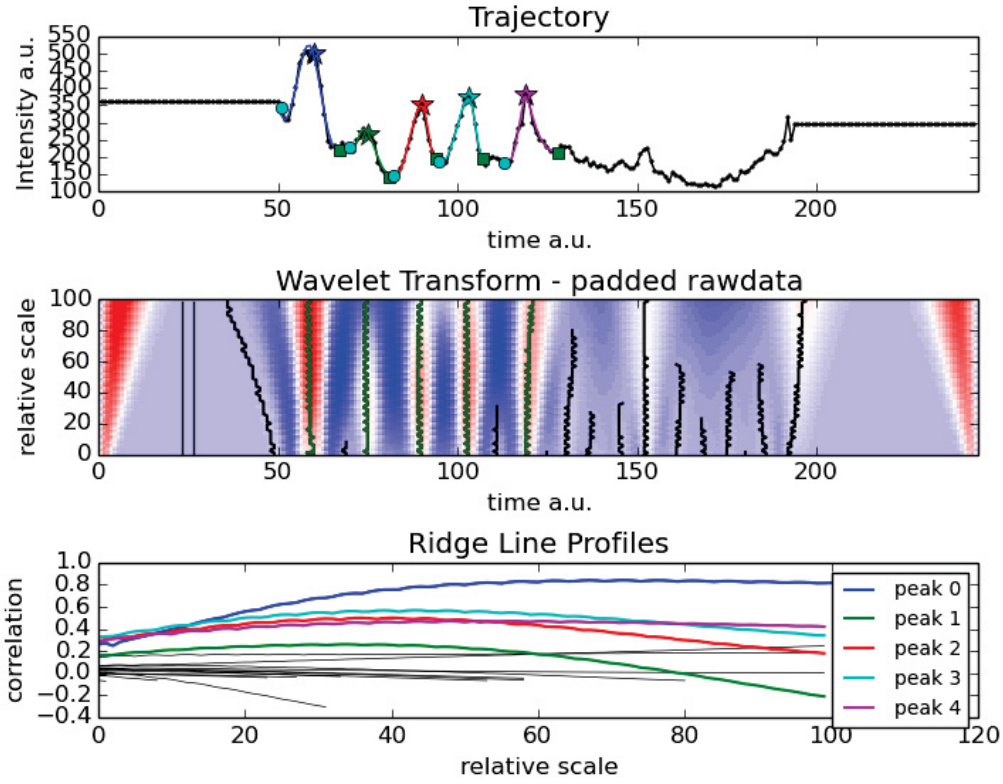

Figure A.5.: Example output of the peak detection program devised for the p53 data analysis. The first plot shows the padded trajectory with the color coded detected peaks, it is from a cell stimulated with 100ng NCS (see main text). In the middle the corresponding wavelet transform (scaleogram) together with the successfully constructed ridge lines is shown. The wavelet scale is given in relative units with $s_{min} \equiv 0$ and $s_{max} \equiv 100$. The last plot at the bottom depicts all identified ridge lines, which color correspond to the color coded detected peaks in the trajectory. Ridge lines in black were filtered out. Optimally, a ridge line is a concave function of the wavelet scale, with a maximum corresponding to the highest correlation at a scale associated with the respective peak width. The employed filter criteria for the ridge lines are a minimum correlation of 0.2 and a minimum length of 100, which corresponds to the total scale range. The absolute scale range was $s_{min} = 2h$ and $s_{max} = 7h$.

A.2. Table of Parameters for the p53 model

All parameters used for the excitable p53 model and their values used for the simulations.

Table A.1.: Overview of all model parameters

name	meaning	value
A	maximal self activation rate of ATM	30.5
P	rate of dephosphorylation of ATM by $Wip1$	22
S	rate of ATM^* formation induced by DSB loci, damage signal strength	$0 < \mathrm{S} < 0.4$
γ	sensitivity parameter for the logarithmic transform $S(DSB) = \gamma\ ln(DSB + 1)$	0.06
C	production rate of $p53$	1.4
g	maximal degradation of $P53$ by $Mdm2$	2.5
d_{AM}	degradation rate of $Mdm2$ by ATM^*	1.
T_m	maximal production rate of $mdm2$	1.
T_M	maximal production rate of $Mdm2$	4.
T_w	maximal production rate of $wip1$	1.
T_W	maximal production rate of $Wip1$	1.
d_A	basal dephosphorylation rate of ATM^*	0.16
d_P	basal degradation rate of $P53$	0.1
d_m	basal degradation rate of $mdm2$	1.
d_M	basal degradation rate of $Mdm2$	2.
d_w	basal degradation rate of $wip1$	1.3.
d_W	basal degradation rate of $Wip1$	2.3
k_A	Michaelis constant for the ATM^* self activation	0.5
k_{WA}	Michaelis constant for the inhibition of the ATM^* self activation by $Wip1$	0.14
k_{MP}	Michaelis constant for the degradation of $P53$ by $Mdm2$	0.15
k_{Pm}	Michaelis constant for the production of $mdm2$ by $P53$	1.
k_{Pw}	Michaelis constant for the production of $wip1$ by $P53$	1.
R	strength of the inhibition of the $Mdm2$ mediated degradation of $P53$ by ATM^*	2

For better readability the model equations again read:

$$\frac{d}{dt}ATM^* = A\frac{ATM^{*2}}{k_A + ATM^{*2}}\frac{1}{1 + Wip1/k_{WA}} - d_A ATM^* - P\ ATM^*\ Wip1 + S(DSB)$$

$$\frac{d}{dt}P53 = C - d_P\ P53 - \ g\ Mdm2\ \frac{P53}{k_{MP} + P53}\left(1 + \frac{R}{1 + ATM^*}\right)$$

$$\frac{d}{dt}mdm2 = T_m\frac{P53}{k_{Pm} + P53} - d_m\ mdm2$$

$$\frac{d}{dt}Mdm2 = T_M\ mdm2 - d_M\ Mdm2 - d_{AM}\ ATM^*\ Mdm2$$

$$\frac{d}{dt}wip1 = T_w\frac{P53}{k_{Pw} + P53} - d_w\ wip1$$

$$\frac{d}{dt}Wip1 = T_W\ wip1 - d_W\ Wip1$$

A.3. Sensitivity of pulse shapes and the excitation threshold on parameter variations

Here numerical studies about the influence of the model parameters on the amplitude and the length of the pulses shall be presented. Additionally the excitation threshold shall be quantified, and its parameter dependence analysed. In general the parameter plots shown in the following are qualitatively the same for parameters of the same bifurcation type as introduced in section 1.5.2 of the main text and shown as table below. So there are again four plots sufficient to qualitatively characterize the parameter dependencies of the model.

Table A.2.: Overview of the bifurcation diagram type membership for all model parameters

	type I	**type II**	**type III**	**type IV**
Parameters	C, d_m, d_M d_{AM}, k_{mp}	g, T_m, T_M R	P, T_w, T_W	A, d_w, d_W k_{WA}, k_{Pw}
Trait	positive on $P53$	negative on P53	negative on ATM^*	positive on ATM^*

For performing the pulse shape analysis, the system is initialized at the lowest stable steady state plus a little initial kick in positive ATM^* direction to cross the excitation threshold. The parameter regions scanned always reach from half up to twice the respective default value. It is noteworthy, that the region of excitability is bigger than the region characterized by one stable and two unstable fixed points. The phasespace still *feels* the existence of the unstable fixed points which disappeared via a saddle-node bifurcation. Therefore, these plots also directly indicate the total parameter region of excitability. This additional region of excitable behavior in parameter space is marked by black dots in the following plots.

The results for the amplitudes and pulse lengths shown in figures A.6 and A.7 indicate that different parameters show a varying degree of influence on the p53 pulse amplitudes. Although the qualitative pulse shape dependencies are the same for all parameters belonging to the same type, the effects may significantly differ in quantity. By analysing all parameters like described and shown above, their impact on the pulse shapes was classified as either strong or weak. Table A.3 gives a general overview of the sensitivity for the main model parameters.

To test the model parameter influence on the excitation threshold, all species are initialized at the stable steady state, except for ATM which is taken out of an interval $[0, ATM^*_{max}]$. For each set of the initial conditions the resulting trajectory is tested for an excitation loop. This procedure is repeated to scan through the same range of parameter values as before and the minimal necessary ATM^* value for triggering a pulse is recored respectively. The results are shown

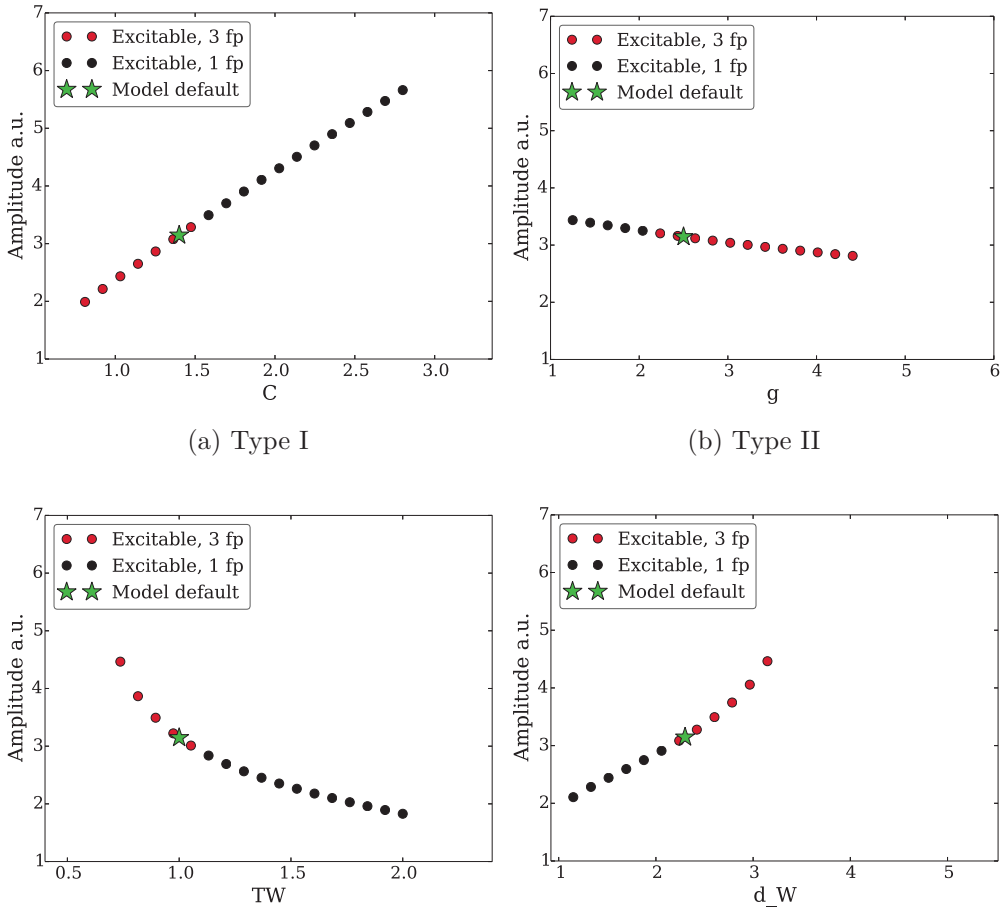

(a) Type I

(b) Type II

(c) Type III

(d) Type IV

Figure A.6.: Model parameter influence on p53 pulse amplitudes. The shown dependencies are qualitatively the same for parameters belonging to the same type according to table A.2.

in figure A.8, black dotes again depict the enlarged region of excitability without three fixes points.

The slope of the threshold dependence can generally be inferred from the codimension-2 bifurcation sets shown in the subsequent section.

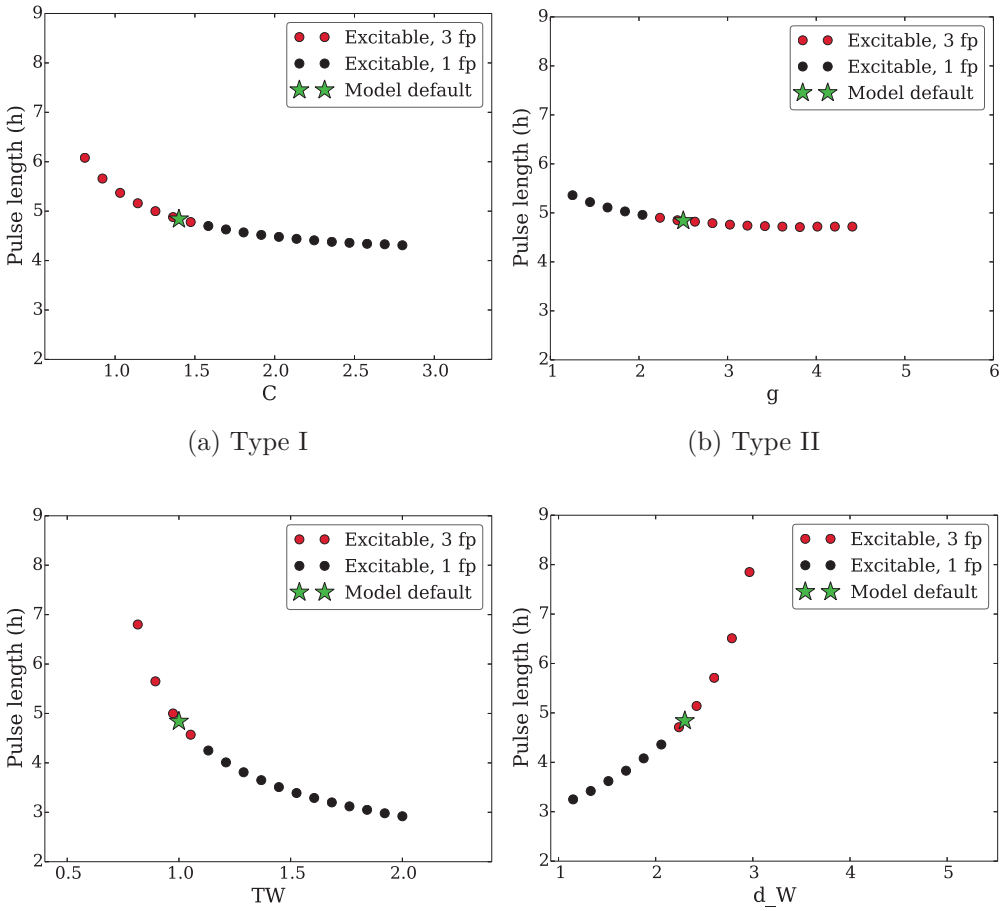

(a) Type I

(b) Type II

(c) Type III

(d) Type IV

Figure A.7.: Model parameter influence on p53 pulse length. The shown dependencies are qualitatively the same for parameters belonging to the same type according to table A.2.

Table A.3.: Overview of the impact of parameter variations with respect to p53 pulse shapes for the main model parameters

parameter	**amplitude**	**length**
A	strong	strong
P	strong	strong
C	strong	weak
g	weak	weak
d_{AM}	weak	weak
T_m	weak	weak
T_M	weak	weak
T_w	strong	strong
T_W	strong	strong
d_M	weak	weak
d_W	strong	strong
d_P	strong	weak
R	weak	weak
S	weak	weak

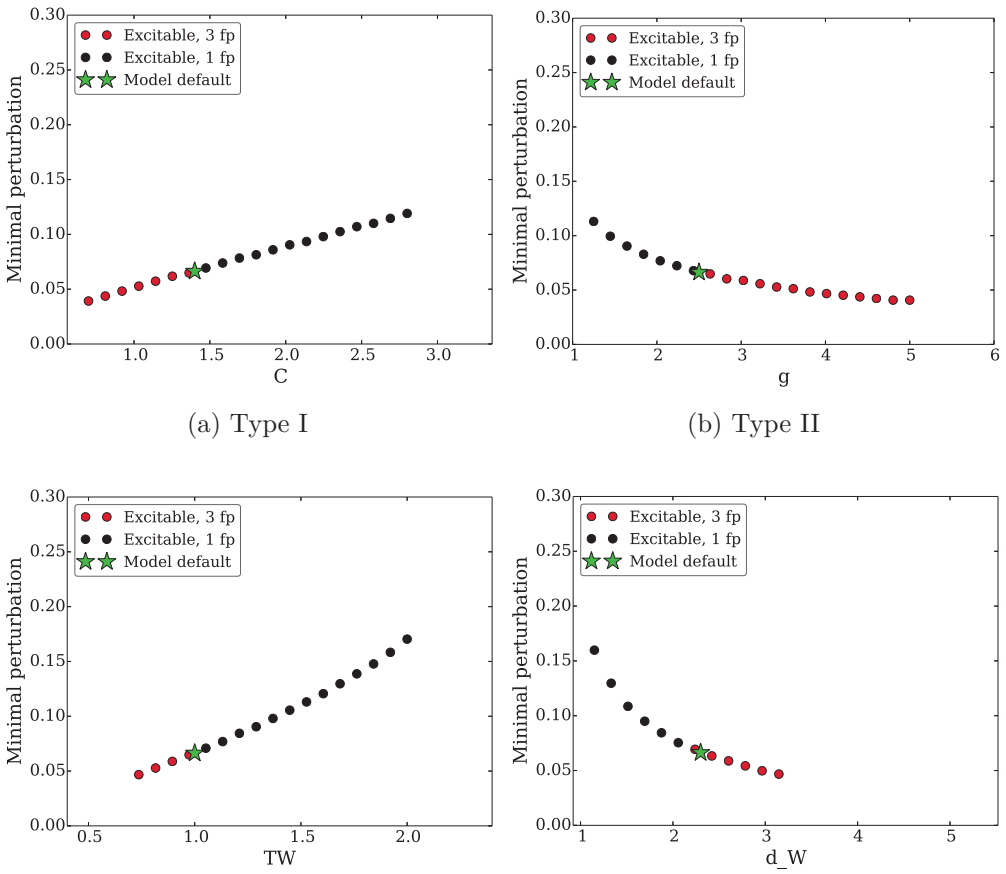

(a) Type I

(b) Type II

(c) Type III

(d) Type IV

Figure A.8.: Selected parameter influence on the excitation threshold. The shown dependencies are qualitatively the same for parameters belonging to the same type according to table A.2.

A.4. Codimension-2 bifurcation diagrams

An effective way to depict the model regimes and parameter dependencies are bifurcation set which trace the saddle-node curves and the Hopf-curve. The excitable regime always spreads from the Cusp point, denoted by 'CP1' in the plots, in between the two saddle-node curves. It is additionally confined by the Hopf-curve which crosses one of the two saddle-node curves, see also figure 1.31 in the main text.

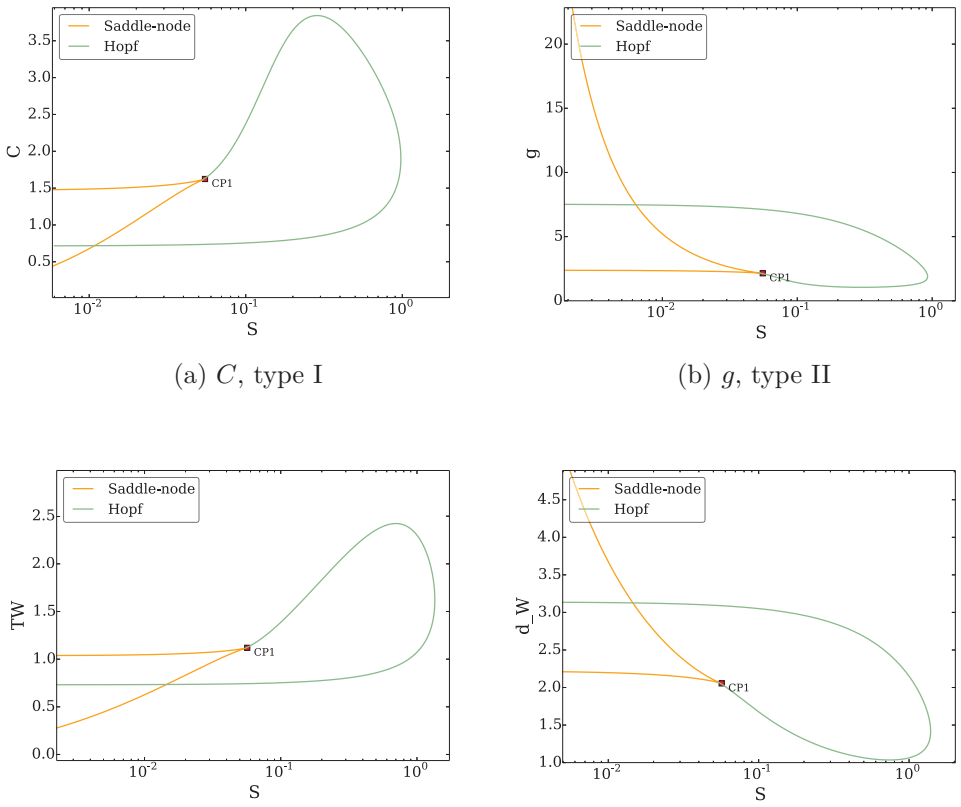

(a) C, type I

(b) g, type II

(c) T_W, type III

(d) d_W, type IV

Figure A.9.: Bifurcation sets for different p53 model parameters. The region of excitability always spreads from the Cusp point in between the two saddle-node curves, see also figure 1.31 in the main text. For better visibility of the excitable region a logarithmic scale for the signal strength S was chosen here.

A.5. Period of oscillations in the p53 model

As outlined in the main text, the period of the limit cycle appearing in the p53 model tends to infinity at the homoclinic bifurcation point. However, in practice the period dependence of the limit cycle on the bifurcation parameter is very steep. As shown in figure A.10, the period changes only very little over most of the parameter range.

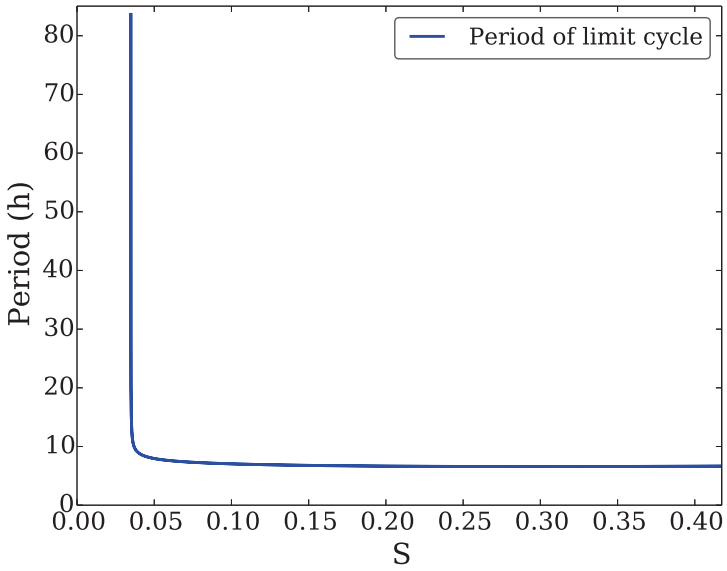

Figure A.10.: Period of the limit cycle oscillations in dependence on the bifurcation parameter S. Over most of the parameter range, the period changes very little. Only very close to the homoclinic bifurcation point, it grows rapidly and tends to infinity.

B. Appendix Ca^{2+}

B.1. Laplace transformations of Ψ_o and Ψ_c

The generalized exponential (GE) distribution is a generalized form of the human mortality distribution discovered by Gompertz and Verhulst in the first half of the 19th century [39, 42]. For the analytic solution of the first passage time problem formulated in the main text, the Laplace transformation of the GE density function and its survival function are needed. They constitute the non-exponential waiting times used for the opening transitions of the tetrahedron model.

The GE density itself reads

$$\Psi_o(t) = \alpha\lambda\ (1 - e^{-\lambda t})^{\alpha-1}\ e^{-\lambda t}. \tag{B.1}$$

The Laplace transformation of a function $f(t)$ is defined by

$$\mathcal{L}\{f\}(s) = \int_0^\infty f(t)\ e^{-st} dt, \tag{B.2}$$

and so the following integral needs to be solved:

$$\mathcal{L}\{\Psi_o\}(s) = \int_0^\infty \alpha\lambda\ (1 - e^{-\lambda t})^{\alpha-1}\ e^{-\lambda t}\ e^{-st} dt. \tag{B.3}$$

Substituting $y = e^{-t}$ gives

$$\alpha\lambda \int_0^1 (1 - y^\lambda)^{\alpha-1}\ y^{\lambda+s-1} dy. \tag{B.4}$$

Next the substitution $x = y^\lambda$ is applied:

$$\alpha \int_0^1 (1 - x)^{\alpha-1}\ x^{\frac{s}{\lambda}} dx. \tag{B.5}$$

Now the definition of the beta function is used, a special function already studied by Euler. Written as an integral, it reads:

$$B(k, l) = \int_0^1 (1 - x)^{k-1}\ x^{l-1} dx. \tag{B.6}$$

There is also a form involving the Euler Γ-function:

$$B(k, l) = \frac{\Gamma(k)\Gamma(l)}{\Gamma(k + l)}. \tag{B.7}$$

By using $l = \frac{s}{\lambda} + 1$ and substituting $k = \alpha$, one obtains from Eq. B.5:

$$\mathcal{L}\{\Psi_o\}(s) = \frac{\alpha\Gamma(\alpha)\Gamma(\frac{s}{\lambda}+1)}{\Gamma(\alpha+\frac{s}{\lambda}+1)}. \tag{B.8}$$

The Laplace transformation for the survival function

$$\bar{\Psi}_o(t) = 1 - (1 - e^{-\lambda t})^{\alpha} \tag{B.9}$$

can be done analogically. This time the following integral needs to be solved:

$$\mathcal{L}\{\bar{\Psi}_o\}(s) = \frac{1}{s} - \int_0^{\infty} (1 - e^{-\lambda t})^{\alpha} dt, \tag{B.10}$$

where the trivial Laplace transformation of a constant was already used. Substituting $y = e^{-t}$ followed by the second substitution $x = y^{\lambda}$ yields

$$\frac{1}{s} - \frac{1}{\lambda}\int_0^1 (1-x)^{\alpha}\ x^{\frac{s}{\lambda}-1} dx. \tag{B.11}$$

Now the the beta function (Eq. B.7) is recalled and a final substitution $l = \frac{s}{\lambda}$ gives the solution:

$$\mathcal{L}\{\bar{\Psi}_o\}(s) = \frac{1}{s} - \frac{\Gamma(\alpha+1)\Gamma(\frac{s}{\lambda})}{\lambda\Gamma(\alpha+\frac{s}{\lambda}+1)}, \tag{B.12}$$

where $k = \alpha + 1$.

The powers of $\bar{\Psi}_o$ needed for the construction of the conditioned waiting times can be written as

$$\bar{\Psi}_o^n = \sum_{k=0}^{\mathrm{n}} \binom{n}{k} (-1)^k (1 - e^{-\lambda t})^{k\alpha}. \tag{B.13}$$

These are just sums of the original terms with a rescaled shape parameter $k\alpha$, and therefore their Laplace transforms are sums of the accordingly rescaled results given above in Eq. B.12.

For the purposes of hierarchic stochastic modelling, the Laplace transform of the closing waiting time is also required. By using the binomial theorem, one may rewrite Ψ_c as:

$$\Psi_c(t) = \mathrm{N_{ch}}\gamma e^{-\gamma t} \sum_{k=0}^{\mathrm{N_{ch}}-1} \binom{\mathrm{N_{ch}}-1}{k} (-1)^k e^{-k\gamma t}, \tag{B.14}$$

where $1^{\mathrm{N_{ch}}-1-k} = 1$ was dropped inside the sum. After multiplication one gets:

$$\Psi_c(t) = \mathrm{N_{ch}}\gamma \sum_{k=0}^{\mathrm{N_{ch}}-1} \binom{\mathrm{N_{ch}}-1}{k} (-1)^k e^{-(k+1)\gamma t}. \tag{B.15}$$

In the end just the Laplace transform of a sum of exponentials is needed, and

one finally obtains:

$$\tilde{\Psi}_c(s) = \mathrm{N_{ch}}\gamma \sum_{k=0}^{\mathrm{N_{ch}}-1} \binom{\mathrm{N_{ch}}-1}{k} (-1)^k \frac{(-1)^k}{s+(k+1)\gamma}. \tag{B.16}$$

This form of the Laplace transformed closing time can be used for construction of the conditioned waiting times, which are needed for computation of the Ca^{2+} spiking statistics by Eq. 2.34 of the main text.

C. List of abbreviations

FP	fixed point
r.h.s.	right hand side
ATM	ataxia telangiectasia mutated
DSB	DNA double strand break
DDR	DNA damage response
IPI	inter pulse interval
ODE	ordinary differential equation
NCS	neocarzinostatin
LCO	limit cycle oscillator
TF	transcription factor
l.h.s.	left hand side
Wm	Wortmannin
ISI	inter spike interval
T_{av}	average ISI
HSM	hierarchic stochastic modelling
GE	generalized exponential
CV	coefficient of variation
HEK	human embryonic kidney 293 cells
CCh	carbachol

Bibliography

[1] U. Alon. Network motifs: theory and experimental approaches. *Nature Reviews Genetics*, 8(6):450–461, 2007.

[2] I. Amit, A. Citri, T. Shay, Y. Lu, M. Katz, F. Zhang, G. Tarcic, D. Siwak, J. Lahad, J. Jacob-Hirsch, et al. A module of negative feedback regulators defines growth factor signaling. *Nature genetics*, 39(4):503–512, 2007.

[3] S. J. Baker, E. R. Fearon, J. M. Nigro, A. Preisinger, J. Jessup, D. Ledbetter, D. Barker, Y. Nakamura, R. White, B. Vogelstein, et al. Chromosome 17 deletions and p53 gene mutations in colorectal carcinomas. *Science*, 244(4901):217–221, 1989.

[4] C. J. Bakkenist and M. B. Kastan. Dna damage activates atm through intermolecular autophosphorylation and dimer dissociation. *Nature*, 421 (6922):499–506, 2003.

[5] R. L. Bar-Or, R. Maya, L. A. Segel, U. Alon, A. J. Levine, and M. Oren. Generation of oscillations by the p53-mdm2 feedback loop: a theoretical and experimental study. *Proceedings of the National Academy of Sciences*, 97(21):11250–11255, 2000.

[6] E. Batchelor, C. S. Mock, I. Bhan, A. Loewer, and G. Lahav. Recurrent initiation: a mechanism for triggering p53 pulses in response to dna damage. *Molecular cell*, 30(3):277–289, 2008.

[7] E. Batchelor, A. Loewer, C. Mock, and G. Lahav. Stimulus-dependent dynamics of p53 in single cells. *Molecular systems biology*, 7(1), 2011.

[8] A. Becskei and L. Serrano. Engineering stability in gene networks by autoregulation. *Nature*, 405(6786):590–593, 2000.

[9] M. J. Berridge, P. Lipp, and M. D. Bootman. The versatility and universality of calcium signalling. *Nat Rev Mol Cell Biol*, 1(1):11–21, 2000.

[10] I. Bezprozvanny, J. Watras, and B. E. Ehrlich. Bell-shaped calcium-response curves of ins(1,4,5)p3- and calcium-gated channels from endoplasmic reticulum of cerebellum. *Nature*, 351(6329):751–4, 1991.

[11] L. Bintu, N. E. Buchler, H. G. Garcia, U. Gerland, T. Hwa, J. Kondev, T. Kuhlman, and R. Phillips. Transcriptional regulation by the numbers: applications. *Current opinion in genetics & development*, 15(2):125–135, 2005.

[12] N. E. Buchler, U. Gerland, and T. Hwa. Nonlinear protein degradation and the function of genetic circuits. *Proceedings of the National Academy of Sciences of the United States of America*, 102(27):9559–9564, 2005.

[13] D. V. Bulavin, O. N. Demidov, S. Saito, P. Kauraniemi, C. Phillips, S. A. Amundson, C. Ambrosino, G. Sauter, A. R. Nebreda, C. W. Anderson, et al. Amplification of ppm1d in human tumors abrogates p53 tumor-suppressor activity. *Nature genetics*, 31(2):210–215, 2002.

[14] M. Choi, J. Shi, S. H. Jung, X. Chen, and K.-H. Cho. Attractor landscape analysis reveals feedback loops in the p53 network that control the cellular response to dna damage. *Science signaling*, 5(251):ra83, 2012.

[15] A. Ciliberto, B. Novák, and J. J. Tyson. Steady states and oscillations in the p53/mdm2 network. *Cell cycle*, 4(3):488–493, 2005.

[16] E. Cinlar. Markov renewal theory: A survay. *Management Science*, 21, 1975.

[17] B. L. Clarke. *Stability of complex reaction networks*. Wiley Online Library, 1980.

[18] M. Colella, F. Grisan, V. Robert, J. D. Turner, A. P. Thomas, and T. Pozzan. Ca2+ oscillation frequency decoding in cardiac cell hypertrophy: role of calcineurin/nfat as ca2+ signal integrators. *Proceedings of the National Academy of Sciences*, 105(8):2859–2864, 2008.

[19] A. S. Coutts, C. J. Adams, and N. B. La Thangue. p53 ubiquitination by mdm2: a never ending tail? *DNA repair*, 8(4):483–490, 2009.

[20] D. Cox. *Renewal Theory*. Methuen & Co, 1970.

[21] P. Crespo, N. Xu, W. F. Simonds, and J. S. Gutkind. Ras-dependent activation of map kinase pathway mediated by g-protein $\beta\gamma$ subunits. 1994.

[22] G. W. De Young and J. Keizer. A single-pool inositol 1,4,5-trisphosphate-receptor-based model for agonist-stimulated oscillations in Ca^{2+} concentration. *Proc Natl Acad Sci U S A*, 89(20):9895–9, 1992.

[23] S. Dehaene. The neural basis of the weber–fechner law: a logarithmic mental number line. *Trends in cognitive sciences*, 7(4):145–147, 2003.

[24] P. Du, W. A. Kibbe, and S. M. Lin. Improved peak detection in mass spectrum by incorporating continuous wavelet transform-based pattern matching. *Bioinformatics*, 22(17):2059–2065, 2006.

[25] G. Dupont, S. Swillens, C. Clair, T. Tordjmann, and L. Combettes. Hierarchical organisation of calcium signals in hepatocytes: from experiments to models. *Biochim.Biophys.Acta*, 1498:134–152, 2000.

[26] G. Dupont, A. Abou-Lovergne, and L. Combettes. Stochastic aspects of oscillatory Ca^{2+} dynamics in hepatocytes. *Biophys J*, 95(5):2193–202, 2008.

[27] A. Dupré, L. Boyer-Chatenet, and J. Gautier. Two-step activation of atm by dna and the mre11–rad50–nbs1 complex. *Nature structural & molecular biology*, 13(5):451–457, 2006.

[28] A. Efeyan and M. Serrano. p53: guardian of the genome and policeman of the oncogenes. *Cell Cycle*, 6(9):1006, 2007.

[29] M. B. Elowitz, A. J. Levine, E. D. Siggia, and P. S. Swain. Stochastic gene expression in a single cell. *Science*, 297(5584):1183–6, 2002.

[30] M. Falcke. Reading the patterns in living cells - the physics of Ca^{2+} signaling. *Adv Phys*, 53(3), 2004.

[31] M. Falk, E. Lukasova, B. Gabrielova, V. Ondrej, and S. Kozubek. Chromatin dynamics during dsb repair. *Biochimica et Biophysica Acta*, 1773 (10):1534–1545, 2007.

[32] M. Fiscella, H. Zhang, S. Fan, K. Sakaguchi, S. Shen, W. E. Mercer, G. F. V. Woude, P. M. O'Connor, and E. Appella. Wip1, a novel human protein phosphatase that is induced in response to ionizing radiation in a p53-dependent manner. *Proceedings of the National Academy of Sciences*, 94(12):6048–6053, 1997.

[33] R. FitzHugh. *Mathematical models of excitation and propagation in nerve*. Publisher Unknown, 1966.

[34] N. Geva-Zatorsky, N. Rosenfeld, S. Itzkovitz, R. Milo, A. Sigal, E. Dekel, T. Yarnitzky, Y. Liron, P. Polak, G. Lahav, et al. Oscillations and variability in the p53 system. *Molecular systems biology*, 2(1), 2006.

[35] N. Geva-Zatorsky, E. Dekel, E. Batchelor, G. Lahav, and U. Alon. Fourier analysis and systems identification of the p53 feedback loop. *Proceedings of the National Academy of Sciences*, 107(30):13550–13555, 2010.

[36] D. T. Gillespie. Exact stochastic simulation of coupled chemical reactions. *J Phys Chem*, 81:2340–2361, 1977.

[37] D. T. Gillespie. *Markov processes: An introduction for physical scientists*. Elsevier, 1991.

[38] A. Goldbeter et al. Biochemical oscillations and cellular rhythms. *Biochemical Oscillations and Cellular Rhythms, by Albert Goldbeter, Foreword by MJ Berridge, Cambridge, UK: Cambridge University Press, 1997*, 1, 1997.

[39] B. Gompertz. On the nature of the function expressive of the law of human mortality, and on a new mode of determining the value of life contingencies. *Phil Trans Royal Soc*, 115, 1825.

[40] B. C. Goodwin. Oscillatory behavior in enzymatic control processes. *Advances in enzyme regulation*, 3:425–437, 1965.

[41] R. D. Gupta and D. Kundu. Closeness of gamma and generalized exponential distribution. *Communications in statistics-theory and methods*, 32 (4):705–721, 2003.

[42] R. D. Gupta and D. Kundu. Generalized exponential distribution: Existing results and some recent developments. *J Statist Plann Inference*, 137(11), 2007.

[43] J. W. Harper and S. J. Elledge. The dna damage response: ten years after. *Molecular cell*, 28(5):739–745, 2007.

[44] S. Hastings, J. Tyson, and D. Webster. Existence of periodic solutions for negative feedback cellular control systems. *Journal of Differential Equations*, 25(1):39–64, 1977.

[45] Y. Haupt, R. Maya, A. Kazaz, M. Oren, et al. Mdm2 promotes the rapid degradation of p53. *Nature*, 387(6630):296–299, 1997.

[46] E. R. Higgins, H. Schmidle, and M. Falcke. Waiting time distributions for clusters of ip3 receptors. *J Theor Biol*, 259(2):338–349, 2009.

[47] A. L. Hodgkin and A. F. Huxley. A quantitative description of membrane current and its application to conduction and excitation in nerve. *The Journal of physiology*, 117(4):500, 1952.

[48] P. G. Hogan, L. Chen, J. Nardone, and A. Rao. Transcriptional regulation by calcium, calcineurin, and nfat. *Genes & development*, 17(18):2205–2232, 2003.

[49] F. C. Hoppensteadt and E. M. Izhikevich. *Weakly connected neural networks*, volume 126. Springer New York, 1997.

[50] S. Jevrejeva, J. Moore, and A. Grinsted. Influence of the arctic oscillation and el niño-southern oscillation (enso) on ice conditions in the baltic sea: The wavelet approach. *Journal of Geophysical Research: Atmospheres (1984–2012)*, 108(D21), 2003.

[51] K. Karanam, R. Kafri, A. Loewer, and G. Lahav. Quantitative live cell imaging reveals a gradual shift between dna repair mechanisms and a maximal use of hr in mid s phase. *Molecular cell*, 47(2):320–329, 2012.

[52] M. B. Kastan, O. Onyekwere, D. Sidransky, B. Vogelstein, and R. W. Craig. Participation of p53 protein in the cellular response to dna damage. *Cancer research*, 51(23 Part 1):6304–6311, 1991.

[53] K. K. Khanna and S. P. Jackson. Dna double-strand breaks: signaling, repair and the cancer connection. *Nature genetics*, 27(3):247–254, 2001.

[54] S. Krishna, S. Semsey, and M. H. Jensen. Frustrated bistability as a means to engineer oscillations in biological systems. *Physical biology*, 6(3):036009, 2009.

[55] J.-P. Kruse and W. Gu. Modes of p53 regulation. *Cell*, 137(4):609–622, 2009.

[56] Y. A. Kuznetsov. *Elements of applied bifurcation theory*. Springer New York, 1995.

[57] G. Lahav, N. Rosenfeld, A. Sigal, N. Geva-Zatorsky, A. J. Levine, M. B. Elowitz, and U. Alon. Dynamics of the p53-mdm2 feedback loop in individual cells. *Nature genetics*, 36(2):147–150, 2004.

[58] D. P. Lane. Cancer. p53, guardian of the genome. *Nature*, 358(6381): 15–16, 1992.

[59] M. F. Lavin. Ataxia-telangiectasia: from a rare disorder to a paradigm for cell signalling and cancer. *Nature reviews Molecular cell biology*, 9(10): 759–769, 2008.

[60] J.-H. Lee and T. T. Paull. Atm activation by dna double-strand breaks through the mre11-rad50-nbs1 complex. *Science*, 308(5721):551–554, 2005.

[61] H. Leonhardt, M. A. Zaks, M. Falcke, and L. Schimansky-Geier. Stochastic hierarchical systems: Excitable dynamics. *Journal of biological physics*, 34(5):521–538, 2008.

[62] A. Loewer, E. Batchelor, G. Gaglia, and G. Lahav. Basal dynamics of p53 reveal transcriptionally attenuated pulses in cycling cells. *Cell*, 142 (1):89–100, 2010.

[63] A. Loewer, K. Karanam, C. Mock, and G. Lahav. The p53 response in single cells is linearly correlated to the number of dna breaks without a distinct threshold. *BMC biology*, 11(1):114, 2013.

[64] X. Lu. Tied up in loops: positive and negative autoregulation of p53. *Cold Spring Harbor perspectives in biology*, 2(5):a000984, 2010.

[65] L. Ma, J. Wagner, J. J. Rice, W. Hu, A. J. Levine, and G. A. Stolovitzky. A plausible model for the digital response of p53 to dna damage. *Proceedings of the National Academy of Sciences of the United States of America*, 102 (40):14266–14271, 2005.

[66] J. Mallet-Paret and H. L. Smith. The poincaré-bendixson theorem for monotone cyclic feedback systems. *Journal of Dynamics and Differential Equations*, 2(4):367–421, 1990.

[67] J. S. Marchant and I. Parker. Role of elementary ca2+ puffs in generating repetitive ca2+ oscillations. *EMBO J*, 20(1&2):65–76, 2001.

[68] J. S. Marchant, N. Callamaras, and I. Parker. Initiation of IP_3-mediated Ca^{2+} waves in xenopus oocytes. *EMBO J*, 18(19):5285–5299, 1999.

[69] M. Marhl, M. Perc, and S. Schuster. A minimal model for decoding of time-limited ca2+ oscillations. *Biophys Chem*, 120(3):161–7, 2006.

[70] R. Maya, M. Balass, S.-T. Kim, D. Shkedy, J.-F. M. Leal, O. Shifman, M. Moas, T. Buschmann, Z. Ronai, Y. Shiloh, et al. Atm-dependent phosphorylation of mdm2 on serine 395: role in p53 activation by dna damage. *Genes & development*, 15(9):1067–1077, 2001.

[71] R. Milo, S. Shen-Orr, S. Itzkovitz, N. Kashtan, D. Chklovskii, and U. Alon. Network motifs: simple building blocks of complex networks. *Science*, 298 (5594):824–827, 2002.

[72] G. Moenke, M. Falcke, and K. Thurley. Hierarchic stochastic modelling applied to intracellular ca2+ signals. *PloS one*, 7(12):e51178, 2012.

[73] C. B. Muratov and E. Vanden-Eijnden. Noise-induced mixed-mode oscillations in a relaxation oscillator near the onset of a limit cycle. *Chaos: An Interdisciplinary Journal of Nonlinear Science*, 18(1):015111, 2008.

[74] E. Oancea and T. Meyer. Protein kinase c as a molecular machine for decoding calcium and diacylglycerol signals. *Cell*, 95(3):307–18, 1998.

[75] T. G. Oliver, E. Meylan, G. P. Chang, W. Xue, J. R. Burke, T. J. Humpton, D. Hubbard, A. Bhutkar, and T. Jacks. Caspase-2-mediated cleavage of mdm2 creates a p53-induced positive feedback loop. *Molecular cell*, 43(1): 57–71, 2011.

[76] M. J. B. P. E. Rapp. The control of transepithelial potential oscillations in the salivary gland of calliphora erythrocephala. *J. Exp. Biol.*, 93:119–132, 1981.

[77] J. Piette, H. Neel, and V. Maréchal. Mdm2: keeping p53 under control. *Oncogene*, 15(9), 1997.

[78] S. Pigolotti, S. Krishna, and M. H. Jensen. Oscillation patterns in negative feedback loops. *Proceedings of the National Academy of Sciences*, 104(16): 6533–6537, 2007.

[79] T. Prager, M. Falcke, L. Schimansky-Geier, and M. A. Zaks. Non-markovian approach to globally coupled excitable systems. *Phys Rev E*, 76(1):011118, 2007.

[80] T. Riley, E. Sontag, P. Chen, and A. Levine. Transcriptional control of human p53-regulated genes. *Nature reviews Molecular cell biology*, 9(5): 402–412, 2008.

[81] T. A. Rooney, E. J. Sass, and A. P. Thomas. Characterization of cytosolic calcium oscillations induced by phenylephrine and vasopressin in single fura-2-loaded hepatocytes. *J Biol Chem*, 264(29):17131–41, 1989.

[82] A. Sancar, L. A. Lindsey-Boltz, K. Ünsal-Kaçmaz, and S. Linn. Molecular mechanisms of mammalian dna repair and the dna damage checkpoints. *Annual review of biochemistry*, 73(1):39–85, 2004.

[83] R. Schlicht and G. Winkler. A delay stochastic process with applications in molecular biology. *J Math Biol*, 57:613–648, 2008.

[84] S. Schuster, M. Marhl, and T. Hofer. Modelling of simple and complex calcium oscillations. from single-cell responses to intercellular signalling. *Eur J Biochem*, 269(5):1333–55, 2002.

[85] B. Schwanhäusser, D. Busse, N. Li, G. Dittmar, J. Schuchhardt, J. Wolf, W. Chen, and M. Selbach. Global quantification of mammalian gene expression control. *Nature*, 473(7347):337–342, 2011.

[86] Y. Shiloh and Y. Ziv. The atm protein kinase: regulating the cellular response to genotoxic stress, and more. *Nature Reviews Molecular Cell Biology*, 14(4):197–210, 2013.

[87] S. Shreeram, O. N. Demidov, W. K. Hee, H. Yamaguchi, N. Onishi, C. Kek, O. N. Timofeev, C. Dudgeon, A. J. Fornace, C. W. Anderson, et al. Wip1 phosphatase modulates atm-dependent signaling pathways. *Molecular cell*, 23(5):757–764, 2006.

[88] A. Sigal, R. Milo, A. Cohen, N. Geva-Zatorsky, Y. Klein, Y. Liron, N. Rosenfeld, T. Danon, N. Perzov, and U. Alon. Variability and memory of protein levels in human cells. *Nature*, 444(7119):643–6, 2006.

[89] A. Skupin and M. Falcke. From puffs to global ca2+ signals: how molecular properties shape global signals. *Chaos*, 19(3):037111, 2009.

[90] A. Skupin, H. Kettenmann, U. Winkler, M. Wartenberg, H. Sauer, S. C. Tovey, C. W. Taylor, and M. Falcke. How does intracellular Ca^{2+} oscillate: by chance or by the clock? *Biophys J*, 94(6):2404–11, 2008.

[91] I. F. Smith and I. Parker. Imaging the quantal substructure of single ip3r channel activity during Ca^{2+} puffs in intact mammalian cells. *Proc Natl Acad Sci U S A*, 106(15):6404–9, 2009.

[92] P. Smolen, D. A. Baxter, and J. H. Byrne. Modeling transcriptional control in gene networks—methods, recent results, and future directions. *Bulletin of mathematical biology*, 62(2):247–292, 2000.

[93] J. Sneyd and M. Falcke. Models of the inositol trisphosphate receptor. *Prog Biophys Mol Biol*, 89(3):207–45, 2005.

[94] E. D. Sontag. Molecular systems biology and control. *European journal of control*, 11(4):396–435, 2005.

[95] S. L. Spencer, S. Gaudet, J. G. Albeck, J. M. Burke, and P. K. Sorger. Non-genetic origins of cell-to-cell variability in trail-induced apoptosis. *Nature*, 459(7245):428–432, 2009.

[96] J. M. Stommel and G. M. Wahl. Accelerated mdm2 auto-degradation induced by dna-damage kinases is required for p53 activation. *The EMBO journal*, 23(7):1547–1556, 2004.

[97] T. Sun and J. Cui. A plausible model for bimodal p53 switch in dna damage response. *FEBS letters*, 588(5):815–821, 2014.

[98] R. Taufiq Ur, A. Skupin, M. Falcke, and C. W. Taylor. Clustering of insp3 receptors by insp3 retunes their regulation by insp3 and Ca^{2+} . *Nature.*, 458(7238):655–9, 2009.

[99] C. W. Taylor and S. C. Tovey. Ip3 receptors: Toward understanding their activation. *Cold Spring Harb Perspect Biol*, 2(12):a004010, 2010.

[100] A. Theodosiou and A. Ashworth. Map kinase phosphatases. *Genome Biol*, 3(7):1–10, 2002.

[101] R. Thul and M. Falcke. Release currents of ip(3) receptor channel clusters and concentration profiles. *Biophys. J.*, 86(5):2660–73, 2004.

[102] R. Thul, K. Thurley, and M. Falcke. Toward a predictive model of Ca^{2+} puffs. *Chaos*, 19(3):037108, 2009.

[103] K. Thurley and M. Falcke. Derivation of Ca^{2+} signals from puff properties reveals that pathway function is robust against cell variability but sensitive for control. *Proc Natl Acad Sci U S A*, 108:427–32, 2011.

[104] K. Thurley, I. F. Smith, S. C. Tovey, C. W. Taylor, I. Parker, and M. Falcke. Timescales of ip(3)-evoked ca(2+) spikes emerge from ca(2+) puffs only at the cellular level. *Biophys J*, 101(11):2638–44, 2011.

[105] K. Thurley, S. C. Tovey, G. Moenke, V. L. Prince, A. Meena, A. P. Thomas, A. Skupin, C. W. Taylor, and M. Falcke. Reliable encoding of stimulus intensities within random sequences of intracellular ca2+ spikes. *Science signaling*, 7(331):ra59–ra59, 2014.

[106] J. J. Tyson, K. C. Chen, and B. Novak. Sniffers, buzzers, toggles and blinkers: dynamics of regulatory and signaling pathways in the cell. *Current opinion in cell biology*, 15(2):221–231, 2003.

[107] N. G. Van Kampen. *Stochastic Processes in Physics and Chemistry*. Elsevier Science B.V., Amsterdam, 2002.

[108] B. Vogelstein, D. Lane, and A. J. Levine. Surfing the p53 network. *Nature*, 408(6810):307–310, 2000.

[109] B. Wang, S. Matsuoka, P. B. Carpenter, and S. J. Elledge. 53bp1, a mediator of the dna damage checkpoint. *Science*, 298(5597):1435–1438, 2002.

[110] K. Wegner, A. Bachmann, J.-U. Schad, P. Lucarelli, S. Sahle, P. Nickel, C. Meyer, U. Klingmüller, S. Dooley, and U. Kummer. Dynamics and feedback loops in the transforming growth factor< i> β</i> signaling pathway. *Biophysical chemistry*, 162:22–34, 2012.

[111] P. O. Westermark, D. K. Welsh, H. Okamura, and H. Herzel. Quantification of circadian rhythms in single cells. *PLoS computational biology*, 5(11): e1000580, 2009.

[112] T. Wilhelm. The smallest chemical reaction system with bistability. *BMC systems biology*, 3(1):90, 2009.

[113] I. Wolfram Research. Mathematica 8.0. 2010.

[114] H. Yamaguchi, S. R. Durell, D. K. Chatterjee, C. W. Anderson, and E. Appella. The wip1 phosphatase ppm1d dephosphorylates sq/tq motifs in checkpoint substrates phosphorylated by pi3k-like kinases. *Biochemistry*, 46(44):12594–12603, 2007.

[115] S.-Z. Yu. Hidden semi-markov models. *Artificial Intelligence*, 174(2): 215–243, 2010.

Acknowledgments

Many people contributed, on one way or the other, to the process of creating this scholarly piece of work.

Dr. Martin Falcke is a supervisor, who is not afraid to engross his thoughts in the very details of the students considerations. His rigorous analytic thoughts and analysis often served as a very helpful paradigm for me, and especially in the beginning guided me on how approach biology with the methodology and mindset of a theoretical physicist. Additionally, he also provided many thoughts about the bigger picture of Ca^{2+} signaling or science in general. I am deeply thankful for his trust and his sometimes sudden bursts of valuable ideas.

Professor Hanspeter Herzel provided with his long and rich experience the narratives every scientist needs, to orientate and locate himself and his work within the scientific community. His farsightedness and universal knowledge often provided very helpful linkages to other studies and insights from various fields, and steered me away from moments of tunnel vision every student experiences at one time or the other. He particularly raised my awareness for the importance of data and data analysis, and the subtle pitfalls and ambiguities a theoretical biologist needs to know about. I am very thankful for his guiding spirit, which helped me to master the challenges of this thesis.

Without the participation of Dr. Alexander Löwer the project about p53 would simply not have happened. He gave me the opportunity to directly collaborate with experimentalists, which value can not be overstated. I am especially thankful for the many fruitful and intellectual challenging discussions which introduced me to the mindset and language of experimental biologists, and allowed me to develop thoughts and questions a theoretician alone would never think of. Even though he often grounded my overly ambitious plans, he made me realize that real progress can be made primarily in collaboration with the people who actually interact with the cells in the laboratory.

I would also like to thank the CSB graduate school for providing the funding and the many possibilities of exchange of views with other PhD students and PIs.

I am much obliged to the open source community around the python programming language, especially the SciPy and PyDStool community, for providing the indispensable tools needed for this work. The realisation of a helpful, and yes often anonymous but also altruistic and fun, community often lifted my spirit and motivated me to contribute in the future.

I would also like to thank all my Berlin dwellers who enriched my life experience profoundly. I want to single out my dear friend Matthieu Séry, who as an artist of life and art provided invaluable guidance on how to preserve and extend ones own identity during the progress of life.

Ich möchte mich auch bei meiner Mutter bedanken, war sie es doch die schon

in recht jungen Jahren meine Begeisterung für die große und interessante Welt der Wissenschaft im allgemeinen, und der Molekularbiologie im besonderen, geweckt hat. Auch meine Versuche sich als Physiker im Wirrwarr der Zellbiologie zurechtzufinden, hat sie bis zuletzt immer unterstützt.

Nun kann ich endlich auch meiner lieben Theresa danken. Ihr lebensfrohes Wesen, ihre Zuneigung und ihr eben nicht nur emotionales Verständnis waren mir unverzichtbare Unterstützung in den vergangenen Jahren. Keiner hat die Freuden und Leiden dieser Promotion intensiver begleitet als sie. Ich hoffe sehr, dass bald ich ihr auf diesem einzigartigen Abschnitt des Lebensweges ebenso den Rücken und das Herz stärken kann.